Study on the Method of Constructing a Statistical Shape Model and Its Application to the Segmentation of Internal Organs in Medical Images

by
Guangxu Li

A Dissertation Submitted to
the Department of Mechanical and Control Engineering
in Partial Fulfillment of the Requirements for the Degree of
Doctor of Engineering

at the

KYUSHU INSTITUTE OF TECHNOLOGY

July 2013

Certified by:

Professor Hyoungseop Kim
Chairperson of Supervisory Committee

ABSTRACT

In image processing, segmentation is one of the critical tasks for diagnostic analysis and image interpretation. In the following thesis, we describe the investigation of three problems related to the segmentation algorithms for medical images: Active shape model algorithm, 3-dimensional (3-D) statistical shape model building and organic segmentation experiments. For the development of Active shape models, the constraints of statistical model reduced this algorithm to be difficult for various biological shapes. To overcome the coupling of parameters in the original algorithm, in this thesis, the genetic algorithm is introduced to relax the shape limitation.

How to construct a robust and effective 3-D point model is still a key step in statistical shape models. Generally the shape information is obtained from manually segmented voxel data. In this thesis, a two-step procedure for generating these models was designed. After transformed the voxel data to triangular polygonal data, in the first step, attitudes of these interesting objects are aligned according their surface features. We propose to reflect the surface orientations by means of their Gauss maps. As well the Gauss maps are mapped to a complex plane using stereographic projection approach. The experiment was run to align a set of left lung models. The second step is identifying the positions of landmarks on polygonal surfaces. This is solved by surface parameterization method. We proposed two simplex methods to correspond the landmarks. A semi-automatic method attempts to “copy” the phasic positions of pre-placed landmarks to all the surfaces, which have been mapped to the same parameterization domain. Another automatic corresponding method attempts to place the landmarks equidistantly. Finally, the goodness experiments were performed to measure the difference to manually corresponded results. And we also compared the affection to correspondence when using different surface mapping methods.

The third part of this thesis is applying the segmentation algorithms to solve clinical problems. We did not stick to the model-based methods but choose the suitable one or their complex according to the objects. In the experiment of lung regions segmentation which includes pulmonary nodules, we propose a complementary region growing method to deal with the unpredictable variation of image densities of lesion regions. In the experiments of liver regions, instead of using region growing method in 3-D style, we turn into a slice-by-slice style in order to reduce the overflows. The image intensity of cardiac regions is distinguishable from lung regions in CT image. But as to the adjacent zone of heart and liver boundary are generally blurry. We utilized a shape model guided method to refine the segmentation results.

3-D segmentation techniques have been applied widely not only in medical imaging fields, but also in machine vision, computer graphic. At the last part of this thesis, we resume some interesting topics such as 3-D visualization for medical interpretation, human face recognition and object grasping robot etc.

ACKNOWLEDGMENTS

I am honored to have spent the last three years as part of my school life. I truly believe that understanding computer aided diagnosis at play within the healthcare industry is critical to its success. This study has allowed me to interact with dozens of incredible people across academia, industry and healthcare, all of which have contributed greatly to my experience.

I could not have completed this thesis without the support, encouragement and guidance of my advisor and thesis committee chair, Professor Hyoungseop Kim. His ideas, perspective and creativity greatly influenced and amazed me throughout my pursuit of this Ph.D. degree. His encouragement and belief in me were sources of energy that kept me going in difficult times. He was, is and will be the inspiration for my life.

I am very grateful to Professor Seiji Ishikawa for his insightful comments on my research process. He inspired much of my scientific thinking and reasoning. I would like to thank my other committee members: Professor Shuichi Kurogi and Professor Hiroshi Maeda for their contribution to this thesis. I also sincerely thank to Associate Professor Joo Kooi Tan for many useful discussions about the imaging techniques.

The most of gold standard data for research experiments were kindly provided by Dr. Akiyoshi Yamamoto. I cannot thank him enough for his dedication to my research. I knew that most of the works were done in his spare time. I could not have completed this thesis without his supports. My heartfelt thanks and my deep respects go to him.

I would like to thank international exchange student Eloi Duchaussoy for always having an open ear for many smart ideas to me. Thank Tobias Heimann at Medical and Biological Infomatics of the German Cancer Research Center for answering my spherical conformal mapping related questions in many helpful e-mails. We are grateful to the

National Cancer Institute and the Foundation for the National Institute of Health, USA on free publicly available LIDC database using in this study.

I am deeply indebted to OB (Old Boy) students: Hiroki Takahashi, Noriaki Miyake *et al.* for their supports and dedication in my research process. Thank you for being gracious with your time, experience and expertise. I look forward to continuing these relationships throughout my career and hope to be able to keep in touch with them in the future.

My sincere thanks also go to my fellow students, both in Kim laboratory and Ishikawa laboratory, for your perspectives, council, and friendship. You were crucial in helping me to develop my ideas and experiments, and afforded me with countless hours. There is no doubt I will be hearing of your future accomplishments and our friendships will not end.

To my family, the most important influences on my entire life: thank you for your endless support and believing in me. Your encouragement always pursues my dream. This thesis is especially dedicated to my dead grandfather with all my love. It was him who introduced the wonderful world of science to me and has been a guiding light since then. His voice and belief in me were sources of energy that kept me going in difficult times. My grandfather is the first person with whom I share my joys and my failures, and he has always stood beside me.

The last but not least, I would like to thank the other teachers and friends at KIT for supporting me over all these years: ARIGATOUGOZAIMASITA!

DEDICATION

In this thesis, we propose a 3-D statistical shape model based segmentation method. The statistical shape model building method and searching method are developed. The dedication is summarized below:

1. Based on the investigation of some widely applied segmentation methods, we present a brief framework to deal with the segmentation problems in medical imaging. This framework contributes to the construction of computer aided software project.

2. In segmentation experiments using 2-D active shape model method, the pose parameters and the shape parameters have strong coupling which always brings operation redundancy and precision loss. To overcome it, we introduce generic algorithm to calculate the parameters update.

3. To align all the training samples in the same spatial modality, we propose Gauss mapping based alignment methods. We compare two mapping images to confirm the rotation parameters of object in 3-D space. As well, since the limitation of boundary when mapping the stereographic surface into a plane, as the improvement, we introduce the stereographic projection to solve it.

4. Spherical conformal mapping is a novel method to parameterize a genus zero shape. We introduce this method to perform the correspondence of landmarks. We propose a semi-automatic correspondence method and an automatic method. As well, we test the affection to correspondence results from the constraints of spherical conformal mapping.

5. Regard to the experiments, we performed various methods for organic segmentation tasks. In lung regions segmentation from CT images, we propose a complementary region growing method to prevent the loss of detail information, such as lesions. In liver region

segmentation, we substitute a slice-by-slice region growing method for 3-D region growing method to improve the robustness of method. In cardiac region segmentation, we combine the mean shape model to fast marching method to reduce false negative rate.

TABLE OF CONTENTS

LIST OF TABLES

LIST OF FIGURES

CHAPTER 1: INTRODUCTION

1.1 MOTIVATION

Medical image segmentation, entailing separation of structures of interest from the background or from each other, plays a crucial role in extraction of useful information and images classification for most of medical imaging applications. Organic segmentation means extracting the target regions of organs from medical scan images, which generally include lung, cardiac, liver, kidney and spleen region. It is one of the important steps leading to image understanding, analysis, shape interpretation, as well as the fundamental part of Computer Aided Diagnosis (CAD) system. The accuracy of organic segmentation results always affects subsequent imaging processes, such as vessels extraction, characters measurement of lesions [1].

3-D organic segmentation focus on the whole interest organic region but not individual slice. With the development of multi-detector-row scan technique, hundreds of slices for each patient are tedious to analyze on a slice-by-slice basis. Consequently, the need for 3-dimensional (3-D) visualization and analysis tools is growing at a high rate of speed [2-4]. This technology has been useful in medicine. Anatomical knowledge coupled with image processing techniques is applied to improve healthcare [5, 6]. The Virtual Human Body project, in which the database and the human anatomy are obtained from the actual data have been widely used in anatomic education, simulation of X-ray imaging, surgery simulation and so on [7].

Many excellent methods have been conducted, such as thresholding methods [7-10], region growing methods [11-18], level set methods [19-27], graph cuts [28-33], deformable model methods [94-43] and atlas guided methods [44-46]. Each of these approaches has been developed into intact theoretical systems and extending. L. P. Dzung *et al.* [47] provided an overview of how the method was implemented, and discussed

their specialties. One of general classification methods for segmentation presents the fundamental concepts and techniques used for region-based and edge-based segmentation. But with the boom in this filed, obviously this category method seems has not met the demand.

One powerful subclass of deformable models---Statistical Shape Model methods (SSMs) has been developed in a top-down fashion [39-41]. This method attempts to learn the actual patterns of variability from a set of examples instead of using a single prototype. Statistical analysis is used to given an efficient parameterization of pattern of variation. Due to the inherent a priori information, this approach is more stable against local image artifacts and perturbations. Generally, there are three steps to construct such a statistical shape model: obtain the training samples by identifying the corresponding landmarks on the manually segmented volume data; align all the training sample in a common coordinate frame; statistical analyze the pattern of shapes and prove a compact representation of variation.

1.2 CHALLENGES IN MEDICAL IMAGES SEGMENTATION

Accurate segmentation of medical images meets with many challenges. First of all, many anatomical structures are inhomogeneous with respect to spatial repetitiveness of individual pixel/voxel intensities or their grouped co-occurrences. A typical example is extracting lung regions from chest CT images. The difficulty of the operation is the similar lung vessels and chest tissues. Low contrast medical images present additional challenges: e.g., boundary on cardiac and liver are difficult to determine even manually. Relative to the industrial imaging, the variability of shapes and textures in a Region of Interest (ROI) brings the further challenges. In addition, the lesions even cause the ROI beyond recognition completely.

1.3 OBJECTIVES

Main objective of this work includes three: Apply SSMs to organic segmentation in 2-D medical images. Contribute 3-D statistical shape model. Analyze segmentation algorithms in special applications and explore the approach of using shape model. In details,

- According to the feature characters of different objects, design an appropriate segmentation scheme and select detailed procedure and method.
- Aimed at a special topic of statistical shape model method, for building a statistical model, easily trainable method is required. Moreover, the training process should be efficient, robust and flexible.
- In terms of experiments of organic segmentation, develop robust, accurate and fast performance should be the first to be affected. Although it is difficult to reach human-like performance in medicine, proposed methods should deliver segmentation regions with a reasonably accuracy that is usable for real medical tasks.

1.4 OUTLINE OF THIS ARTICLE

This thesis is organized as follows. In chapter 2, investigate an overview of current methods used for computer assisted segmentation of anatomical image, we briefly describe an analytic method that split the segmentation problem to three processes: extracting the elements of image; selecting a style of propagation and inferring the variation of propagation. From chapter 3, we will analysis the statistic shape model based method. In details, in chapter 3, an improved two-dimensional (2-D) active shape model method is provided. We will state the model building method and how to apply the polygonal model to organic segmentation. To overcome the coupling of parameters in the original searching method, we introduce the Genetic Algorithm (GA). However, there are many demerits when using 2-D model based methods. In chapter 4 and chapter 5, we will discuss the key processes in 3-D statistical shape model construction and explain our proposed alignment method and corresponding method. Meanwhile we also scribe the methodologies and experiment approaches for triangular surface construction. As the

important application of organic segmentation, the segmentation experiments of lung regions, cardiac regions and liver regions are illuminated in chapter 6. The rendering techniques and the recent applications of 3-D segmentation technology is interpreted in the next chapter. Finally in chapter 8, we conclude this thesis with an outlook for future works.

CHAPTER 2: FRAMEWORK OF MEDICAL IMAGE SEGMENTATION

The segmentation problem could be decomposed into three processes: 1) extracting the image features and geometric characters; 2) selecting a style of propagation and 3) inferring the variation of propagation. For example, in Snakes methods or Active Contour Models (ACMs) [34], two image features are counted: intensity value and intrinsic pliable character of boundary of interest object. The propagation style is variable line segment. As well, the boundary of segmented object is inferred from balance of variation of two image features by minimizing energies optimization. We describe the details in the sections below.

2.1 EXTRACTION OF FEATURES

Medical images contain some visual noise. The presence of noise gives an image a mottled, grainy, or snowy appearance. It reduces image quality and is especially when adjacent objects have the similar issues the contrast is relatively low. With the purpose of obtaining relative desired image features, generally, first of all, the smoothing processing is implemented.

2.1.1 SMOOTHING FILTERS

2.1.1.1 Diffusion equation

Fick's low states that a concentration gradient of information quantity *f* causes a flux *j* which aim to compensate for this gradient. They are related by a diffusion tensor *D*. If we plug in Fick's law into the continuity equation we end up with the diffusion equation

$$\frac{\partial f}{\partial t} = div\left(D \cdot \nabla f\right) \tag{2.1}$$

where ∇ is gradient operator, $div(\cdot)$ is divergence operation. In image processing we may

identify the concentration with the gray value at a certain location. If the diffusion tensor is constant over the whole image domain, it called as *homogeneous* diffusion or *isotropic*, and a space-dependent filtering is called *inhomogeneous* or *anisotropic*. Often the diffusion tensor is a function of the differential structure of the evolving image itself. Such a feedback leads to nonlinear diffusion filters. Diffusion which does not depend on the evolving image is called *linear*.

When introduce this idea into imaging technique, support $f(p,t)$ can be viewed as a sequence of images at location p (Cartesian coordinates of a pixel. In 2-D image, p = (x, y)) and time t. It starts with $f(p,0)$ and evolves over time to become smoother. "Smoothing" process becomes an initial value problem that we put in an image f at $t = 0$ and obtain a smoother image at some later time t. While t becoming larger, result image is smoother.

2.1.1.2 Gaussian smoothing

Let $D = 1$ for a linear case. If we assume either an infinite or cyclical domain for the image and take the Fourier transform of f with respect to the spatial dimension, we can express diffusion equation as

$$\frac{\partial F}{\partial t} = -d^2 F \tag{2.2}$$

where d is the distance from the origin of the Fourier transform. This is an ordinary differential equation, and its solution is an exponential of the form

$$F(d,t) = e^{-d^2 t} F(d,0)\,. \tag{2.3}$$

When we consider a linear diffusion equation, i.e. linear and shift invariant, its solution can be represented by convolution with a kernel. If transform the solution of Eq. (2.3) back to the spatial domain, we could get the Gaussian form function

$$f(p,t) = \frac{1}{\sqrt{4\pi t}} e^{-\frac{|p|^2}{4t}} \otimes f(p,0). \tag{2.4}$$

Comparing to the Gaussian kernel

$$g(p) = \frac{1}{\sqrt{2\pi\sigma^2}} e^{\frac{|p|^2}{2\sigma^2}} \tag{2.5}$$

where σ is the standard deviation, we can see that the solution to the diffusion equation at a particular time is the same as convolving the initial conditions with a Gaussian of standard deviation $\sigma = \sqrt{2t}$. Fig. 2.1(a) demonstrates a smoothed image. Some novel algorithms have been proposed for medical imaging [48].

2.1.1.3 Anisotropic diffusion smoothing

The drawback of linear filter used in medical imaging is that it tends to blur away the sharp boundaries in the image that help to distinguish between the larger-scale anatomical structures. The motivation for anisotropic diffusion (also called *nonuniform* or *variable conductance* diffusion) is that a Gaussian smoothed image is a single time slice of the solution to the heat equation that has the original image as its initial conditions [49]. Nonlinear diffusion filters utilize *D* in Eq. (2.1), as a scalar-valued diffusivity which is adapted to the underlying image structure. Perona and Malik [50] proposed such a method for avoiding the blurring and localization problems of linear diffusion filtering. They applied an inhomogeneous process to reduce the diffusivity at those locations which had a large likelihood to be edges. Such purpose can be done by let $D = c\left(|\nabla f|^2\right)$, such

$$D = \frac{1}{1 + |\nabla u|^2 / \lambda^2}, \tag{2.6}$$

done in [51]. Therefore, the variable conductance can be formulated to limit the smoothing at “edges” in images, as measured by high gradient magnitude (Fig.2.1).

(a) (b) (c)

Figure 2.1 Effects of smoothing filter. The processing is firstly smooth the input image using smoothing filter. Then to observe its effect, enhance gradient magnitude of image and transform the result to binary image. (a) One slice of liver abdominal CT image. (b) Smoothing filter uses Gaussian kernel. (c) Smoothing filter uses gradient anisotropic diffusion filter. We can see that in (c) some parts with line-like structure are preserved.

2.1.2 GRADIENT

2.1.2.1 Differentiation

Changes or discontinuities in an image amplitude attribute such as luminance value or density are fundamentally important primitive characteristics of an image because they often provide an indication of the physical extent of objects within the image. That is the basic idea when we process an image using maximum gradient strength. In general, derivative edge detection is the most applied for edge detection. The first derivative is well known as gradient. We can extract the edge map function $em(p)$ from the binary image $I(p)$. Suitable edge map functions are given by the equations:

$$em(p) = -|\nabla I(p)|^2$$

or

$$em(p) = -|\nabla[G_\sigma(p) \otimes I(p)]|^2, \tag{2.7}$$

where $G_\sigma(p)$ is a two dimension Gaussian function with standard deviation σ. The second derivative is a matrix, known as the Jocobian.

$$\begin{bmatrix} \frac{\partial^2 f}{\partial x^2} & \frac{\partial^2 f}{\partial x \partial y} \\ \frac{\partial^2 f}{\partial y \partial x} & \frac{\partial^2 f}{\partial y^2} \end{bmatrix}.$$

The elements of this matrix are useful in a number of ways, such as the Laplacian

$$\nabla^2 f = \frac{\partial^2 f}{\partial x^2} + \frac{\partial^2 f}{\partial y^2}, \tag{2.8}$$

sums the diagonal terms of the Jacobian to yield a rotationally invariant representation of the second derivative of image intensity.

2.1.2.2 Vector flow

Edge map $em(p)$ derived from the image $I(p)$ having the property that it is larger near the image edges. Gradient Vector Flow (GVF) field is computed as a diffusion of the gradient vectors of a gray-level or binary edge map derived from the image [36]. The GVF field v(**x**) as the equilibrium solution to the following vector diffusion equation

$$\begin{aligned} \mathbf{u}_t &= g\left(|\nabla f|\right)\nabla^2\mathbf{u} - h\left(|\nabla f|\right)\left(\mathbf{u} - \nabla f\right) \\ \mathbf{u}(\mathbf{x}, 0) &= \nabla f(\mathbf{x}) \end{aligned} \tag{2.9}$$

Here, the first term on the right is referred to as the smoothing term since this term alone will produce a smoothly varying vector field. The second term is referred as the data term since it encourages the vector field **u** to be close to ∇f computed from the data. The weighting functions $g(\cdot)$ and $h(\cdot)$ apply to the smoothing and data terms, respectively. They are the functions with respect to $|\nabla f|$. Since these weighting functions are dependent on the gradient of the edge map which is spatially varying, the weights themselves are spatially varying generally. Fig. 2.2 demonstrates an example of vector flow.

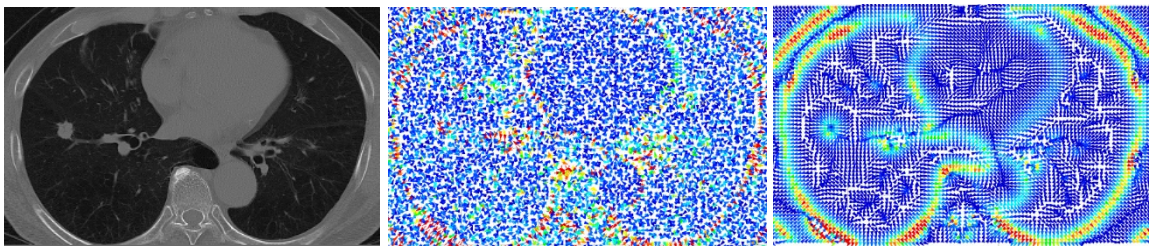

(a) (c) (d)

Figure 2.2 Examples of edge map and GVF. (a) One slice of chest CT image. (b) Its edge map image. (c) Its vector flow image.

2.2 SHAPE REPRESENTATION

2.2.1 2-D SHAPE REPRESENTATION

2.2.1.1 Pixels line

This representation is the most common in image processing, especially in edge detection. An edge in a continuous domain can be detected by forming the continuous one-dimensional gradient along with a line normal to the edge slope. If the gradient is sufficiently large, an edge is deemed present. The gradient along the line normal to the edge slope can be computed in terms of the derivatives along orthogonal axes. Most of common edge detection algorithms try to find edge pixels meanwhile to eliminate the noise influence. However, in medical images, due to noise influence and structural break, the edges or other line structures are usually not clearly defined. To overcome these defects, geometric characters, such as curvature, are utilized to recover the line structure. Another novel works were proposed to enhance the line-like structures, which is known as selective enhancement filters [52].

2.2.1.2 Polyline

The polyline is a composite one-dimensional cell consisting of one or more connected lines. The polyline is defined by an ordered list of $n+1$ points, where n is the number of lines in the polyline. Almost the most famous segmentation method using this

representation is the Snakes. They try to find the edges of object using a segment line as well as tracking those contours during motion and matching them in stereopsis.

2.2.2 3-D SHAPE REPRESENTATION

2.2.2.1 Voxels

Voxel-based visualization is an example of a regular volumetric grid. Tim and Demetri present a physics-based approach to anatomical surface segmentation, reconstruction [42]. Cootes and Taylor use finite element methods to calculate vibrational modes for each training shape, which are used to generate a number of modified shape instances [54].

It is very common to find medical image datasets that have been acquired with anisotropic shapes. For medical image analyzing and diagnosing by radiologists, “one-by-one” reading style is also prevalent. However, for the model building and image reconstruction, the extreme rectangular pixel shapes becomes regular. To overcome this asymmetry and uniform the different dataset, image *isotropic* procedure is used to subsample the high in-plane resolution and to super-sample the inter-slice resolution. Generally the subsampling process requires that we preprocess the data with a smoothing filter in order to avoid the occurrence of aliasing effects.

2.2.2.2 Point distribution model (PDM)

The pattern of “legal” variation in the shapes and spatial relationships of structures is obtained from a set of training samples, which are marked using landmarks. Statistical analysis is used to given an efficient parameterization of this variability, providing a compact representation of shape and allowing shape constraints to be applied effectively during image interpretation. Due to a clash with nomenclature in the statistics literature, they are now re-christened statistical shape model in the literature. In this thesis, we specify the SSM as subclass of PDM which the positions of points are corresponded.

The conception of *landmarks* was denoted as the anatomic landmarks in medicine at the beginning. In SSM literature, the landmarks are referred as a set of involved points

that used to represent shapes distributed across the surface. They have been used extensively for the statistical study of biological shape [55-59]. We presume that one kind of issues have the similar structure. In order to calculate statistics of shapes, the corresponding landmarks across the whole surface data should be located at the same anatomical positions of surface. So, to model a statistics of a class of shapes, a set of appropriate training shapes with well-defined correspondences is required.

2.2.2.3 M-rep

Medial representation (m-rep) or skeleton has been used to describe biological shapes by Blum since in the 1970s and are commonly utilized in image analysis [60, 61]. They represent objects by their centerlines and vectors pointing from there toward the boundary, often leading to a more compact description than landmarks. Pizer *et al*. present a medial model with a coarse-to-fine representation for two dimensions [62]. This approach was later extended to three dimensional in and termed m-rep. It has been used successfully for a number of medical image processing tasks, including segmentation.

2.2.2.4 Spherical harmonics (SPHARM)

Spherical Harmonics is a set of basic functions which can be used to describe closed surfaces of spherical topology. Among others, this method was employed for deformable models in image segmentation by Szekely *et al*. [63]. Also related to the SPHARM technique is the method employed by Nikou et al. who hierarchically describe surfaces using the vibration modes of a spherical mesh [64]. Another approach for shape description using wavelets to deal with 2D shape has been proposed by Davatzikos *et al*. [65]. Nain *et al*. presented versions using spherical wavelets for the 3D cases [66].

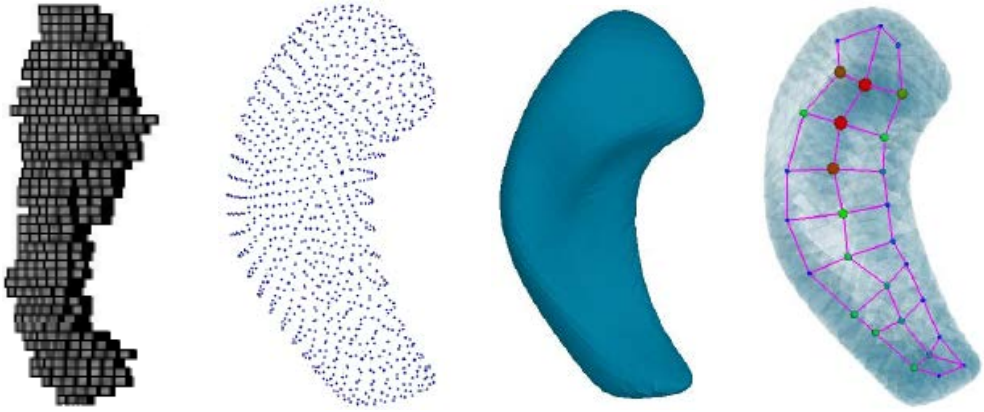

(a) (b) (c) (d)

Figure 2.3 Four different shape descriptions of a human left hippocampus: (a) Voxels (b) point distribution model. The points are remarked as landmarks (c) Spherical harmonics (SPHARM) (d) M-rep. (all pictures are from [67])

2.3 PROPAGATION

2.3.1 DIMENSIONALITY

Dimensionality of an algorithm refers to whether a segmentation method operates in a 2-D image domain or a 3-D image domain. Some methods are easy to be expanded from 2-dimennal space to 3-D. However, in some methods such as deformable models, incorporated spatial information may lead to the difficulty of operation. In some cases, however, 2-D methods are applied sequentially to the slices of a 3-D image [69]. They are favors because of practical reasons such as ease of implementation, lower computational complexity, and topology. In addition, it is easier to observer the process in 2-D plane, due to most of viewer support 2-D only.

A unique situation that occurs in computer imaging is the delineation of regions on a non-Euclidean domain, such as surface geometry. Because a surface is a 2-D object folded in 3-D space, segmentation on a surface cannot be treated as a standard 2-D or 3-D problem. The modeling of spatial characteristics along a surface is much more difficult than in a standard imaging plane because of the irregular sampling used by mesh representations. This is an emerging area of research and preliminary results have shown

great promise.

2.3.2 HISTOGRAM

Image histogram is a classical way when using automatic threshold algorithm. It makes the premise that the interested structures or regions have distinctive quantifiable features such as the image intensity or the gradient magnitude. Each of the regions can be separately processed for information extraction. Segmentation can be accomplished by identifying all pixels or voxels that belong to the same structure/region or based on some other attributes associated with each pixel or voxel [70]. Except for accounting the image density itself, image features are also be taken in account, such as Gray Level Co-occurrence Matrix (GLCM), Zernike moments and so on. Fractal models are also used to describe medical structures [71]. Fractal is useful in modeling statistical roughness and self-similarity at different scales of many natural surfaces. These models are scale independent, display self-similarity, and are able to model natural textures Histogram based methods have been derived as: global methods based on gray-level histograms, global methods based on local properties, local threshold selection, and dynamic thresholding, etc. [72]. Thresholds used in these algorithms can be selected manually or automatically. Fig. 2.4 shows some instances of organic regions. The comparisons of histograms between the intensity of interesting regions and the intensity statistic of background are demonstrated.

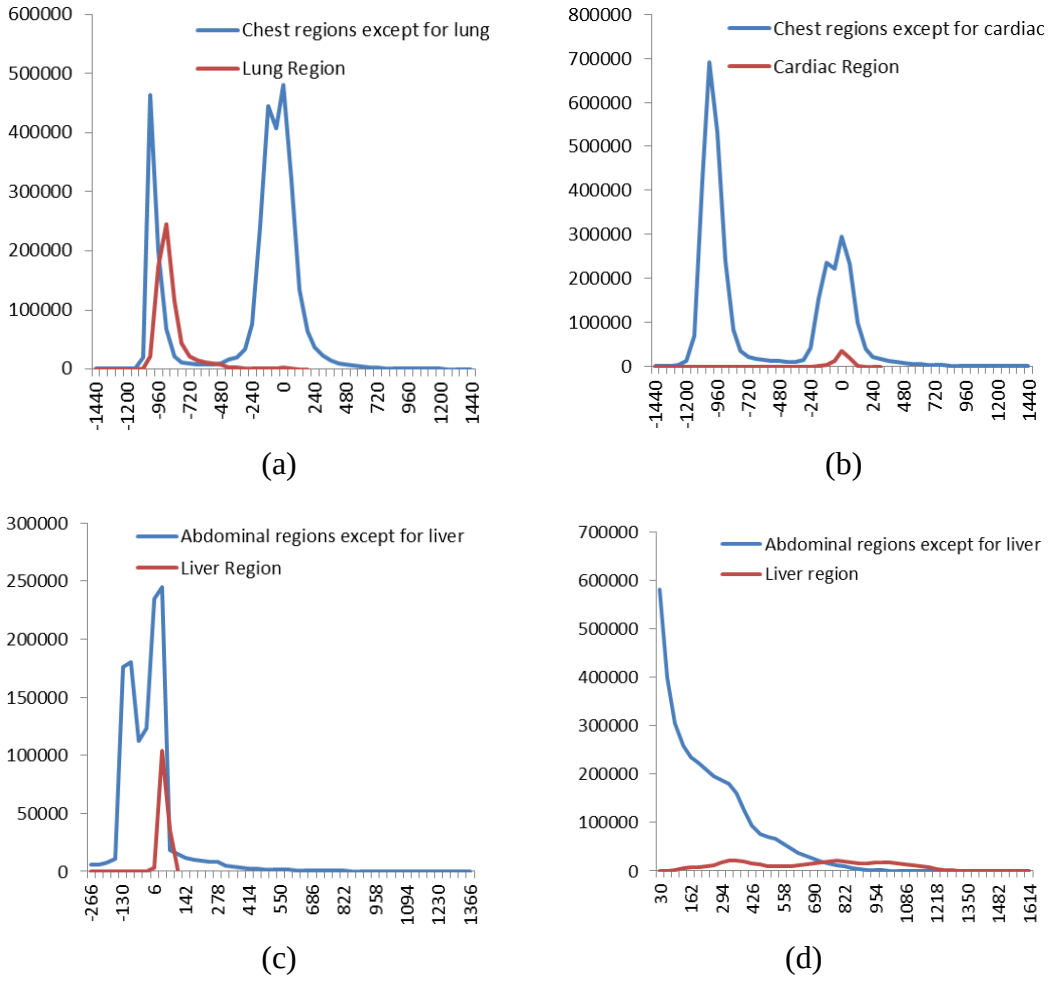

Figure 2.4 Histograms. (a) Lung regions from chest CT images (b) Cardiac regions from chest CT images (c) Liver regions from abdominal CT images (d) Liver regions from abdominal MRI images (with contrast medium)

2.3.3 Region Growing

The ideas of region-based algorithms come from the observation that quantifiable features inside a structure tend to be homogeneous [12]. The searching rules are different among algorithms. The most common used method is seeds based, which is also known as flood fill algorithm. The growing regions are started from some previously set seeds and expended by merging the unallocated neighbor pixels of which the image features are within the thresholds. Another searching rule is using unseeded algorithms, such as scanline fill algorithm, while the merging criterion is same the first one. By applying

statistical features properties, one can extend the concept of threshold-connected components to include confidence-connected components. These statistical methods of linking pixels or voxels in a dataset can be used to delineate regions or boundaries, depending on the application.

When we want obtain a three dimensional object using region growing method, two merging styles could be considered. The first one is the “real” three dimensional growing scheme, that means each front-pixel (from which the searching is performed) has 6 or 8 neighbors (make up a cube). When the object has single connectedness, growing process could be completed from one seed. And we do not worry about the topology of the object. But because of the flexibility, this scheme is very weak to deal with the medical images which always filled with noises. Another disadvantage is that since it is common to find medical image datasets that have been acquired with large inter-sclice spaces, different regions are always dealt with into one region. As in Fig. 2.5(a) showing, region I and region II have the similar intensity. When we want to extract region I, region II is emerged together caused of the overlap of two successful slices at the boundary.

Another merging style is region growing slice-by-slice, and integrating all extracted 2-D regions together finally. Obviously, it could reduce the affection from the noises or anisotropic of slices in a certain degree, but many under-growing regions could be found due to losing of the topological information, as shown in Fig. 2.5(b).

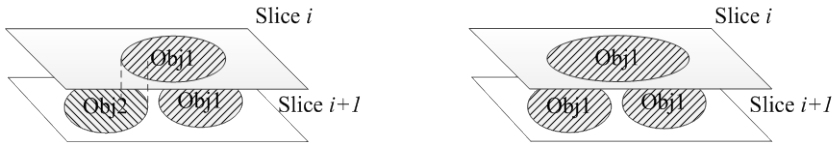

(a) (b)

Figure 2.5 Region growing through serial of slices. (a) Mapping the Obj1 in Slice *i* to Slice *i+1*, there are overlap regions with Obj2 in Slice *i+1*. When using 3-D region growing method to obtain Obj1, overflow might occur from these overlap regions. (b) Objective region becomes branched over slices. In this case, one region might be loosed if running region growing in slice-by-slice style.

2.3.4 LEVEL SET

Level set methods add dynamics to implicit surfaces. The key idea that started the level set fanfare was the Hamilton-Jacobi approach to numerical solutions of a time-dependent equation for a moving implicit surface [19],

$$H + \frac{\partial S}{\partial t} = 0$$

where $H = H\left(q_1, \cdots q_N; \partial S/\partial q_1, \cdots, \partial S/\partial q_N; t\right)$ is the classical Hamiltonian function, $S = S(q_1, \cdots, q_N, t)$ is called Hamilton's principal function. t denotes time. It is obvious that a variation in N dimensional space is related with a scalar function S in N+1 (original N dimensions plus t). The level set method was initially proposed to handle the topological changes during the curve evolution. When we consider an image I. The boundary function of point p at time t is $C(p,t)$. We assume the boundary is propagated along the normal direction N of boundary. Propagated speed is $F(k)$ which relates the curvature of boundary k. Variation of boundary could be denoted as

$$C(p,t) = F(\kappa)\mathbf{n}\,. \tag{2.10}$$

Introduce an implicit embedding $\phi(p(t), t)$, and the boundary $C(p,t)$ is treated as $\phi(p(t), t) = 0$, i.e.

$$\begin{aligned} C(p,t) &= \{p : \phi(p,t) = 0\} \\ C(p,0) &= \{p : \phi(p,0) = 0\} \end{aligned}. \tag{2.11}$$

Since $C(t) = \phi^{-1}(0)$, we can contribute the relationship between ϕ and $C(t)$,

$$\phi\left(C(t), t\right) = 0\,.$$

The partial differential equation of ϕ with respect to time, denoting as ϕ_t is

$$\phi_t + \nabla\phi[C(t), t]p_t = 0 \tag{2.12}$$

where p_t denotes as the partial differential equation of $p(t)$. On the other hand, the normalized normal vector **n** can be calculated using

$$\mathbf{n} = \frac{\nabla\phi}{|\nabla\phi|}. \tag{2.13}$$

Such

$$F(k) = p_t\mathbf{n} = p_t\frac{\nabla\phi}{|\nabla\phi|}. \tag{2.14}$$

The Eq. (2.11) could be represented as

$$\begin{aligned} &\phi_t + F(\kappa)|\nabla\phi| = 0 \\ &\phi[C(p,0),0] = 0 \end{aligned}. \tag{2.15}$$

The advantage of doing so is that the topological changes can be easily handled and the geometric properties of the contour can be implicitly calculated. Therefore, the computational complexity of geometric deformable models is decreased. Like in the parametric deformable models, speed functions should be defined properly to drive the contour to the right position.

An important development of level set method is called fast marching Method, which assume for that speed function F is always bigger than zero. Hence the propagation of boundary has a certain direction “outward”. One way to characterize the position of this expanding front is to compute the arrival time t of the front as it crosses each point p. And along the normal direction of boundary, the front motion is characterized as the solution to a boundary value problem. If the speed F depends only on position, the Hamiltonian equation reduces to what is known as the Eikonal equation. Malladi *et.al* [20] applied this method to the medical image segmentation. To overcome the drawback

of leakage in Malladi's method, a stopping criterion is selected carefully to make sure the contour stops at the right position. If the images are noisy or blurred, the contour may shrink to disappear after long time evolution.

One of derivation of level set method is geodesic active contour algorithm (GAC). It utilizes the gradient of pixel value as the factor of speed function directly and models the segmentation as an optimization problem of finding the minimal distance curve in the image [22]. Geodesic active contour algorithm shows a tight relationship between the parametric model and the geometric model. A survey of algorithms that combine statistical techniques with level set methods can be found in [23].

2.3.5 Deformable Model Based Methods

In order to perform higher-level analysis to defend the noise, occlusion, and structural complexity in medical images, a priori information must be incorporated into the interpretation process. A convenient way of achieving this is to use a flexible model to encode information such as the expected position, structure shape and local surface curvature of objects in an image. A fairly extensive review on various deformable model methods can be found in [38].

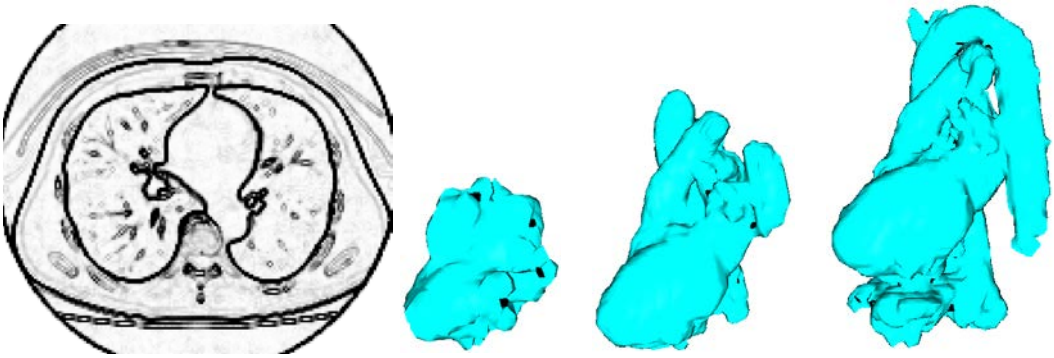

Figure 2.6: An example of extracting cardiac regions using fast marching method. (a) Edge map used to compute the speed term for the front propagation. (b) Segmented result when iterated 200 times. (c) Result when iterated 450 times. (c) Result when iterated 600 times.

A local flexible model was popularized form Snakes proposed by M. Kass. A snake deforms so as to match image features whilst ensuring that it satisfies structural constraints, such as curvature. It is an explicit tracking way with the advantage of high computational efficiency. In [37], an interactive mechanism was developed that allows user to select control points in order to form a constraining force to influence the curve movement. Numerical comparisons have shown that these improved algorithms considerably decrease the influence of initial conditions and improve the segmentation results. However, a snake lacks specificity as it has little knowledge of the domain, limiting its value in image interpretation.

Incorporation of global shape information is one of the possible solutions to constrain the segmentation of organ structures which are also called statistical model based approaches. Generally, these approaches are always described as an optimization problem of searching the best fit for the image data to the model. One typical statistic shape model was developed by Cootes *et al*., including Active Shape Model (ASM) [39] and Active Appearance Model (AAM) [40]. Training samples are used to extract the mean shape and define proper ranges of the parameters. After finding an approximate position of the new examples, active shape model uses the edge information to move the control points (also called landmarks) to better positions while the AAM added the mean texture of each point to find a better position. The searching procedure is like the snake methods but the movements of control points are constrained by the ranges of shape parameters which guarantee the similarity between the segmentation result and the training samples. These methods have been applied widely in 3-D medical image segmentation [47]. Although AAM can also be seemed as the derivation of ASM, because of the great successful in computer imaging, this method has been established as a new class. We will leave out it in this thesis.

2.3.6 Atlas Based Methods

Atlas-based segmentation is an imaging task which involves labelling a desired

anatomy or set of anatomy from images generated by medical imaging modalities. It could be described as finding a one-to-one transformation that maps a pre-segmented atlas image to the target image. The overall goal of atlas-based segmentation is to assist radiologists in the detection and diagnosis of diseases [46]. Atlas-guided approaches are a powerful tool for medical image segmentation since the anatomic knowledge could be stored in a standard atlas or template is available. Two types of atlases are always utilized: The first one attempts to construct the atlas based on a single subject. In the literature these atlases are called topological, single-subject or deterministic atlases. The single-subject atlas is often a volume image which recorded the average size, shapes or intensity of a class of objects. Note that, however ASM, AAM can also be considered as atlases since they bring spatial prior knowledge to the segmentation process. The second one are often cited as population-based, statistical or probabilistic atlases. Atlases based on a single-subject are not constructed to represent the diversity of human anatomy. To better characterize the variability of anatomical structures, atlases have been constructed on the basis of populations. Such templates could be represented by a probabilistic atlas can be easily subdivided into groups according to specific criteria.

2.3.7 GRAPH THEORY

Many graph theoretic techniques have been proposed for cluster analysis [28]. The graph approach generally implements as a coarse-to-fine process. To improve the precision of boundary tracking, multi-resolution pyramids were used to connect discontinuities in traced edges [29].

Another novel methods using graph theory is known as graph cuts. It is represented using an adjacency graph, have been applied as global optimization methods in image segmentation. Each vertex of the graph represents an image pixel, while the edge weight between two vertices represents the similarity between these two vertices.

Random walker algorithm is a novel for performing multilabel, interactive image segmentation. Given a small number of pixels with predefined labels, one can

analytically and quickly determine the probability that a random walker starting at each unlabeled pixel will first reach one of the prelabeled pixels. By assigning each pixel to the label for which the greatest probability is calculated, high-quality image segmentation may be obtained [33].

2.3.8 OTHERS

Edge tracking. In the automatic tracing case, the target tracking framework is applied by first assuming that a hypothetical target has followed the boundary of an object in an image and that measurements of its position have been taken at equal time intervals. The position information is obtained by applying an edge detector to the image to identify discrete edge points [73].

Watershed. The concept of watersheds based segmentation method in three dimensions could be treated as two spatial coordinates versus gray levels. Due to the combination of diverse image information, watershed algorithms can achieve satisfied results and always produce a complete segmentation of an image. To handle the over-segmentation, hybrid threshold-based algorithms usually incorporate other techniques to perform the segmentation [74]. Some intuitive images of propagation methods are shown below.

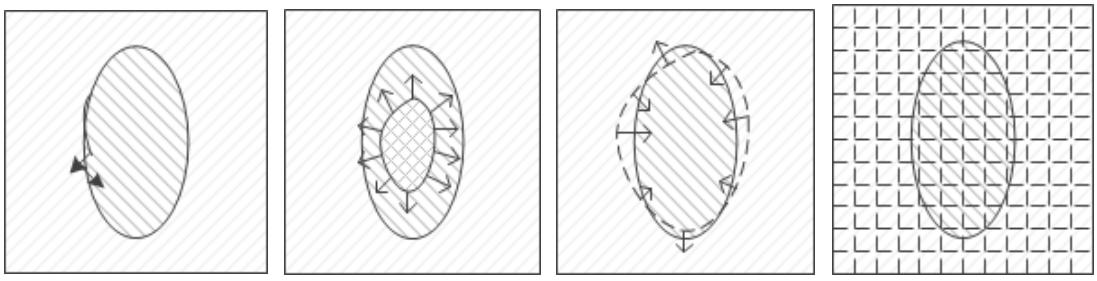

(a) (b) (c) (d)

Figure 2.8: 4 examples of propagation styles. (a) Edge tracking. (b) Region growing (c) Deformable model (d) Image dividing. Divide the image into patches and remain the patches which are between the “inside” and “outside”. Then divide the remained patches again subtly. Iterate this processing.

2.4 FITNESS FUNCTIONS

2.4.1 DISTANCE MINIMIZING

In geometry, *L1 Norm* measures the absolute distance between the pixels of the original and the corrected image. *L2 Norm* measures the Euclidian distance between the pixels of the original and the corrected image. And distant minimum of L2 Norm means minimizing root mean squared distance. This principal is generally used to solve the registration problem. Segmentation using statistical model-base method could be dealt with as a registration procedure.

A dominant method using distance minimizing is Iterative Closest Point (ICP) algorithm [75]. It starts with two meshes and an initial guess for their relative rigid-body transform, and iteratively refines the transform by repeatedly generating pairs of corresponding points on the meshes and minimizing an error metric. Generating the initial alignment may be done by a variety of methods [76]. Many variants of ICP have been proposed, affecting all phases of the algorithm from the selection and matching of points to the minimization strategy. As one of the derivation, mesh-to-volume registration methods adapts a deformable surface model to the volumes, and according to the relative positions of corresponding landmarks, searches for the best matching. We use this approach to constrain both ends of cardiac regions in segmentation experiment. The details are described in section 6.3.

2.4.2 ENERGY MINIMIZING

In active contour model method, a typical energy functional includes the internal energy and the external energy. The internal energy aims to keep the regularity of the contour and is usually defined through the geometric properties of the contour such as length, area or curvature; the external energy attracts the contour to the boundary position and is defined by the image information. The definitions of external forces are the main differences between algorithms. Variable evolutions have been developed to overcome the insufficient of the original snake method. For example, in order to prevent the curves

from shrinking or stopping on local minimum, an added balloon force to the external forces to make the contour inflate or deflate when the gradient field is weak []. By analyzing the reason why the original Snakes have unstable convergence to boundaries with large curvatures, Xu and Prince replaced the gradient field with GVF [36].

Energy minimizing is applied in Graph cut as well. Usually, the cost function to be minimized is the summation of the weights of the edges that are cut. The exact solution can be found in polynomial time. The normalized cut approach [29] is aimed at reducing this bias by introducing a cost function called disassociation. However, the algorithm is slow for planar graphs and NP-hard for non-planar graphs. Interactive graph cuts [30] use s–t minimum cut as an optimization method with the user identifying the object and background regions interactively.

2.4.3 Linear Model

For a single multivariate Gaussian, where the data is independent and the principal component axes do correspond to real modes of variation of the input data. Principal component analysis (PCA), also called K-L transform or Hotelling transform, is probably the most famous method [78]. It has been widely applied in a number of scientific areas and usually used to reduce dimensionality. To apply PCA, we consider a distribution of the data by a multivariate Gaussian, which centers on the mean of the data in shape space.

In many cases, where the shape variation is linear, a multivariate Gaussian density model is sufficient. If the distribution is not simple, PCA will still enable us to discard dimensions which are orthogonal to the data, that is, perform dimensional reduction. The individual directions of vectors will not however necessarily correspond to modes of variation of the data. A kernel-based technique then comes in handy, which is known as kernel principal component analysis [79]. Another popular technique is independent component analysis (ICA), which does not assume a Gaussian data distribution and delivers statistically independent projections. It was applied to shape modeling to obtain more abundant description of shapes [80].

2.4.4 BAYESIAN PRINCIPLE

Using Bayesian principle is another novel way to integrate prior knowledge of anatomical structures to segmentation process [81]. The goal of this work is to unify this process into a single Bayesian framework in order to overcome biases caused by commitment to the initial registration. With notable exceptions, these methods first register the prior information, i.e., an atlas, to the medical image and then segment the medical image into anatomical structures based on that aligned information. Because the Bayes rule allows us to modify our knowledge about a process using both the historical information and the current data, it has been successfully used to segment anatomical structures defined by weakly visible boundaries in medical images.

2.4.5 INTELLIGENCE METHODS

The objective function in medical image segmentation is usually complex, multimodal, discontinuous, and cannot be described in a closed mathematical form that can be analytically solved. Thus, application of several classical techniques becomes limited. In these cases intelligence method seems to be appropriate and natural. Genetic Algorithms (GAs) is a search and optimization method that is capable of handling huge, complicated, and multimodal search spaces. Moreover, incorporation of domain knowledge about the image brings considerable flexibility in the segmentation procedure. In [82], U. Maulik summarized the state of the art in medical image segmentation using GAs and broach this topic in 5 techniques: contour-based technique, texture-based technique, knowledge-based technique, learning-based technique and model-based technique.

Fuzzy technique has been utilized for medical image segmentation for decades [83]. Neural networks based classification is also a common nonlinear parallel processing. Some authors focus on a particularly effective class of neural networks, the generalized radial basis functions, and present an approach that combines unsupervised and supervised techniques [84].

2.5 EVALUATION OF IMAGE SEGMENTATION

Image segmentation consists of object recognition and delineation. Generally, there are three factors to evaluate the results of segmentation: precision, accuracy, and efficiency [85]. To assess precision, we need to choose a figure of merit, repeat segmentation considering all sources of variation, and determine variations in figure of merit via statistical analysis. It is impossible usually to establish true segmentation. Hence, to assess accuracy, we need to choose a surrogate of true segmentation noted as *gold standard* and proceed as for precision. In determination of accuracy, it may be important to consider different ROI to be segmented depending on the application. To assess efficiency, both the computational and the user time required for algorithm training and for algorithm execution should be measured and analyzed.

2.5.1 DEFINITION OF GROUND TRUTH

Although it is impossible to establish absolute true segmentation, some surrogate of truth is applied. Two possible choices for delineation are outlined below.

2.5.1.1 Manual delineation

In medical imaging human expert knowledge is often used as a substitute for a gold standard [86]. Object boundaries are traced or regions are painted manually by experts. Sometimes, it is easier for experts to manually correct the delineation produced by a pretreatment. To acquire an objective representation, multiple repetitions of segmentation by multiple operators is encouraged. Then the accuracy rate is generated by voting the experts' results.

2.5.1.2 Synthesized data

A set of mathematical phantoms is created to depict the application domain as realistically as possible in terms of image blur, relative tissue contrast and heterogeneity, noise, and background inhomogeneity in the images (Fig. 2.9). We can also add the known deformation to simulate the real images. The main shortcoming of this approach is the questionable authenticity when changing the algorithm to real segmentation practices.

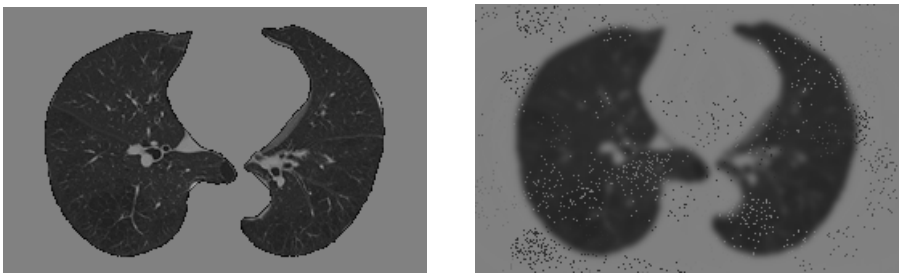

(a) (b)

Figure 2.9: A sample of synthesized data for evaluating the segmentation result. (a) The "true" objective region. (b) Be blurred and added noises.

2.5.1.3 Probabilistic distances between segmentation

In a lot of medical image segmentation tasks there are no clear boundaries between anatomical structures. Absolute ground truth by manual segmentation does not exist and only a "fuzzy" probabilistic segmentation is possible [87]. Manual probabilistic segmentations can be generated by aggregating repeated multiple segmentations of the same structure done either by a trained individual rater or by multiple raters. We have developed a probabilistic overlap measure between two fuzzy segmentations derived from the normalized *L1* distance between two probability distributions. The probabilistic overlap is defined as

$$POV(A,B) = 1 - \frac{\int |P_A - P_B|}{2\int P_{AB}} \tag{2.16}$$

where P_A and P_B are the probability distributions representing the two fuzzy segmentations and P_{AB} is the pooled joint probability distribution.

2.5.2 RECEIVER OPERATING CHARACTERISTIC

One way of summarizing classification results (labeling) is creating a data set for each class. As illustrated in Tab. 2.1, a confusion matrix is composed of four cells. Each cell is the number of instances that meet the criteria of it. There are four possible outcomes that need to be identified: (a) correctly segment a region (TP), (b) over-segment a region (FP), (c) under-segment a region (FN), (d) correctly ignore a region (TN).

Table 2.1: Receiver Operating Characteristic

		Actual class	
		Negative	Positive
Predicted class	Negative	True Negative (TN)	False Negative (FN)
	Positive	False Positive (FP)	True Positive (TP)

There are several standard terms derived from this confusion matrix. Among such quality terms, we use two terms, *true positive rate* (TPR) and *false positive rate* (FPR):

$$\begin{aligned} \text{TPR} &= \frac{\text{TP}}{\text{FN} + \text{TP}} \\ \text{FPR} &= \frac{\text{FP}}{\text{TN} + FP} \end{aligned} \tag{2.17}$$

We also should merit attention that the accuracy of a segmentation technique must be judged by its performance on a specific application. At the same time different classifier criteria make different assumptions of interesting regions, the specification of the problem is important.

2.5.3 Dice Similarity Coefficient

A common evaluation measure for brain segmentation is the *Dice similarity coefficient* (DSC), an overlap metric between two binary masks defined as:

$$DSC = \frac{2\left|A \cap M\right|}{\left|A\right| + \left|M\right|} \tag{2.18}$$

where A represents the automatic segmentation mask and M the manual segmentation from the expert. DSC ranges between [0, 1], and DSC values equal or higher than 0.7 are usually considered as a good agreement between two binary masks [88]. This measure is mathematically related to the *Area Overlap* (A_{ov}), another common similarity index presented in [89]. The A_{ov} also ranges between [0, 1], and it is defined as:

$$A_{ov} = \frac{|A \cap M|}{|A \cup M|} \tag{2.19}$$

2.5.4 CROSS CORRELATION

In probability theory and statistics, correlation is always used to include a standardizing factor in such a way that correlations have values between −1 and +1. The correlation between two signals is a standard approach to feature detection as well as a component of more sophisticated techniques. To use of cross-correlation for template matching is motivated by the distance measure

$$d = \sum_{x,y} [f(x,y) - t(x-u, y-v)]^2 \tag{2.20}$$

where f is the image and the sum is over x, y under the window containing the template t positioned at (u, v). Expand this representation, remove the invariant parameters, the cross-correlation term can be express as

$$c(u,v) = \sum_{x,y} f(x,y)t(x-u, y-v)\,. \tag{2.21}$$

It is used to measure the similarity between the image and the template. There are several disadvantages to using Eq. (2.21) for template matching.

2.5.5 HAUSDORFF DISTANCE

Hausdorff distance is also called maximum surface distance [90]. The Hausdorff-Chebyshev metric defines the largest difference between two contours. Given two finite points sets $A = \{a_1, \cdots, a_p\}$ and $B = \{b_1, \cdots, b_q\}$, the Hausdorff distance is defined as

$$H(A,B) = \max\left(h(A,B), h(B,A)\right) \tag{2.22}$$

where $$h(A,B) = \max_{a \in A} \min_{b \in B} \|a - b\|$$

is called the directed Hausdorff distance from A to B. It identifies the point a $a \in A$ that is

farthest from any point of *B* and measures the distance from a to its nearest neighbor in *B*, that is $h(A,B)$ in effect ranks each point of *A* based on its distance to the nearest point of *B* and then uses the largest ranked such point as the distance. The Hausdorff distance $H(A,B)$ is the maximum of $h(A,B)$ and $h(B,A)$. Thus, it measures the degree of mismatch between two sets by measuring the distance of the point of *A* that is farthest from any point of *B* and vice versa.

2.5.6 Mean Absolute Surface Distance

The mean absolute surface distance tells us how much on average the two surfaces difference. This measure integrates over both over- and under-estimation of a contour, and results in an *L1 Norm* with intuitive explanation. The calculation is not straightforward if point to point correspondence on two surfaces is not available. We use a similar strategy as for the Hausdorff metric calculation, namely signed Euclidean distance transforms on one object and overlay of the second object surface. We then trace the surface and integrate the distance values. This calculation is not symmetric, since distances from *A* to *B* are not the same as *B* to *A*. Consequently we can derive a common average by combining the two averages. The mean absolute distance, as opposed to binary overlap, does not depend on the object size. However, it is only suitable for isosurface comparison.

2.5.7 Inter-/Intra- Class Correlation Coefficient

Intra-class correlation coefficient (ICC) is a descriptive statistic that can be used when quantitative measurements are made on units that are organized into groups [91]. It describes how strongly units in the same group resemble each other. A number of ICC estimators have been proposed. Most of the estimators can be defined in terms of the random effects model

$$Y_{ij} = \mu + \alpha_j + \varepsilon_{ij} \tag{2.23}$$

where Y_{ij} is the i^{th} observation in the j^{th} group, μ is an unobserved overall mean. α_j is an unobserved random effect shared by all values in group j, and ε_{ij} is an unobserved noise term. The measure calculates the ratio between the variance of a normally population and the "population of measurements", i.e. the variance of the population σ_α^2 plus the variance of the rater σ_ε^2. The intra-class correlation is thus defined as

$$\rho = \frac{\sigma_\alpha^2}{\sigma_\alpha^2 + \sigma_\varepsilon^2}. \tag{2.24}$$

If the rater variance is small relative to the total, then the variation in measurements among different cases will be due largely to natural variation in the population and thus close to 1.

2.6 CONCLUSIONS

Because of issues such as spatial resolution, blurry boundaries between the organs, noise, or acquisition artifacts, organic segmentation is a difficult task and futile to use gray-level information alone. Methods for performing segmentations vary widely depending on the specific application, imaging modality, objective regions and so on. There is currently no single segmentation method that can yield acceptable results for every medical image.

An earlier work divided the segmentation methods into two categories: region-based segmentation methods and boundary-based methods. In this chapter, we abandoned many excellent works but concentrated on an analysis methodology to conclude the segmentation process into 3 steps: Feature extraction. Propagation, which illustrates the mode of update functions. Fitness functions represent the statistic methods and classification strategy. We have reviewed the current state of the art in medical image segmentation. We summarized the characters of each method or its evolution.

Precision, accuracy, and efficiency factors have an influence on one another. Segmentation methods must be compared based on all three factors, as illustrated in an example wherein two methods are compared in a particular application domain. The weight given to each factor depends on application.

CHAPTER 3: 2-D ORGANIC REGIONS USING ACTIVE SHAPE MODEL AND GENETIC ALGORITHM

Shape is defined as a property which does not change under similarity transformations. Due to the prior knowledge of the target shape, shape model based methods are more stable against local image artifacts and perturbations than conventional low-level algorithms. Since their introduction by Cootes *et al*., active shape model has become one of the most popular model-based segmentation techniques in medical imaging. This approach includes two processes: *statistical model building* and *objects searching*. In this chapter we analyze the fundamental of 2-D statistical shape model construction. And proposed a new searching strategy to improve the limitation of shape description caused form linear PCA.

3.1 ACTIVE SHAPE MODEL METHOD

3.1.1 STATE OF THE ART

One of the extensions to the basic ASM algorithm was to improve the searching speed. As the multi-resolution approach was introduced for image processing, a coarse-to-fine search strategy was also applied to object searching [92]. The search starts at the coarsest level and switches to the next resolution when a predefined criterion is met. This procedure leads to a considerable increase in speed, robustness and commonly employed in all recent publications. In iterative processing, if the residual vectors could be composed and controlled separately, it is not doubt to increase the speed of convergence. Hill e*t al*.[93] used this idea: the error term from the model to object is split into two weighted parts, one normal vector of surface and one tangential. In experiment, weighting the tangential part lower than the normal, landmarks can slide along the surface more easily.

Another improvement of ASM is making efforts to the robustness of algorithm. Using the original ASM algorithm, if the initialization of model position is not suitable, searching result is disastrous. Duta and Sonka proposed to constrain the variation of model by comparing to the average point influence [94]. If it is too large, the point is considered an outlier and corrected based on the position of its neighbors. Lekadir *et al.* employed a shape metric based on the ratio of landmark distances to detect outliers. If a candidate point is located outside a trained confidence interval, a replacement point is suggested for further processing [95].

To relax the hard shape constraints of the original SSM, additional flexibility is added to refine the results. One approach to solving this problem is to run a normal ASM until convergence and to include an additional refinement step afterwards. The rationale behind this is that the model surface should be close enough to the real contour at that stage to be attracted with edge-based features. Local appearance usually plays an important role [96]. Another kind of methods is to integrate local energy minimizing strategy. Tsagaan *et al*. [97] model shape variation based on local curvature feature vectors, which are used to calculate covariance matrices during training.

3.1.2 MODEL BUILDING

To obtain an accurate segmentation result, information about common variations of biological objects must be included in the shape model. An approach to gather this information is to examine a number of training shapes by statistical means That is to say constructing a SSM basically consists of extracting the mean shape and the amount the pattern of legal variation from the collection of training samples. Generally the SSM building includes three steps. Training samples generation, obtain surface data from general medical images. Correspondence---search the corresponding points for each training sample which always relate to the biological surface characters. Alignment---dedicate to normalize the attitude of the training samples naturally and account the variation of the shape in this coordinate frame.

3.1.2.1 Correspondence

In this experiment, correspondence of landmarks was defined using manual landmarks, placed at points of anatomical significance. Such manual landmarking can often give acceptable results. For many applications, specialist anatomical knowledge exerts to identify consistent and reproducible points of anatomical significance. Good choices for landmarks including such as clear corners of object boundaries, “T” junctions between boundaries or easily located biological landmarks. However, there are rarely enough of such points to give more than a sparse description of the shape of the target object. We augment this list with points along boundaries which are arranged to be equally spaced between well-defined landmark points.

3.1.2.2 Alignment

In many cases, the size, placement, and orientation of an object are arbitrary. Only if remove these freedom (scaling, translation, and rotation), we have nothing to do with the actual variation of shape that we are interested in. Consider a fixed shape **y**, and a second moving shape **x**, which we wish to align with the first by means of a similarity transformation. A general similarity transformation acting on **x** can be written as:

$$\mathbf{x} \rightarrow \mathbf{y} : s\mathbf{R}(\mathbf{x} - t), \tag{3.1}$$

where t represents a translation, **R** is a rotation matrix, s is a scaling. The purpose of alignment is to find the similarity transformation which brings the moving shape **x** as close as possible to the fixed shape **y**. And then statistical analysis is used to give a parameterization of this variability, providing an appropriate representation and constraints. Fig. 3.1 demonstrates a serial of training samples of cardiac regions. We can see intuitively that the intrinsic shape of object become manifest when after align the training set.

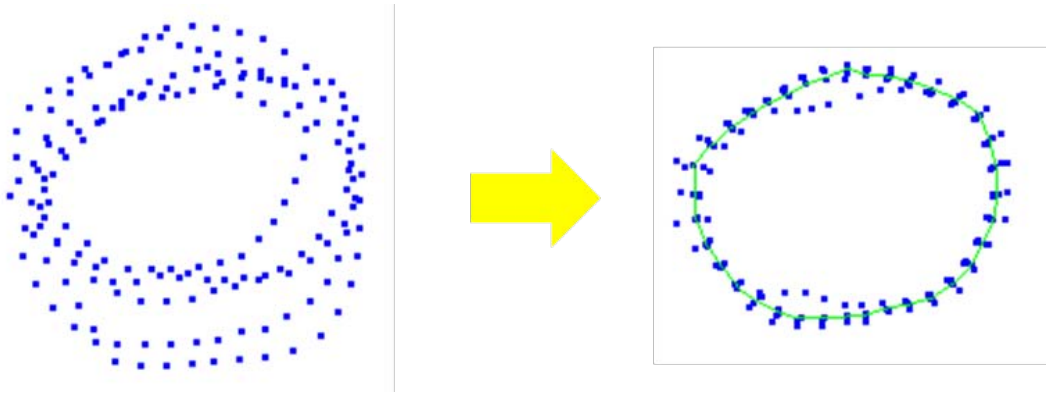

(a) (b)

Figure 3.1 Demonstration of alignment of 5 cases of cardiac training samples. (a) training samples on the preliminary state. (b) after alignment. Green line represents the mean position.

3.1.2.3 Shape analysis

After alignment, the next step is to reduce the dimensionality of the training set. We wish to analyze the statistics of distribution of shape vectors. To do this, we first need to find a set of axes specific to the particular set of shapes. We have in some sense already started to perform this, since we have a mean shape that can be used as an origin. PCA generates a coordinate system centered on the distribution, whose axes are aligned which the significant directions of the distribution, and represent modes of variation of that data.

For the statistical shape model construction, a parametric point distribution model has been developed for describing the segmenting curve by using linear combinations of the eigenvectors that reflect variations from the mean shape. The shape and pose parameters of this point distribution model are determined to match the points to strong image gradients. Every aligned 3-D training shape is described by 3n point coordinates in the vector $\mathbf{x}_i$; then the corresponding covariance matrix S is given by,

$$S = \frac{1}{N-1}\sum_{i=1}^{N}(\mathbf{x}_i - \bar{\mathbf{x}})(\mathbf{x}_i - \bar{\mathbf{x}})^{\mathrm{T}}, \tag{3.2}$$

where the mean $\bar{\mathbf{x}}$ is formed by simply averaging over all N samples. Eigen

decomposition on *S* delivers the principal modes of variation ϕ_i (eigenvectors) and their corresponding eigenvalues λ_i. A shape instance can then be generated by a linear combination of the first *c* principal modes

$$\mathbf{x} = \bar{\mathbf{x}} + \mathbf{\Phi b} = \frac{1}{N}\sum_{i=1}^{N}\mathbf{x}_i + \sum_{i=1}^{c} b_i\phi_i \,, \tag{3.3}$$

where $\mathbf{\Phi} = (\phi_1 \cdots \phi_c)$ are the matrix of eigenvectors and $\mathbf{b} = (b_1 \cdots b_c)$ are defined as shape weight parameters. Choosing the parameters **b** could generate a set of similar shape examples to the training set. If we assume that b_i are independent and Gaussian, then we can limit them by $|b_i| \leq 3\sqrt{\lambda_i}$. And to retain a given proportion δ of the variation in the training set, *c* modes can be chosen by satisfying

$$\sum_{i=1}^{c}\lambda_i \geq \frac{\delta}{100}\sum_{i=1}^{2n}\lambda_i \,. \tag{3.4}$$

3.1.3 Active Shape Model Search

In active shape model method, the factors of pose shift of model, such as translation, rotation and scaling is integrated. An instance of the model $\mathbf{x}'$ in an image is defined by a similarity transformation $\mathbf{T}_{t,s,\theta}$ based on the Eq. (3.3),

$$\mathbf{x}' = \mathbf{T}_{t,s,\theta}(\bar{\mathbf{x}} + \mathbf{\Phi b}) \tag{3.5}$$

where *t*, θ, and *s* show translation, rotation and scaling parameter respectively. Suppose now we wish to find the best transformation parameters and shape parameters to match a model instance $\mathbf{x}'$ to a new set of image points **y**. Minimize the sum of square distances between corresponding model and image points is equivalent to minimizing the expression

$$\left|\mathbf{y} - \mathbf{x}'\right|^2 \tag{3.6}$$

In searching process, we aim to adjust the pose parameters firstly and then remedy the pose residual offsets by shape parameters adjusting. If defining $d\mathbf{x_0}$ are the initial landmarks coordinate errors between model and actual position of object; dt are the translation errors between the mean model center and the object center; $d\mathbf{x}$ are a set of residual errors after pose adjustment in the local model coordinate frame. We can use geometry transform method to get dt, $d\theta$ and scaling factor (1+ds) from $d\mathbf{x_0}$ and then calculate shape adjustment amount $d\mathbf{x}$ by

$$d\mathbf{x} = \mathbf{T}_{s,\theta}((s(1+ds))^{-1}, -(\theta + d\theta))[\mathbf{y}] - \mathbf{x}, \tag{3.7}$$

where $\mathbf{x} = \mathbf{T}_{s,\theta}[\mathbf{x}] + d\mathbf{x}' - dt$. Note that the $\mathbf{T}_{s,\theta}$ is equal $\mathbf{T}_{t,s,\theta}$ but without the translation part. From Eq. (3.3)-(3.5), suppose the deformation is generated by first c principal modes and an approximation to calculate shape weight parameters variation is got by

$$\begin{aligned} d\mathbf{x} &\approx \mathbf{\Phi}(d\mathbf{b}) \\ d\mathbf{b} &= \mathbf{\Phi}^{\mathbf{T}}(d\mathbf{x}) \end{aligned}. \tag{3.8}$$

These two steps are conducted iteratively, until a specified convergence criterion is hit. More details of this algorithm can be found in [39]. A simple iterative approach to achieving this processing is as follow.

Algorithm 1:

1) *Initialize the shape parameters, **b** to zero (the mean shape).*
2) *Generate the model point positions using Eq.* (3.3)*.*
3) *Find the pose parameters (t, s, θ) which best align the model points **x** to the current found points **y**.*
4) *Project **y** into the model coordinate frame by inverting the transformation T:* $\mathbf{y}' = T_{t,s,\theta}^{-1}(\mathbf{y})$.
5) *Project y into the tangent plane to* $\bar{\mathbf{x}}$ *by scaling:* $\mathbf{y}'' = \mathbf{y}' / (\mathbf{y}' \cdot \bar{\mathbf{x}})$.
6) *Update the model parameters to match to* $\mathbf{y}''$ *by* $\mathbf{b} = \Phi^{-1}(\mathbf{y}'' - \bar{\mathbf{x}})$.
7) *If not converged, return to step 2).*

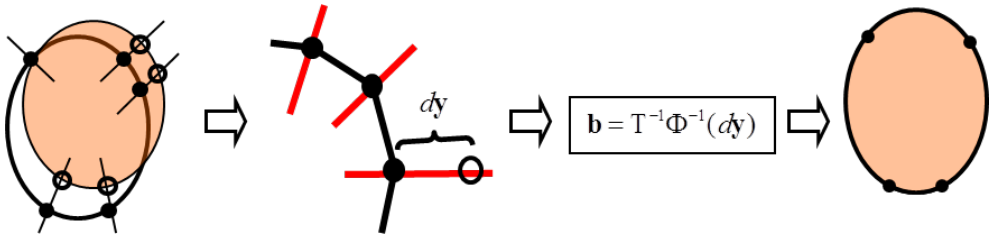

Figure 3.2 ASM searching processing. At the beginning, the model is located at near the positing of ROI. Local appearance models for all landmarks are evaluated at different positions perpendicular to the model. Calculate the transformation parameters and the deformation parameters. The best positions are searched by iteration.

3.2 OPTIMATE PARAMETERS USING GENETIC ALGORITHM

In original ASM description, a novel search algorithm using an iterative scheme was developed. The matching process of model and object was performed that measure the coordinate errors of landmarks and replace the landmarks by updating the pose parameters and shape parameters. However the pose parameters and the shape parameters have strong coupling which always brings operation redundancy and precision loss.

Genetic algorithm is a robust search method requiring little information to search effectively in a complex and multi-modal landscape. Here the GAs is used to find the parameters optimization to improve the precision and robust of objects searching process.

3.2.1 GENETIC ALGORITHM

Eq. (3.7) gives a way of calculating the suggested movements of the point $\mathbf{x}_i$ from the initial landmarks coordinate errors. However, in fact, this relationship is ambiguous. It means that it is hard to distinguish initial landmark errors deriving from the pose inexact or the shape variety. GAs is one of the resolutions to solve this optimization problem.

As the statement in section 2.4.5, GAs are efficient, adaptive, and robust search and optimization techniques guided by the principles of evolution and natural genetics, and have implicit parallelism. The essential components of GAs are the following: 1) a representation strategy called chromosomes; 2) a population of chromosomes; 3) mechanism for evaluating each string (fitness function); 4) selection/reproduction

procedure; and 5) genetic operators (crossover and mutation). The different steps of a GA process are as follows.

Algorithm 2:

1) *Initialize the population.*
2) *Decode the strings and compute their fitness values.*
3) *If termination criterion is attained, stop the process.*
4) *Else reproduce/select strings to create new mating pool.*
5) *Generate new population by crossover and mutation.*
6) *Go to Step 2).*

Here each individual gene in the GAs represents one variety defined by number of principal eigenshapes and pose parameters. The number of principal eigenshapes c can be calculated by Eq. (3.4); the pose parameters in 2-D image incorporate two translation parameters errors dx, dy, rotation $d\theta$ and scaling ds, respectively. Thus the number of real-valued genes on a GAs chromosome is c+4. Fixed-length individual genes are used here. We employ the linear ranking method as rank selection of an encoding. Noting that after initially place the model near the object manually, the range of translation adjustment and the rotation adjustment is not large. So reducing the encoding length represented them is advisable. We estimate the initial gene group with 150 genes and one-point crossover is implemented by swapping same length segments of genes between two individuals. Mutation is performed by changing the value of a gene on a certain probability. Here we choose mutation rates of 1[%].

3.2.2 FITNESS FUNCTION

The fitness function of GAs is based on the region texture evaluation by cross-correlation. The texture is defined as the pixel intensities across the object in question. The method to warp the image into normalized and collect the texture information in the same areas between two compared images is called piece-wise affine warp. In this experiment we constructed triangular mesh by connecting each landmark [99]. The normalized cross-correlation is proposed by normalizing the image and feature vectors to unit length and yielding a cosine-like correlation coefficient.

$$cc(u,v)=\frac{\sum_{x,y}[f(x,y)-\bar{f}][t(x-u,y-v)-\bar{t}]}{\sqrt{\sum_{x,y}[f(x,y)-\bar{f}]^2\sum_{x,y}[t(x-u,y-v)-\bar{t}]^2}} \tag{3.9}$$

where $\bar{t}$ is the mean of the feature in template and $\bar{f}$ is the mean of $f(x,y)$ in the region under the feature.

The flow of procedure is shown in Fig. 3.2. Shape and texture information are derived from the training images. Use "the strongest image edge" to research a suggested movement for landmark errors as done in ASMs. The genes of GAs are derived from the shape parameters and the pose parameters and adjusted by valuation of GAs. The selection, crossover and mutation are performed sequentially until getting an accepted precision. The algorithm is described as below.

Algorithm 3:

1) *Initialize position parameters and shape parameters. Same like step 1 of Algorithm 1.*
2) *Generate the shape using new set of parameters.*
3) *Require the object image I_0 which is encircled by the model.*
4) *Calculate the normalized cross-correlation value $cc(I_0, I')$.*
5) *If this value is more than the threshold end the processing.*
6) *Else, generate a set of new parameters using GAs and return step 2).*

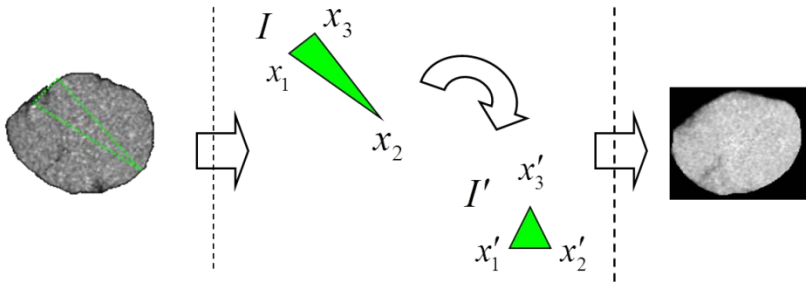

Figure 3.3 Piece-wise affine transformation. Divide the separated region into certain number of triangular regions. Normalize the shapes of these regions. Combine the normalized triangles to generate the normalized appearance model.

3.3 EXPERIMENT RESULTS

3.3.1 DATA SET

The lung segmentation results: contains 5 chest CT images of size 512×512 and 12 bits gray scale in Hounsfield units. Both lung fields have been delineated manually and the left and right lungs are modeled independently.

3.3.2 EXPERIMENTS OF MODEL BUILDING

Training examples extracted from 5 cases of volumes consisted of 35 landmarks, which had been corresponded manually. The alignment processing was completed using affine transformation. We tested the PCA to decompose the variation of shape into "domain modes". Fig. 3.4 demonstrates the first 4 modes of variation, which are corresponding to the first principal components.

3.3.3 EXPERIMENTS OF SEGMENTATION

Proposed method was performed on segmentation both of lung field and cardiac field segmentation from chest CT images. The compartments of the experiments between manual segmentation and automatic segmentation using proposed method are shown in Fig. 3.4. And evaluate the results using set theory described in the section 2.5.2. The average fitness is 91.0[%]. The cardiac segmentation results: contains 5 chest CT images of size 512×512 and 12 bits gray scale in Hounsfield units. The average fitness is 81.7[%].

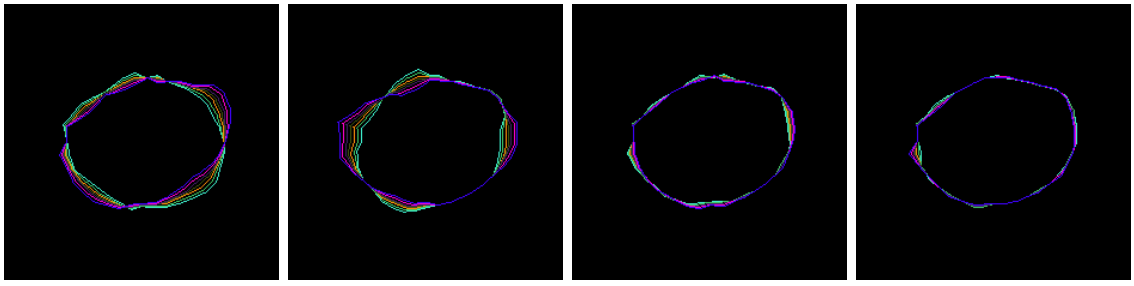

(a) (b) (c) (d)

Figure 3.4 The first 4 principal modes of cardiac shape deformation.

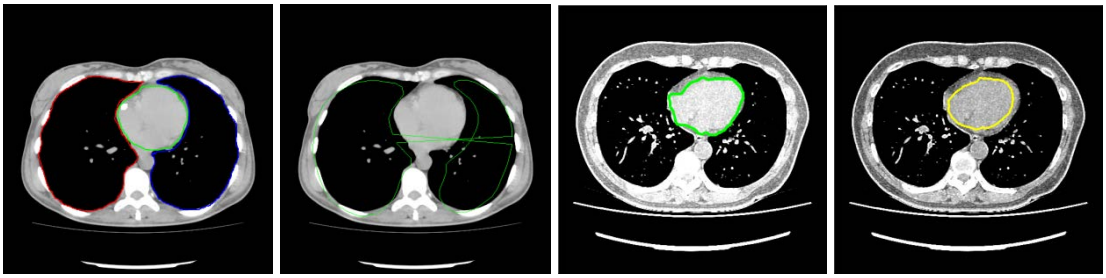

(a) (b) (c) (d)

Figure 3.5 Segmentation results. (a) Gold standard. (b) Automatic segmentation result of lung region. (c) and (d) demonstrates two slices of segmentation of cardiac regions.

3.3.4 DIVISIONAL SEGMENTATION METHOD

We expend the mentioned 2-D model method to 3-D space. In practice, the difference between the slices in cardiac regions is not obvious within certain limits. To obtain an integrated cardiac region from CT images, we divided the cardiac into 3 groups. 2-D boundary shapes in the same group should be guaranteed as similar as possible. The details are shown in Fig. 3.6.

- Up group：since it is the point of junction with main artery and main vein, shape of these regions are complex.
- Middle group: shapes of these regions appropriate to circle. However the deformation is severe along with the cardiac cycle.
- Bottom group : shapes of these regions are relative regular. However, the blur between cardiac and liver always induces the enormous difficulties to extract the ROI.

We experimented 10 cases of segmentations of cardiac regions that each case included 10 slices. We compared the automatic segmented results with the gold standards, which had been delineated by radiologists. The average of fitness of all cases was 86.1%.

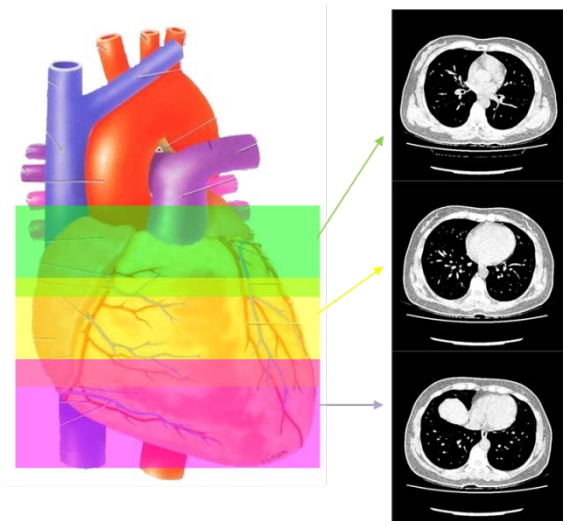

Figure 3.6 Divide the cardiac regions into 3 groups.

Table 3.1 Fitness results.

I. Fitness results of lung region

Case	1	2	3	4	5	***Ave.***
TPR[%]	94.5	89.3	92.5	91.5	87.2	91.0

II. Fitness results of cardiac region with 3 groups

Case	***TPR***[%]										
	up group(1-3)			middle group(4-7)				bottom group(8-10)			***Ave.***
1	91.2	89.7	91.4	86.3	83.7	88.0	79.1	81.2	81.7	53.8	82.6
2	85.0	88.2	88.8	92.0	92.7	93.6	92.4	91.9	88.5	84.2	89.7
3	88.8	82.4	82.9	86.4	76.4	75.4	76.9	78.4	75.8	71.6	79.5
4	80.3	87.1	89.2	91.1	91.2	89.5	81.2	77.7	57.2	32.8	77.8
5	73.4	83.4	91.2	90.6	93.5	90.8	90.8	88.5	86.2	69.0	85.8
6	82.0	86.9	89.5	92.4	94.3	89.5	88.7	86.0	86.0	73.3	86.9
7	91.5	89.6	92.6	91.7	91.0	89.8	94.2	93.4	93.5	68.9	89.6
8	88.1	89.5	92.1	93.0	94.5	93.2	94.6	83.4	89.1	79.4	89.7
9	92.2	91.2	93.6	91.3	93.2	91.1	89.7	90.7	91.5	78.9	90.3
10	88.1	89.9	88.6	89.9	89.2	91.2	94.0	83.4	86.9	88.0	88.9
											81.8

3.4.5 DISCUSSION

From Fig. 3.3 we can see that although any dependencies between the parameters would imply nonlinear relationships between the original point positions but according to vary the first four parameters separately we can generate “illegal” shapes. Each of the parameters represents a mode of variation of the shape which can frequently be associated with an intuitive description of the deformation. When enlarged the conjunct region of cardiac and chest (preprocessed by sobel filter, in Fig. 3.7) we can see that the edge information is quite weak. At the same time, the length of this part occupies a large proportion. For this region, it becomes more difficult to search them when using ASMs.

The segmentation results of lung CT image perform well, and the accuracy can be expected with the built shape model. But the errors of cardiac field segmentation are a little larger than accepted. Cootes *et al*. pointed out that the shape models described using PCA is a linear combinations of the shapes in the training set. In order to be able to match well to a new shape, the training set must exhibit all the variation expected in the class of shape modes. If the shape variation does not follow a Gaussian distribution, the presented constraints for shape weight parameter b will possibly result in invalid shapes. Park *et al*. [99] analyzes the cardiac motion with parameter function. They construct a 3 dimension coordinate with the axis direction defined as same as volume direction definition of CT scan. The formulation of deformations with continuous parameter functions is general and can be applied to any underlying shape *e*. The model is approximated

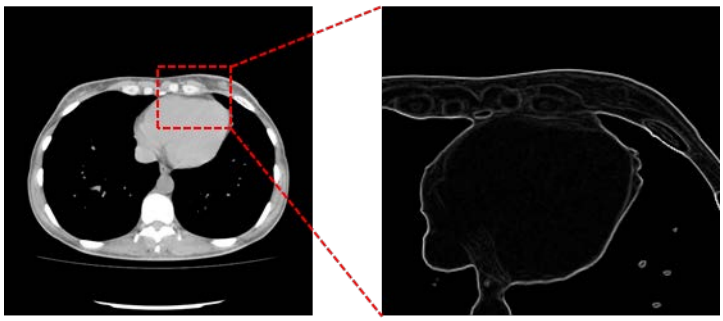

Figure 3.7 Enlarge view of edge map image of boundary between cardiac and chest.

$$\mathbf{s_t} = \mathbf{T_t}(e; \tau(u)) = \begin{pmatrix} e_1 \cos(\tau(u)) - e_2 \sin(\tau(u)) \\ e_1 \cos(\tau(u)) + e_2 \sin(\tau(u)) \\ e_3 \end{pmatrix}, \quad (3.8)$$

where τ(u) is the twisting parameter function along the z axis. From this function the non-linear variety of cardiac shape is known. By employing the radial contractions, this variety of cardiac in the radial direction during systole is approximately 20-25[%]. There were several non-linear extensions to the model. However, it seems that the model approaches must assume that varying the parameters **b** within given limits the plausible shapes in training set can get an effect.

3.5 CONCLUSIONS

In this chapter, we proposed a method that use genetic algorithm to pursue the pose parameters and shape weight parameters. And perform this method on lung field segmentation and cardiac field segmentation for CT images. The results of lung field segmentation performed well. But the task of segmentation of cardiac fields shown that linear PCA model has a limitation on the segmentation of largely deformable organs.

The main challenges and issues in integrating GAs for solving the optimization problems in medical image segmentation are manifold. First, the encoding strategy must be suitably defined so that it conforms to the building block hypothesis. Second, since computation of fitness function is the most time-consuming part, its efficient design is crucial for a successful application of GAs. Third, incorporation of expert knowledge and integration with local searching are ways to enhance the convergence rate.

Although shape representation from a successful 2-D “thin-slice models” could facilitate procedure of model building, 3-D model method is still the tendency. There are three main benefits to using 3-D models. Firstly, data quantity could be reduced. It is clear that when using slice-by-slice method, we have to describe shape character for each slice that increases the number of required landmarks considerably. Secondly, according the positions of selected slices seems impossible, i.e. if we index the selected slices, due to the shape deformation it is not able to confirm that the anatomical structures in the slice of the same index are correspondent. For these reasons, building a 3-D shape model is urgent. In following two chapters, we discuss the 3-D shape model building methods.

CHAPTER 4: ALIGNMENT OF 3-D MODELS

As the light of previous chapter, the difference of shapes among a class of objects generally could be decomposed into two items: global transformation and deformation. Note that the transformation should not be modeled by an SSM in order to keep the model as specific as possible. As a set of surface samples, if their PDM has been established (i.e. the landmarks have been corresponded), generalized Procrustes analysis (GPA) algorithm is no doubt an alternative alignment method. However in some cases, the correspondence processing adjoins the attitude of surface samples, i.e. alignment processing should be performed previously. For example, in some surface parameterization methods, correspondence results are affected from rotation transformation. Hence we should reconcile the orientations of surface samples firstly. In this chapter, we propose a feature-based alignment method to reconcile the surface samples of by their Gauss maps.

4.1 STATE OF THE ART

The alignment problems of training shapes can be summarized as a transformation between the same anatomy images at different modalities. The most famous method is usually obtained by minimizing the sum of squared distances between corresponding landmarks on all examples, which is known as Generalized Procrustes Analysis (GPA) [100, 101]. Some other novel strategies were reported to optimize measures such as the average distance between each representative point, or iterated minimal distances metric [102]. In [103,104], authors contributed a Gaussian Mixture Model (GMM) that solved the alignment of two point sets as a probability density estimation problem. Feature-based alignment is largely founded on the use of differential geometry to describe local surface feature [105]. According to the difference of local feature on parameterized space, an appropriate transformation could be required. The statistical model building would

benefit from this technology, because the landmarks positions always involve the local features of surface. It is also applied in the structure alignment of 4D CT images [106].

4.2 POLYGONAL SURFACE GENERATION

4.2.1 REQUIREMENT OF VOXEL SURFACE

The ROI has to be extracted by experts in all CT images in the training set. Here, semi-automatic approaches (region growing, etc.) are used to segment the interest parts previously and then correct the results by radiologists. With the ImageJ(R) [107] a manual segmentation of liver from CT images (120 slices) takes about 40 minutes.

The key point in generation of voxel surface processing is guarantee of surface is isolate, i.e. there are not holes and self-intersections inside of the region. The processing is described as Fig. 4.1. Support connected region B is ROI with some isolated holes noted as un-connected region C. D is also un-connected that represents self-intersections. A is noted as the other region, such as background. We assume A is connected. Now, we attempt to fulfill the region $B \cup C$ as an isolate region. Using region growing method, we just obtain the connected region A and B, separately. The processing is like that. Firstly, get connected region B, label this region with “true”. Label the other regions, including A, C, D, with mark “false”. Such, the region A and D become connected, denote as AD. Secondly, fulfill the connected region AD an label it as “false”. Naturedly, the remained region B and C become connected what is we want. The fulfilling method is also used for the segmentation of lung regions, described in section 6.1.2.

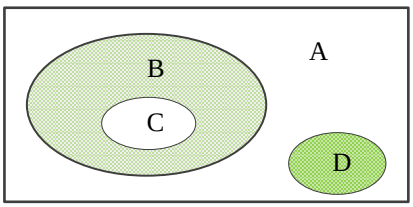

Figure 4.1 A Venn diagram illustrating the fulfill procedure. B and C present ROI. A and D present background regions. A and B are connected regions.

4.2.2 MARCHING CUBES

In the digital geometry processing field, surfaces are generally represented as triangular meshes, which are developed by many geometric theories and supported by common graphics hardware directly. Any other image representations, such as volume, implicit surfaces, need to be converted to triangular meshes for display purposes. In medical imaging, triangular surfaces are always generated from volume data of medical image. Marching Cubes algorithm introduced by Lorensen and Cline is a well-known polygonal isosurfaces generating method from volumetric data sets [108]. The basic principle behind the marching cubes algorithm is to subdivide space into a series of small cubes. Then test the mode of each corner points through each of the cubes, “march” the mode by looking up the table, and replace the cube with an appropriate set of polygons. The sum total of all polygons generated will be a surface that approximates the one the data set describes.

Let us look at a 2-D example. Fig. 4.1 shows a solid circle which is seem as the ROI. Our purpose is representing the boundary using a set of line segments. The first step is dividing this region using lines into a serial of cells. The corners that are inside the ROI are enhanced by the green dots. According to the statements of corners in each cell (whether it is inside of the ROI or not), we can guess the intersection points of the boundary and the edges (pink dots). Connect these approximate vertices to construct a polygonal boundary.

Substitute the cubes for cells, as the standard Marching Cubes algorithm has done, in Fig. 4.2, we list the polygon generating modes. The rectilinear lattice is constructed by successive two slices S_k and S_{k+1} in 3-D space. And a lattice becomes to a cube, which have 8 corners and a potential 256 possible combinations of corner status.

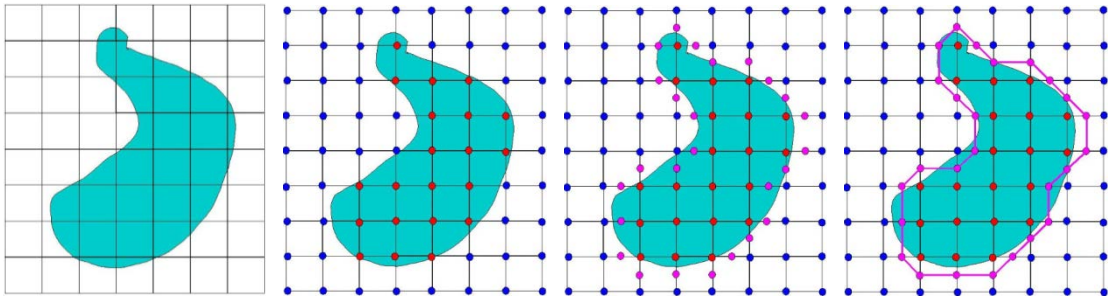

Figure 4.2 Illumination of Marching. (a) A discrete image of lung region. (b) Record the states of the corners: inside the region (red) or not (blue). (c) According to the states of 4 corners of each lattice, intersect the polygonal points (pink points) to each edge. (d) Connect the intersection points to construct an appropriate boundary.

4.2.3 DELAUNAY MESH

Delaunay triangulations have been studied extensively in computational geometry and have found applications in many fields, including numerical analysis, computer graphics, image processing, and geographical information. Delaunay triangulation finds the triangulation that maximizes the minimum angle of all triangles, among all triangulations of a given point set. This presentation has a number of nice theoretical properties that make it very popular in computational geometry. Unfortunately, surface mesh obtained by Marching Cubes algorithm cannot satisfy this condition for all vertices. The most popular way to tackle this problem is the Delaunay swap criterion and the geometry-preserving algorithm, which is split triangles by inserting new vertices or designs a convex combination map with good properties. In this study, we use the flipping algorithm [110] to solve this problem.

4.3 ALIGNMENT USING SURFACE GAUSSIAN MAPS

4.3.1 ORIENTATION OF A SHAPE

The orientation of a shape is defined as a property which does not change under the rotation transformation, i.e. all the geometrical information that remains when location, scale and rotational effects are filtered out from an object. Benefit from the Gauss map,

the surface Gaussian curvature could be reflected on the 2-D spherical surface. According to analyzing the surfaces of one class of objects, we can facilitate to obtain the estimation of geometric attributes such as curvature distribution, uniform continuity and smoothness, which are invariant to rotation.

Fig. 4.3(a) demonstrates mapping a two dimensional shape of left lung to a sphere. The cambered surface patches which have continuous curvature are mapped continuous regions on Gauss map spherical surface. The plane part P_1P_3 is concentrated into a point n_0. The patch P_1P_2 is convex line segment, the mapping is continuous from n_1 to n_2. The concave patch P_2P_3 is reflected to n_3n_4 with the anti-clockwise. Since the discontinuity of curvature among the regions of surface, the mapping points aggregate to some separations. The modalities could be inferred from this global distribution. If we use spherical coordinate to expression the points on Gauss map again. Define θ is the inclination angle measured form a fixed zenith direction, and ϕ is the azimuth angle. Unfolded Gauss map according to the spherical coordinates, the texture of the Gauss map is like Fig. 4.3(b). The distribution of map of vertices can be observed to some points classifiers obviously. More samples of unfolded Gauss maps of left lung are listed in Appendix A.

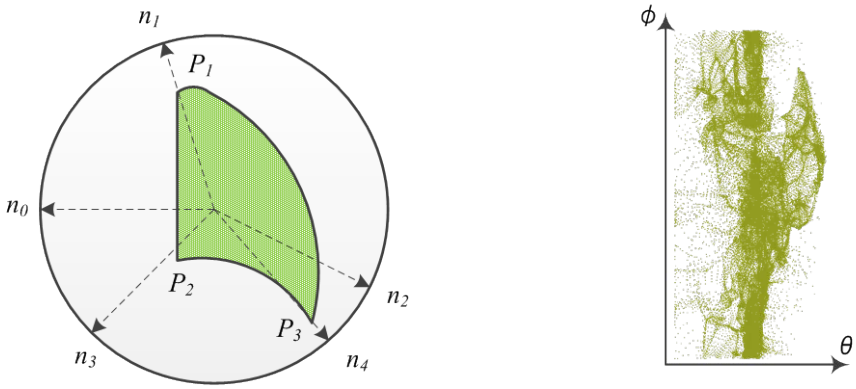

(a) (b)

Figure 4.3 Demonstration of Gauss map. (a) Illumination of the process of Gauss mapping. (b) Unfold the Gauss map of a left lung surface.

4.3.2 DISCRETE GAUSS MAPPING

The Gaussian curvature of a point on a surface is an intrinsic measure of curvature, i.e., its value depends only on how distances are measured on the surface. The Gauss-Bonnet theorem links total curvature of a surface to its topological properties [111]. The theorem also has interesting consequences for triangles. It could be accounted as follows:

Gauss-Bonnet theorem: Suppose D is a simply connected region on the surface, ∂D is a piecewise smooth closed curve, k_g is called the geodesic curvature of the curve. Assume α_j are the outer angles of the vertices of ∂D. Then

$$\int_D K_p dA + \int_{\partial D} k_g ds + \sum_j \alpha_j = 2\pi . \tag{4.1}$$

If the geodesic curvature is smooth, then

$$\int_D K_p dA + \sum_j \alpha_j = 2\pi . \tag{4.2}$$

The integral operation will be replaced by the accumulated sum operation, when we consider the piecewise polygonal surface.

Fig. 4.4(a) shows a polygonal cell with three faces adjacent a vertex V_i. G_j represents one point in the unit triangular face $V_iV_{i+1}V_{i+2}$, and the norm n_j joints this triangular face at it. As the normal direction of each polygonal plane face is special, mapping this unit face to a point on the Gaussian sphere still makes sense. G'_j is the corresponding point of G_j on Gauss map, in Fig. 4.4(b), and it also used to represent the mapping of the face $V_iV_{i+1}V_{i+2}$. According to the angular variety of the two vertices G_j, G_{j+1}, the line segments G_jM, MG_{j+1} could be projected to the spherical segment $G'_jG'_{j+1}$. In the same way, mapping of the vertex V_i is loaded inside of the simple connection of the region $G'_jG'_{j+1}\ldots G'_{j+s-1}$, because the original surface is smooth and continuous.

Support α_j are the outer angles of the cell. Because the Gaussian curvature on the Gauss sphere is one everywhere, from the Eq. (4.2), the area of cell A_i could be simplified by

$$A_i = 2\pi - \sum_j \alpha_j = (2-n)\pi + \sum_j \beta_j \tag{4.3}$$

where β_j is the intersection angle between two spherical segments. Since spherical segments $G'_jG'_{j+1}$ and $G'_jG'_{j+s-1}$ are the mapping of the segments G_jMG_{j+1} and G_jNG_{j+s-1} respectively, if denote the projective angle of β_j as β'_j, it is not difficult to proof that β'_j approaches to β_j. As well as

$$\gamma_i + \beta'_i = \pi$$

then

$$A_i = 2\pi - \sum_j \gamma_j . \tag{4.4}$$

The right part of this equation is the total Gauss curvature at vertex V_i. So, this equation illustrates that the area of the spherical polygonal cell on Gauss map could be applied to estimate the curvature of the original piecewise polygonal surface. When we minimized the area A_i, the norm of the vertex V_i could be approximated by the sum of the norms of the faces around V_i.

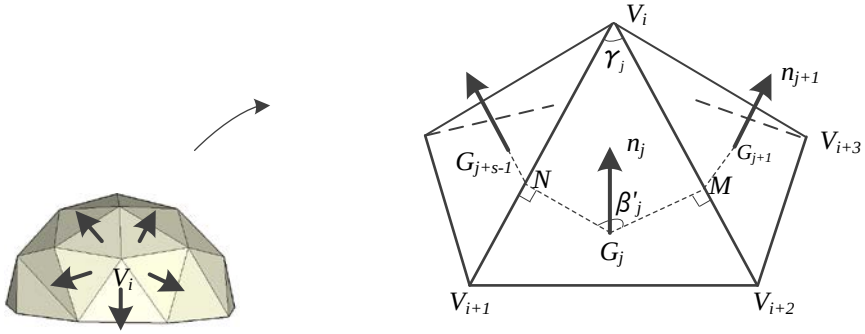

Figure 4.4 One polygonal cell around a vertex and its normal computing method. Sum of norms of triangular faces adjacent a vertex approximate the norm of vertex. G_j is one point on face $V_iV_{i+1}V_{i+2}$. Its mapping point is G'_j on Gauss map.

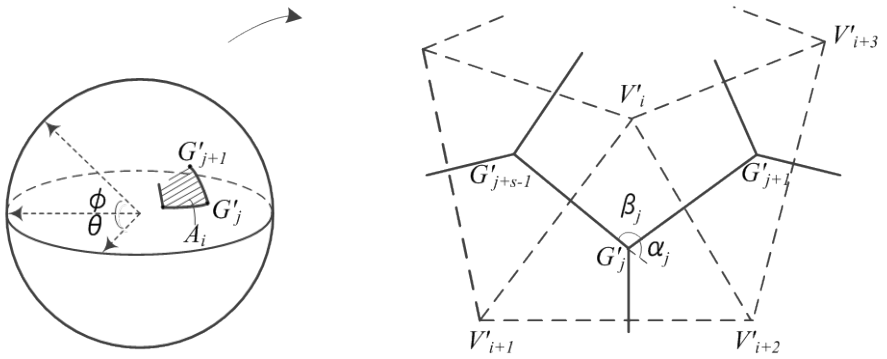

Figure 4.5 One polygonal face unit on Gauss map. β_j is an inner angle of polygon $G'_j \cdots G'_{j+s-1}$. α_i is exterior angle. The area of cell could be calculated from inner angles.

Generally, the normal to a surface have a pair opposite directions. For a surface which is the topological boundary of a set in 3-D, one can distinguish between the inward-pointing normal and outer-pointing normal. For an oriented surface, the surface normal is usually determined by the right-hand rule, as Fig. 4.6 (a). If the total curvature is positive, the local region of surface is convex along the norm direction. In contrast, if *n* is negative, the orientation of reflected curve on Gauss map is inverse again the original curve. On the other hand, the norm of *n*, i.e. the area ration between a surface region and area of its Gauss image could be illustrated the bent degree. Consider a curve unit of an orientable triangular surface in Fig. 4.6(a), which includes two triangular faces. If we defined the positive orientation of a face as clock-wise, the orientations of all the faces of this regular surface are same. The mapping unit of a local region with positive curvature does not change the original orientation. The norms are crossed when the angle of two surface faces is less than π. The orientations of their mapping are negative. Fig. 4.6(b) demonstrates the distribution of total curvature of a lung triangular surface. Regions where the curvature is negative are marked in red color.

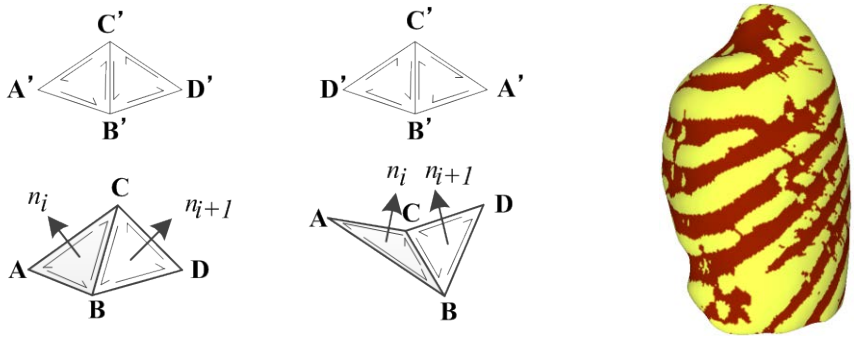

(a) (b)

Figure 4.6 Total curvature of piecewise triangular faces. (a) Illustration of the mapping of a curve unit. The sub-pictures on upper row are the Gauss map of their corresponding units on the lower row (b) the demonstration of total curvature of a lung triangular surface.

Whilst the areas of piecewise faces are not consistent, the distribution of vertices cannot reflect areas of local regions. Here we add a weight to each vertex, and treat the vertex as the mass center of an infinitesimal area. In [112], authors propose a local spatial average of 1-ring neighborhood for triangular mesh surfaces and provide an approximation of Voronoi area A as

$$A = \frac{1}{8} \sum_{j \in V_i} (\cot \alpha_{ij} + \cot \beta_{ij}) \| V_i - V_j \|^2 \tag{5.5}$$

where V_i, V_{i+1} are two vertices connected to an edge. α_{ij} and β_{ij} are the two angles opposite to the edge in the two triangles sharing the edge (V_i, V_{i+1}).

4.3.3 Statistical Method Using K-Means Clustering

Unfold the Gauss map according to the spherical coordinates, as Fig. 4.3(b) demonstrated, cluster of the mapping point sets is obvious. The intensive regions correspond to the main faces which are relative flat on the original polygonal surface of organic model. Following this viewpoint, if found a metric to measure the distances between the main surfaces, the alignment of two surface could be achieved.

The cluster method is used to describe the distribution of the point sets. In detail, here we use the K-means clustering algorithm to divide the point sets on 2-D Gauss map. The centroid of a cluster, denoted as the representative point, is the average point in the multidimensional space defined by the dimensions. In a sense, it is the center of gravity for the respective cluster. In this method, the distance between two clusters is determined as the difference between centroids. Reference [113] provides a boosting algorithm which uses kd-tree structure. The number of the classifiers is 21 and the initial seed points' positions are set averagely (Fig. 4.7(a)).

The solution of the rigid parameters solution is based on Berthold B.K.P. Horn [114]. The author provides a method to decompose the effects from the translating, scale and rotation. It is a coarse alignment method and could give a simple solution when all the points are coplanar. It has been inferred that to require the translation minimize, just align the centers of gravity of two point sets. Referring to the scale factor, actually it need not be considered, for all surface maps are in the unit sphere. The remaining task about the rotation is the solution of a least squares problem in a plane, as Fig. 4.7(b) The vector $v_{l,i}$ points from one representative point to the centroid on Gauss map of referent model, Corresponding it $v_{r,i}$ is on the sample model. α_i represents the angle between these two vectors pair. The solution of the rotation amounts to minimize the Euclidean distance of corresponding vectors. The optimized deviation angle θ could be calculated by

$$\sin\theta = \pm\frac{S}{\sqrt{S^2 + C^2}} \tag{4.6}$$

where $C = \sum_i (v_{l,i} \cdot v_{r,i})$, sum of the inner products of vectors. $S = \sum_i (v_{l,i} \times v_{r,i})$, sum of the cross products of vectors. More details could be found in section 4.3.5.

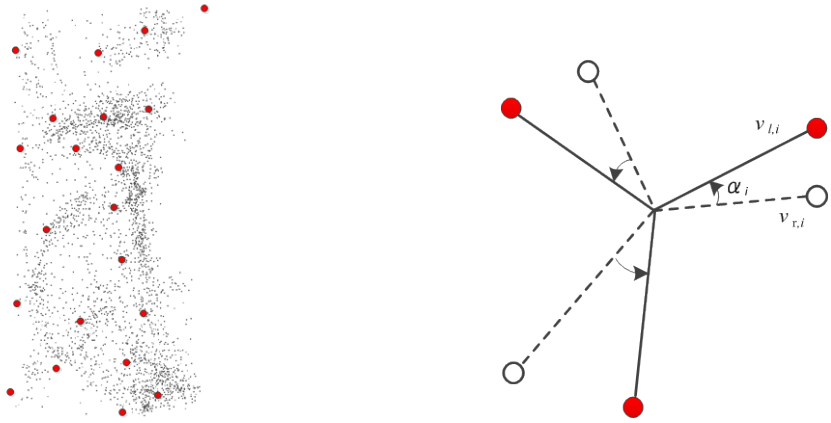

(a) (b)

Figure 4.7 Alignment method illustration. (a) On unfolded Gauss map, representative points are obtained using k-means clustering. (b) Rotation parameter optimization. Two set of representative points are represented in white color and red color respectively. Coincide the centers of these two point set, and make it as the original point.

4.3.4 Statistical Method Using Stereographic Projection

There is a inhere defaults in the proposed method of previous section. Since the rotation of object in 3-D space is limitless, however, when we map the spherical surface into a plane region with boundary, Gauss map has to be divided. Hence, the surface model would not be rotated with a large angle, due to its map in plane might be out of the boundary. Alignment method is helpless. In this section we break the limitation of boundary of map by means of stereographic mapping method. The spatial surface models could be adjusted with the whole 3 freedom of rotation.

4.3.4.1 Principle of stereographic mapping

The stereographic projection is a particular mapping that projects a sphere onto a plane. Define a stereographic projection of a unit sphere is $SP(x, y, z)$ and its inverse is $SP^{-1}(u, v)$, as shown in Fig. 4.8(a). Let plane $z = 0$ go through the center of the Gaussian sphere. Denote coordinates (0, 0, 1) on as the “North Pole”; (0, 0, -1) as the “South Pole”; the complex plan intersect the “equator” of the sphere. Using Cartesian coordinates (x, y, z) on the sphere and (u, v) on the plane, the projection and its invers are given by the formulas:

$$SP(x, y, z) = \frac{x}{1-z} + i\frac{y}{1-z}$$
$$SP^{-1}(u, iv) = (uT, vT, 1-T) \tag{4.7}$$

where $T = \frac{2}{1+u^2+v^2}$ and i is imaginary symbol.

Generally, for any point P on the Gauss map, there is a unique line through North Pole and P, and this line intersects the complex plane in one point P`, which is represented as the projection of P. In this way, the lower hemisphere is mapped inside the unit circle. As well the upper hemisphere is mapped outside the unit circle. It is not convenient for statistic of the upper hemisphere, since the small neighborhoods of the North Pole are sent to subsets of the plane far away from the equator. Here we propose a symmetrical way that connecting the South Pole and the point on upper hemisphere. The intersected point with complex plane is located inside the unit circle but the lower face, as Fig. 4.8(a). The complex plane has two faces which are denoted as C^+ and C^- separately. Support (x, y, z) are the Cartesian coordinates on the sphere and (u, v) are the complex coordinates on plane, the projection is given by the formula

$$u + iv + kw = \frac{x}{1+|z|} + i\frac{y}{1+|z|} + k \cdot \text{sign}(-z) \tag{4.8}$$

where k is used to distinguish the surface of plane. “sign” operator gets the sign of z coordinate.

The projection mapping is smooth and conformal, but not preserving area. So we should product a weight to translate the statistic on plane to the equivalent value on sphere. If denote dA_s as the area element of the sphere and dA_p is its coordinated area element on the plane, the weight can be calculated as

$$dA_s = \frac{4}{(1+u^2+v^2)^2} dA_p . \tag{4.9}$$

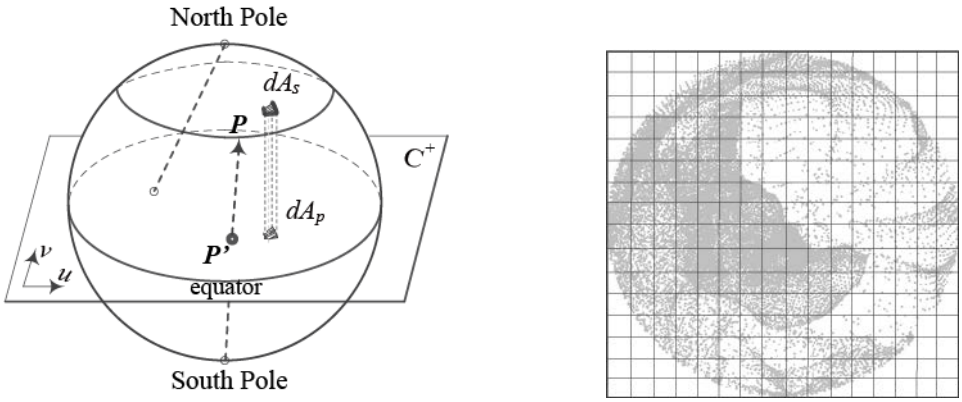

(a) (b)

Figure 4.8 Demonstration of stereographic projection. The bifacial complex plane C^+ is denoted as the upper hemi-plane. Point P is a point on the upper sphere. Its projection is mapped to P' on C^+. dA_s is an infinitesimal area on upper sphere and it is mapped as dA_p on C^+. (b) is an example of stereographic projection image of Gauss map of left lung.

4.3.4.2 Fitness function

So far, we have translated the three dimensional surface statistical problem to a two dimensional plane. On the complex plane, we divide the circumscribed squares of the mapping circles into small sub-regions equally. Count the total of the mapping points of the vertices in each region. Then multiple the correspondent weights, described by Eq. (4.9). The result is used as the metric to estimate the intensity of unit region on Gauss map. According to compare the matric of the object shape to the matric of reference model, we can obtain the best rotation transformation of the object training shape, as Fig. 4.8(b), mapping result of gauss map of lung polygonal surface. We can distinguish the significant distribution of mapping vertices.

The next necessary is an optimizer that we need an iterative algorithm to change the modality of Gauss map and compare the statistical value in the different modality. Experimentally, the variation range should be limited to increase the robustness and the algorithm speed. Here we use a fast random rotation matrices for iterate operations, which is described in [115]. The whole procedure of proposed method is described below.

Algorithm 4:

Input (mesh *M*, block statistic of reference shape *RefVal*, loop time *t*, initialized coefficients of rotation matrix r_0).

1) *Calculate the density coefficient A for each vertex on the original triangular surface.*
2) *Get the Gauss map of vertieces.*
3) *Get the stereographic projection of vertieces on Gauss map.Two hemispheres are mapped to two discs separately.*
4) *Calculate the projection area coefficient for each vertex using Eq.* (4.9).
5) *Count the block statistic on plane and normalization. Require the metrics of sub-regions.*
6) *Campare the statistical metrics of object to the RefVal. Require the error of comparision δv.*
7) *If reach the loop time, return the coefficient of rotation matrix r, when δv is the minimum. Else, rotate the Gass map of object randomly by rotation matrix. Repeat 3)-6).*

4.3.5 TRANSLATION AND SCALING

According the argument above, we have solved the rotation transformation regarding the surface features. However, how to solve the translation and scale factors?

Suppose *n* landmark points are placed on each training sample. Reset the original point of each shape to its mass center. Denote that the regulated vector of fixed points set on reference model is y_i and vector of moving points set on training sample is x_i. An alignment problem on relative measured coordinates could be described as follows to minimize the residual error sum of the length of responding points, i.e.,

$$\sum_{i=1}^{n} \left| \mathbf{y}_i - s\mathbf{R}\mathbf{x}_i - t \right|^2 \tag{4.10}$$

or

$$\sum_{i=1}^{n} \left| \mathbf{y}_i - s\mathbf{R}\mathbf{x}_i \right|^2 + t\left(nt - 2\sum_{i=1}^{n} \left| \mathbf{y}_i - s\mathbf{R}\mathbf{x}_i \right| \right), \tag{4.11}$$

where **R** represents the rotation matrix. *s* is scaling factor. *t* is translation value of training samples. Now the sum in the middle of this expression is zero since the measurements are referred to the centroid. The first term does not depend on *t*, and the last term is

nonnegative. The total error is obviously minimized when $t = 0$, i.e., when the centroid of fixed points set and the centroid of moving points set coincide. The first term of Eq. (4.11) could be decomposed as

$$\sum_{i=1}^{n}\left|\mathbf{y}_i\right|^2 - 2s\sum_{i=1}^{n}\left|\mathbf{y}_i\mathbf{R}\mathbf{x}_i\right| + s^2\sum_{i=1}^{n}\left|\mathbf{R}\mathbf{x}_i\right|^2 . \tag{4.12}$$

As in relative measured coordinates, the centroid has been moved to zero, the rotation is a linear operation and it preserves lengths

$$\sum_{i=1}^{n}\left|\mathbf{R}\mathbf{x}_i\right| = \sum_{i=1}^{n}\left|\mathbf{x}_i\right|. \tag{4.13}$$

Denote

$$Y = \sum_{i=1}^{n}\left|\mathbf{y}_i\right|^2,\ X = \sum_{i=1}^{n}\left|\mathbf{x}_i\right|,\ D = \sum_{i=1}^{n}\left|\mathbf{y}_i\mathbf{R}\mathbf{x}_i\right| = \sum_{i=1}^{n}\left|\mathbf{y}_i\mathbf{x}_i\right|,$$

then aforementioned formula (4.12) could be re-expressed as

$$Y - 2sD + s^2X = \left(s\sqrt{X} - \frac{D}{\sqrt{X}}\right)^2 + \left(Y - \frac{D^2}{X}\right). \tag{4.14}$$

This is minimized with respect to scale s when the first term is zero or

$$s = \frac{D}{X}. \tag{4.15}$$

Generally the registration of two different shapes is a nonlinear processing. When we exchange the fixed points set and the moving points set, approximate y_i to x_i, the registration result will be different from the original matching pattern. To facilitate the procedure, here we utilize a symmetrical system that ignores this difference. It is described as

$$\sum_{i=1}^{n}\left|\mathbf{x}_i-\frac{1}{s}\mathbf{R}^{-1}\mathbf{y}_i+t\right|^2 \tag{4.16}$$

as well as

$$\sum_{i=1}^{n}\left|\mathbf{R}^{-1}\mathbf{y}_i\right|=\sum_{i=1}^{n}\left|\mathbf{y}_i\right|. \tag{4.17}$$

In the same way, the first term when we decompose Eq. (4.14) could be obtained in the similar way

$$X-\frac{2}{s}D+\frac{1}{s^2}Y=\left(\frac{1}{s}\sqrt{Y}-\frac{D}{\sqrt{Y}}\right)^2+\left(X-\frac{D^2}{Y}\right) \tag{4.18}$$

and

$$s=\frac{Y}{D}. \tag{4.19}$$

The simultaneous function of Eq. (4.15) and Eq. (4.19), scale factor can be solved as

$$s=\sqrt{\frac{Y}{X}}=\left(\frac{\sum_{i=1}^{n}\left|y_i\right|}{\sum_{i=1}^{n}\left|x_i\right|}\right)^{\frac{1}{2}}. \tag{4.20}$$

From this formula we get a conclusion that the determination of the rotation is not affected by the scale factor. It can be simply calculated as: firstly, get the sum of the length of the radius to the centroid both the fixed points set and the moving points set; then extract the square root of the proportion.

4.4 ALIGNMENT EXPERIMENTS

4.4.1 SIMILARITY CRITERIA

Due to the intense variety of organ shapes, seeking for corresponding points between the surfaces seems to be a difficult task and, the evaluation of alignment methods seems unrealizable. There is ever lack of reliable measures to quantify model quality yet. In this study, the selection of the label points depending on the anatomical structure drew an easy way of implement. There are two steps: the position matching that reconciling the

center of models and regular the size of the samples by mean radius of the whole vertices. Then we choose 20 points, we call them label points, on the polygonal surface. Evaluate the results by measure the Euclidean distances sum of corresponding points.

4.4.2 AVAILABILITY EXPERIMENTS

The availability experiments were used to check out the recovery capability and accuracy when the model has been rotated randomly. The triangular surface model of left lobe of lung field included 47022 vertices and 94040 faces. We compared the Euclidean distance sum of corresponding vertices with time, i.e. rotated the model with an offset from the original modality, and then recovered its posture using alignment algorithm. The results of distance sum of the corresponding marked points are recorded below. Tab. 4.1 records the results aligned using the method of section 4.3.3 as well as Tab. 4.2 is the results referring to method of section 4.3.4. In the table, the "rotation offsets" volume represents the rotation around the *x*, *y* and *z* axis in 3-D Cartesian coordinate respectively. The pre-alignment is the original sum of the distances between coordinating points before alignment and the post-alignment corresponds the distances after alignment. Improved rate denotes the variation of the distance sum, which is defined as

$$\varepsilon = \frac{\sum |l_p| - \sum |l_a|}{\sum |l_p|}. \tag{4.21}$$

l_p measures the sum of the distances of the corresponding vertices before alignment. l_a represents the sum of distances after alignment.

Table 4.1 Availability experiment results using the method of section 4.3.3.

Case	***Rotation offsets* (radian)**	***Pre-registration***	***Post-registration***	***Improved rate* (%)**
1	0, 0, 0.0175	0.0381	0.0346	9.2
2	0, 0.0175, 0	0.1956	0.0191	90.2
3	0.0175, 0, 0	0.0810	0.0799	0.1
4	0.0349, 0.0349, 0	0.4380	0.4424	-1.0

Table 4.2 Availability experiment results using the method of section 4.3.4.

Case	***Rotation offsets* (radian)**	***Pre-registration***	***Post-registration***	***Improved rate* (%)**
1	0.201, 0.251, 0.113	0.8317	0.6682	19.7
2	0.276, -0.295, 0.113	0.8658	0.3858	55.4
3	0.094, -0.126, -0.226	0.5307	0.4082	23.1
4	-0.308, 0.207, -0.069	0.9800	0.7523	23.2
5	-0.138, 0.258, 0.295	0.8272	0.7401	10.5

4.4.3 CONVERGENCE EXPERIMENTS

In section 4.3.4, we applied an iterative algorithm (Algorithm 4) to search the best alignment solution. The convergence experiments are utilized to verify the relationship between accuracy and optimization time. This procedure is similar as the availability experiments. Set the rotation offset to (0.245, 0.258, 0.138) previously, and watch the recovery results at intervals. Here we plot the variation of the sum of Euclidean distances with the iterative times, as the Fig 4.9. The abscissa shows the iterative times. The ordinate axis indicates the rate of change of distance measurements.

4.4.4 FITNESS EXPERIMENT RESULTS

Alignment experiments were performed on training samples of left lung field and liver field. To evaluate the results of alignment, we compared the Euclidean distances sum of corresponding label points between training samples and reference model. The improvement of distances sum of the label points is applied to evaluate the availability of proposed method. 4 cases triangular polygonal surface samples of left lung field and 3 cases on liver were implied. The rotation column records the angle adjustment, discussed in section 4.3.4. As well as the improvement rate is shown in Tab. 4.3 and Tab. 4.4. The pre-Alignment is the original mean distances of label points. The post-Alignment is the corresponding distances after alignment.

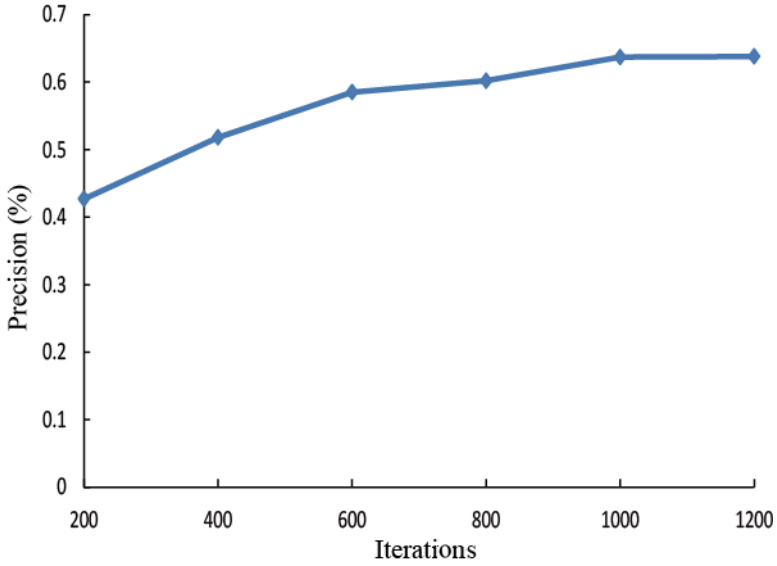

Figure 4.9 Variation of alignment results with iterations.

Table 4.3 Fitness experiment results of left lung models.

Case	***Rotation offsets* (radian)**	***Pre-registration***	***Post-registration***	***Improved rate* (%)**
1	0.0291	0.3214	0.3090	3.9%
2	0.0707	0.3395	0.3381	0.4%
3	0.0356	0.2503	0.2481	0.9%
4	0.0551	0.3340	0.3342	0%

Table 4.4 Fitness experiments results of liver models.

Case	***Rotation offsets* (radian)**	***Pre-registration***	***Post-registration***	***Improved rate* (%)**
1	0.0385	0.3565	0.3543	0.6%
2	0.0405	0.6078	0.6012	1.1%
3	-0.0012	0.4422	0.4467	-1.0%
4	0.0385	0.3565	0.3543	0.6%

4.4.5 DISCUSSION

From Tab. 4.1 and Tab. 4.2 we can see the proposed method is an available method for solve the rotation transformation in rigid registration. The mean improve rate is 24.63[%] using method of section 4.3.2 and 26.38[%] using method of section 4.3.4 respectively. The results of former appeared unstable. As well, the recovery results using both of the proposed methods seem relating to biased orientation. Since the proposed method bases on the projection of surface, the different orientations in 3-D space will produce the differences of projections. The original objects should not have lots of symmetric structures on surface patches, because this is a global matching method. But be benefit this global character, it also not sensitive for the noise.

Fig. 4.9 demonstrates the convergence with the iterative times increasing. From it we can see that in some sections of iterative times the optimized results are not changed, like the section from 500 to 700, as the randomness of the random rotation optimizer. In practice if we increase the iterative times up to 3000, the algorithm will exert instability. The errors will increase, especially when the oriental deviate of the training sample has been set as large shift. So, the robustness of this method should be enhanced and we should apply an analytic algorithm instead of random rotation optimizer.

The mean improvements of fitness experiments were 13[%] for lung models and 23[%] for liver models. In medical imaging human expert knowledge is often used as a substitute for a gold standard, since ground truth is only known for synthetic and phantom data, but not for the actual images. In the evaluation of alignment methods this becomes even more evident, because the goal is not clearly defined.

4.5 CONCLUSIONS

Aligning surface models into a common reference frame is a fundamental task in shape building. In this chapter, we propose a feature based method to transform the 3-D object alignment problem into 2-D spherical domain. Here, we introduced the piecewise Gauss map theoretical foundation and gave an approximated solution for triangular polygonal surface. As well, we proposed using representative points to reflect the modality of the point sets on Gauss map. While the K-means based clustering method was employed to obtain these representative points. In addition, to overcome the limitation of planar mapping, we introduce stereographic projection method to re-map the surface norms to a complex plane. In this way, freedom of object could be expanded.

The experimental results on the left lung and liver training samples showed the availability of the proposed method. This time we applied rotating Gauss sphere randomly to obtain the optical solution. However, it is common that it is hard to guarantee the convergence and convergent time is very long. So, as the future works, we would like to perform the iterative procedure using analytical method, as to solve the 2-D registration problem. Other else, in theory, Orientation discrimination using Gauss map is not elaborate yet. Surface Gauss map cannot describe the character of surface reliably all the time. So to analyze the convergence of it will give rise to an interesting study.

CHAPTER 5: CORESPONDENCE OF 3-D MODELS

The correspondence of 3-D surface models could be considered as a process that searches the same anatomical parts on surface of objects. In general, establishing the best defined correspondences is a fundamental as well as the most challenging part to construct the 3-D model. It is one of the major factors influencing model quality. Even in 2-D shape model building, manual corresponding trend to become unpopular. It is also a very time-consuming process, prone to error, and cannot be guaranteed to produce good models which limits their use in interpreting medical images. A semiautomatic or automatic approach to establishing correspondence is desirable. In this section, we concentrate on a parameterization based correspondence method. To form a total concept, we introduce basic theories of surface mapping, as well as the implement algorithms for zero genus triangular surfaces.

5.1 STATE OF THE ART

While correspondence methods for 2-D models have been wide-spread since the early 1990s, their development in medical imaging for 3-D models appeared only late than 2000s. Depending on the registration process involved, T. Heimann and H.P. Meinzer summarized the 3-D correspondence methods into 4 types: mesh-to-mesh registration, mesh-to-volume registration, volume-to-volume registration and parameterization-to-parameterization registration [116]. Since the correspondence of 3-D training samples could be treated as a searching process on surface of objects, a surface parameterization method could simplify this task significantly.

The purpose of parameterization of a surface is re-presenting the surface and remaining only the necessary topological information. For the correspondence problem, what we need include such as relative orders of landmarks, surface curvature and so on. Surface

parameterization is a one-to-one bijective mapping between the surface and an appropriate base domain. It has been applied in various fields of science and engineering, and many different methods have been proposed in the literature. As far as the surface corresponding, Kelemen *et al*. [117] proposed to implicit method using the Spherical Harmonics (SPHARM) mapping to correspond the training set. By aligning the first order ellipsoid, the shapes are seemed as the phase alignment. While referring to the details of the surface, these methods appear that could not attain a high quality, and the results depend strongly on the input shapes. Another implicit method is that start with a standard parameterized process and modify it for a better matching subsequently – a technique also known as re-parameterization or warping. In general, higher order correspondences must be enforced between specific anatomical points, curved landmarks, or sub-regions lying within the two surfaces. An explicit strategy is that, firstly mark the landmarks to the corresponding positions according to a reference model, and then implement the local regulation using the population based optimization. It is a potential way to attain the high quality mesh in some sense [118, 119]. The last but not the least, if the models including the features information, such as curvature or shape context, correspondence between these features can then be established using a generic numerical optimization algorithm [120]. Tree-based searching methods describe discrete optimization problems of branch-and-bound or priority search [121]. During the tree expansion, each node represents a partial solution. A full solution is found by following the path from the root of the tree to one of its leaves. And the correspondence is mainly represented as collections of assignments between pairs of feature points, and the expansion step involves adding a new pairwise assignment to a given solution.

In this chapter, we propose a distance map based correspondence method. It uses a mapping procedure that assigns an initial manual point set to the other point sets. It is semiautomatic that the landmarks have been placed on a reference surface model previously. As another experiment, we use distance maps as a basis for establishing automatic correspondence.

5.2 DIFFERENTIAL GEOMETRIC PROPERTIES OF SURFACES

5.2.1 BASIC THEORIES OF DIFFERENTIAL GEOMETRY

In the 3-D case a surface normal to a surface at a point *P* is a vector that is perpendicular to the tangent plane to that surface at *P*. The concept has been generalized to differential geometry of surface. Suppose a map from a planar domain R^2: (u,v) to 3-D domain R^3: (*x*, *y*, *z*), a regular surface patch $\mathbf{r}(u,v) = (x(u,v), y(u,v), z(u,v))$. And the partial derivative vectors $\mathbf{r}_u = \left(\frac{\partial x}{\partial u}, \frac{\partial y}{\partial u}, \frac{\partial z}{\partial u}\right)$ and $\mathbf{r}_v = \left(\frac{\partial x}{\partial v}, \frac{\partial y}{\partial v}, \frac{\partial z}{\partial v}\right)$ are linearly independent, i.e. $\mathbf{r}_u \wedge \mathbf{r}_v \neq 0$. *Normal* of the surface is defined as

$$\mathbf{n}(u,v) = \frac{\mathbf{r}_u \wedge \mathbf{r}_v}{|\mathbf{r}_u \wedge \mathbf{r}_v|}. \tag{5.1}$$

And a *Gauss map***,** introduced in the previous chapter, maps a point on the surface to its normal vector on the unit sphere. Denote the first fundamental, which defines the lengths on the surface as well as the second fundamental forms, which defines how the surface is embedded in the Euclidean space as

$$\begin{aligned} F_1 &= Edu^2 + 2Fdudv + Gdv^2 \\ F_2 &= Ldu^2 + 2Mdudv + Ndv^2 \end{aligned} \tag{5.2}$$

or the matrix notation $F_1 = \begin{pmatrix} E & F \\ F & G \end{pmatrix}$ and $F_2 = \begin{pmatrix} L & M \\ M & N \end{pmatrix}$.

Then the principal curvatures k_1, k_2 are the eigenvalues of $F_1^{-1}F_2$ .The *Gaussian curvature K* could be calculated by

$$K = k_1 k_2 = \frac{LN - M^2}{EG - F^2}. \tag{5.3}$$

As well the *mean curvature H* is defined as the sum of the eigenvalues

$$H = \frac{1}{2}(k_1 + k_2) = \frac{1}{2}\frac{LG - 2MF + NE}{EG - F^2}. \tag{5.4}$$

5.2.2 SURFACE MAPPING AND TRIANGULAR SURFACE

Surface parameterization can be seemed as map one surface to another surface since the parameter domain itself could be represented as a surface, such as planar domain, unit sphere and so on [123]. According to the difference of constrains, surface mapping methods can be distinguished to 3 type. *Isotropic mapping* from *S* to *S`* is isometric or length-preserving if the length of any arc on *S`* is the same as the length of corresponding arc on *S*. Isometric surfaces have the same Gaussian curvature at corresponding pairs. *Conformal mapping* or angle-preserving if the angle of intersection of every pair of intersecting arcs on *S`* is the same as that of the corresponding angle on *S* at the corresponding point. The stereographic mapping interpreted in section 4.3.4.1 is this type. *Equiareal mapping* is defined as if every part of *S* is mapped onto a part of *S`* with the same area. Isometric mapping is ideal that it has been proofed that every isometric mapping is conformal and Equiareal, i.e. it preserve lengths, angles, areas on both of surfaces. However, it is difficult to realize in most cases. *Harmonic mapping* is defined as a mapping *f* satisfies the Cauchy-Riemann equations: two surfaces functions: $z = x + iy$ and $\omega = u + iv$. Any mapping ($u(x, y)$, $v(x, y)$) which satisfies

$$\Delta u = 0\,,\ \Delta v = 0 \tag{5.5}$$

where Δ is the Laplace operator

$$\Delta = \frac{\partial^2}{\partial x^2} + \frac{\partial^2}{\partial y^2}. \tag{5.6}$$

Harmonic map has many nice properties. Isometric is also harmonic mapping, such that each of the functions u and v is the solution to a linear elliptic partial differential equation (PDE) which can be approximated by various methods.

Nowadays, surfaces are frequently represented using triangular polygonal mesh. So the discrete mapping methods have become the research focus in many fields. The popularity of triangular meshes can be explained in terms of both theory and practice. In theory, any surface can be triangulated. Differential forms, curvatures, geodesics, and conformal mappings can only be solved on meshes by approximation.

A half-edge data structure is commonly used in geometric software to represent triangular meshes. It is flexibility and high performance to support discrete geometric processing operations and has been established as a static representation and dynamic handling of arbitrary polygonal meshes [124]. A mesh M consists of a list of vertices $\{V_i\}$, edges $\{E_i\}$, and faces $\{F_i\}$. Each edge represents by two ordered half-edge $h_{ij} = [V_i, V_j]$ and $h_{ji} = [V_j, V_i]$, which points from the source vertex to the target vertex. If there is unique existence of the orientation of vertices $\{v_i,v_j,v_k\}$ in each face, we call M is orientable (see Fig. 5.1).

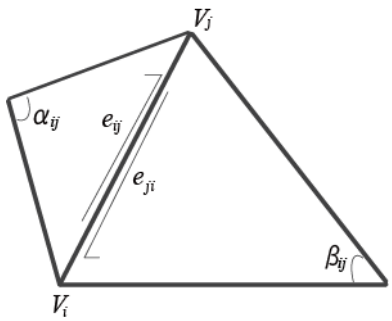

Figure 5.1 Half edge structure. Edge V_iV_j is represented by two half-edge e_{ij} and e_{ji}.

5.2.3 SPHERICAL CONFORMAL MAPPING

One kind of conformal mapping that maps a genus zero surface to a unit sphere is called spherical conformal mapping. An important theorem given by Gu and Yau is that harmonic maps from a closed genus zero surface to the unit sphere are conformal [125]. For a triangular surface, suppose K is a simplicial complex, u, v denote the vertices, and e_{uv} denotes the edge spanned by u, v. A position vector $r(u, v)$ on surface of 3-D space is usually represented by

$$r(u,v) = (x(u,v), y(u,v), z(u,v)).$$

We use f to represent the piecewise linear function defined on K. The string energy is defined as

$$E(f) = \sum_{e_{uv} \in K} k_{uv} \left\| f(u) - f(v) \right\|^2 . \tag{5.7}$$

The string constants k_{uv} describes the stretching factor between the surface and the parameter domain. Changing it we can define different string energies. If $k_{uv} \equiv 1$, the string energy is called the Tuette energy. Well, string constants that define the harmonic energy are calculated by

$$k_{uv} = \frac{1}{2}(\cot \alpha_{ij} + \cot \beta_{ij}) \quad \alpha_{ij} + \beta_{ij} < \pi \tag{5.8}$$

where α_{ij} and β_{ij} are the two angles opposite to the edge in the triangles sharing the edge on original triangular surface. Many different methods to deal with genus zero surfaces have been proposed in the literature, such as the harmonic energy minimization, global conformal parameterization, and Laplace-Beltrami operator and so on. With respect to the spherical conformal mapping, it has been proved that the harmonic maps from closed genus zero surfaces to the unit sphere are conformal. We can map the polygonal surface to a unit surface firstly and minimize the error sum of harmonic energy between the two

surfaces. However the construction of spherical conformal mapping by this method is not unique. There are essentially 6 degrees of freedom in a spherical conformal mapping and the maps form a Möbius group [125].

5.2.4 CONSTRAINT THE TRANSFORMATIONS

A Möbius transformation is a map defined on complex plane *C*,

$$M(z)=\frac{az+b}{cz+d},\quad a,b,c,d\in C \text{ and } ad-bc=1. \tag{5.9}$$

The Möbius transformations are conformal as well. All Möbius transformations form the Möbius group. The different constraints of Möbius transformations will lead to different mapping results. Fig. 5.2 shows 2 cases of examples that mapping the same lung sample using spherical conformal mapping, but with different constrain condition of Möbius transformations. The left one uses the zero mass-center constraint proposed in [123]. As well, the variation of shapes could be constrained as the unique mode according to the fixed three datum points on surface too. Given three distinct points z_1, z_2, $z_3 \in C$, the Möbius transformation which maps them to $\{0, 1, \infty\}$ respectively is

$$M(z)=\frac{(z-z_1)(z_2-z_3)}{(z-z_3)(z_2-z_1)}. \tag{5.10}$$

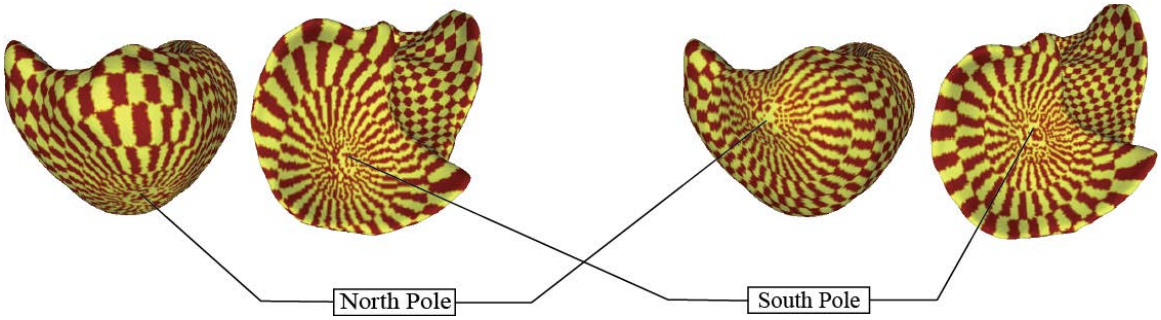

Figure 5.2 Map the same lung sample with the different constraint conditions of the Möbius transformation. Left images: using zero mass-center constraint. Right ones: using three special points surface fixed constraint.

5.2.5 STEEPEST DESCENDENT ALGORITHM

This section follows the Gu-Yau algorithm for genus zero meshes. Given a genus zero mesh *M*, For a map $f: M \to R^3$, $f = (f_0, f_1, f_2)$. The piecewise Laplacian is

$$\Delta_{PL} \vec{f} = (\Delta_{PL} f_0, \Delta_{PL} f_1, \Delta_{PL} f_2) \quad . \tag{5.11}$$

If a map *f* is harmonic, the tangential component of the $(\Delta_{PL} \vec{f})^{\perp}$ is zero. A novel steepest descent algorithm is proposed to minimized the string energy $E(f)$. The absolute derivative of tangent vector in step δt is calculated by

$$\delta \vec{f}(v) = -(\Delta_{PL}(\vec{f}) - (\Delta_{PL} \vec{f})^{\perp}) \times \delta t \quad . \tag{5.12}$$

In experiments, we should choose δt modestly. If it is too large, the result would not converge to an acceptable accuracy. The Tuette mapping is not able to unfold sufficiently. And the smaller value would result in amount of time even stop in halfway. Here we proposed variable values of δt to confirm the convergence efficiently. The algorithm using spherical conformal mapping with 3-datum points' constraint and with zero-mass constraint are listed below orderly.

Algorithm 3:

Input (mesh *M*, initial length δ_t, energy error threshold δE ,select three datum points P_0, P_1, P_{init} in surface vertices)

1) *Output ($\vec{h}: M \to R^2$), where $\vec{h}$ is the mapping.*
2) *Compute Gauss map N: $M \to S^2$. Let t = N.*
3) *For each vertex $v \in M$, compute absolute derivative Dt(v) and update $\delta \vec{f}(v)$ as Eq.* (5.12).
4) *Compute the hormonic energy E.*
5) *Compute conformal embedding $\vec{h}$ and its energy E_0.*
6) *$\delta E = E - E_0$.* If *$\delta E < 0$, $\delta t = \delta t * k$, $k \in (0, 1)$. Else if $\delta E <$ threshold, stop. Else assign E to E_0, repeatsteps 2) through 6).*
7) *Compute stereographic projection. Denote the corresponding complex points of three datum points as z_1, z_2, z_3* as (4.2).
8) *Compute Möbius transformation as* (5.10).

Algorithm 4:

Input (mesh *M*, initial length δ_t, energy error threshold δE ,select three datum points P_0, P_1, P_{init} in surface vertices)

1)-3) are same as **Algorithm 3**.

4) *Compute Möbius transformation* $\vec{\varphi}_0$

$$\Gamma(\vec{\varphi}) = \int_{M_1} \vec{\varphi} \circ \vec{h} d\sigma_{M_1}$$

$$\vec{\varphi}_0 = \min \left\| \Gamma(\vec{\varphi}) \right\|^2$$

where $d\sigma_{M_1}$ is the area element on M_1. $\Gamma(\vec{\varphi})$ is the mass center, and $\vec{\varphi}$ minimizes the norm in the mass center condition.

5) *Compute the hormonic energy E.*

6) *Compute conformal embedding* $\vec{h}$ *and its energy* E_0.

7) $\delta E = E - E_0$. If $\delta E < 0$, $\delta t = \delta t * k$, $k \in (0, 1)$. *Else if* $\delta E <$ *threshold, stop. Else assign E to* E_0*, repeatsteps 2) through 6).*

5.3 CORRESPONDENCE METHODS

5.3.1 DIRECT CORRESPONDENCE METHOD

In this section, a parameterization based correspondence method is proposed to build a static model of organic training sets. The procedure is demonstrated in Fig.5.3. “mapping” means mapping the surface to parameterization domain and “placing” indicates the order of the procedure of the landmarks placement. The scheme is described as follow. Firstly, choose one model as reference model, and place the landmarks onto the surface manually to anatomical significance. Like the description in section 5.3.1. Then map the reference model and other surface models into a common parameterization domain using spherical conformal mappings. According to the properties of conformal mapping, the relationship between the landmarks is prevented. Then search the corresponding points through the all spherical maps on the base of spherical coordinates. Since the points on surface and the corresponding points on its map are one-to-one, we could find the positions of landmarks for all the surface models.

5.3.2 AUTOMATIC PLACEMENT OF LANDMARKS

Although using the method of section of 5.3.1, we just need manually landmarking one

sample model for each object. Manual landmarking are still time-consuming as well as subjective. A fully automatic approach to establishing correspondence is anticipant. One of the simple automatic approach, which has been widely applied in object recognition from video images, is placing the given number of landmarks by equal space on each boundary or surface. In this section, we develop this method to 3-D space.

While considering for a 2-D shape, the nature order of point index could be mapped to a parameter space by linear operation. A correspondence procedure can be described that select a starting point on each training sample and equally space an equal number of points on each boundary. In the similar way, simple shapes in 3-dimension might have the topology of a sphere, where the parameter space is then the appropriate topological primitive, a sphere. Following the description of mapping procedure in previous section, the positions of landmarks are angle-prevented and the mapping is one-to-one from the shape space to parameter space. As the illumination of Fig. 5.4, at first, we establish a uniform triangular sphere of which the length of edges is equal. As well the number of vertices of reference sphere equals the number of landmarks we wanted. Then map this reference sphere to spherical conformal maps of surfaces. The mapped points on spherical maps are also isometric. In this way, we can obtain a set of landmarks which are assumed to be placed by the same phase of surfaces.

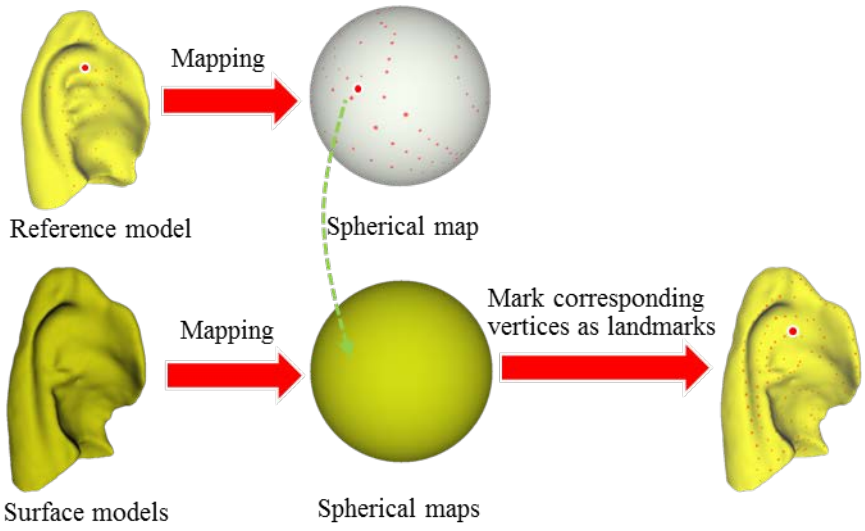

Figure 5.3 Correspondence method using a preliminarily placed reference model. At first landmarks are placed onto the Reference model manually. Then map all the models to a same parameterization domain. Mark the landmarks to the corresponding positions according the spherical coordinates. The landmark points are represented as small dots.

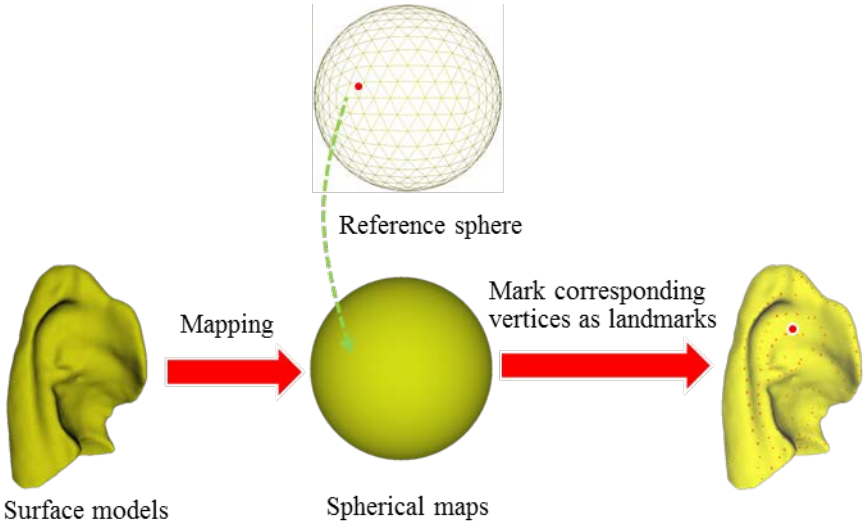

Figure 5.4 Automatic correspondence method using an equal spaced reference sphere. Here we replace the reference sphere for equilateral polygon.

5.4 CORRESPONDENCE EXPERIMENTS

5.4.1 SIMILARITY CRITERIA

Since there is not standard of agreement on correspondence or a mathematical definition, the measures of correspondence are quite difficult. In this experiment we tested two criteria. The first goodness measure is directly computed on the corresponding points as differences to manually selected anatomical landmarks. The second one is of indirect nature, since they are computed using the PCA model based on the correspondence.

Goodness: is directly computed on the corresponding points as differences to manually selected anatomical landmarks. Generally, to the reference surface model, the landmarks have been placed to anatomical significance. Based on the anatomical features of landmarks on reference model, we can choose the corresponding points on other surface models. Calculate the Euclidean distance sum between the chosen positions and the corresponded positions. Normalize it and make the result as the goodness measure.

Compactness: the ability to use a minimal set of parameters. We can approximate how few of principal modes are able to represent the variation of shapes. It simply measures the accumulative variance of the model.

$$C(M) = \sum_{i=1}^{M} \lambda_i \tag{5.13}$$

where λ_i is the i_{th} eigenvalue. $C(M)$ is measured as a function of the number of shape parameters M. In order to reason about the significance of differences, its standard error is determined from training set size n_s:

$$\sigma_{C(M)} = \sum_{i=1}^{M} \sqrt{2 / n_s}\,\lambda_i \tag{5.14}$$

5.4.2 Comparative Analysis of Different Constrains of Spherical Conformal Mapping

We compared the corresponding results with two constraint conditions of spherical conformal mapping described in section 5.2.4. We applied our proposed correspondence method on 15 cases of aligned left lung training samples. The goodness ability for each evaluation was calculated. The objective measure evaluations define distances between shapes with the aid of a finite set of shape points. These points had been placed on the surface manually. Test the errors between the automatic corresponding results to the expected locations where the radiologists chose. Fig.5.5 denotes the mean errors between the real locations of landmarks to their expected locations. Sub-graph (a) is the results when the spherical conformal mapping is performed using 3-datum points' constraint. Sub-graph (b) is the results when the constraint applied zero mass-center constraint.

5.4.3 Automatic Correspondence Experiments

This section describes automatic correspondence results using the method of section 5.3.1. We performed 3 type of organic models generation: left lobes of lung regions from 11 cases of chest CT images, 11 cases of liver model, and 5 cases of cardiac model. The average numbers of vertices are left lung model---62000, liver model---37000 and cardiac model---24000 separately. Each model was constructed by 642 landmarks. The mean model demonstrates in Fig. 5.6. The whole cases of correspondence results are attached in Appendix B. The algorithm took a long time to converge; for example, using a C++ implementation on a desktop PC (Intel(R) Core(TM) i7—3.4 GHz, 8G RAM), the left lung experiment took 55 min/case, the liver experiment took average 15min/case, and the cardiac took 4 min/case.

For a qualitative inspection of correspondence, we tested the compactness ability of model described in section 5.4.1. We can see the variation becomes small with the number of parameters increasing. Graph of compactness results is shown in Fig. 5.7.

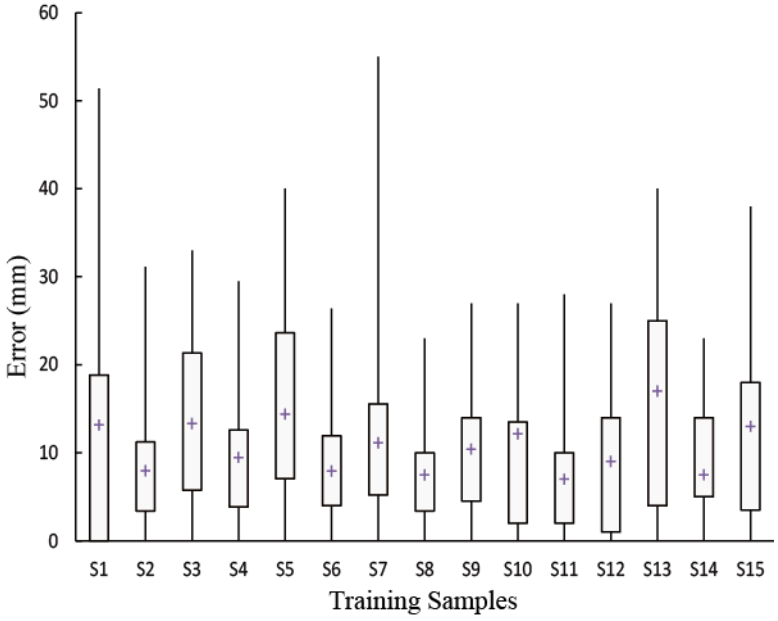

(a)

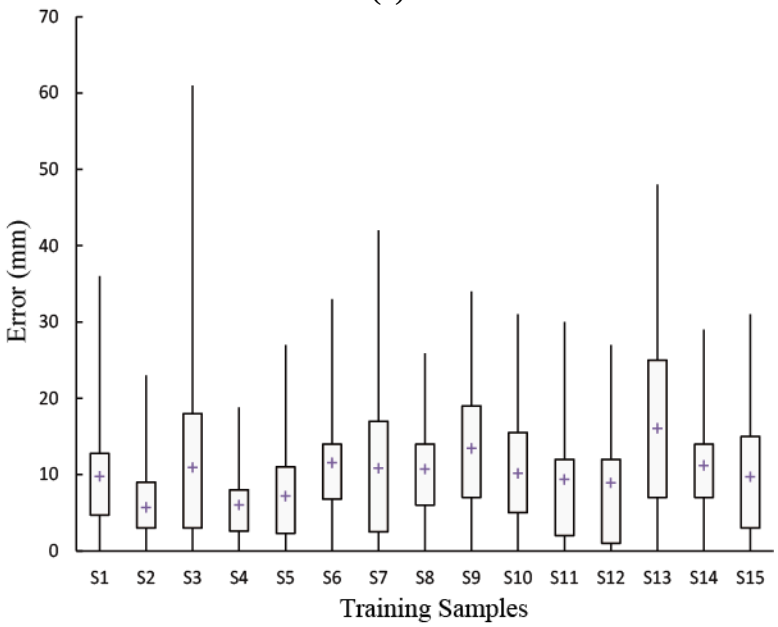

(b)

Figure 5.5 Results of goodness evaluation. (a) Errors of corresponding results using the spherical conformal mapping method with 3-datum points' constraint. (b) Errors of corresponding results using same mapping method with zero mass-center constraint.

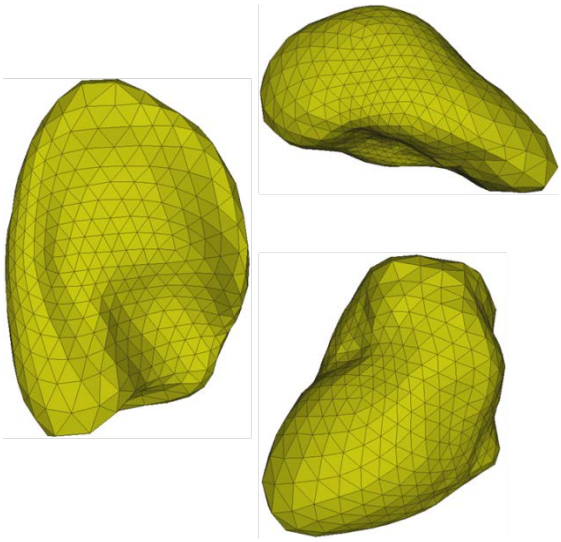

Figure 5.6 Mean shape models of left lobe of lung, liver and cardiac.

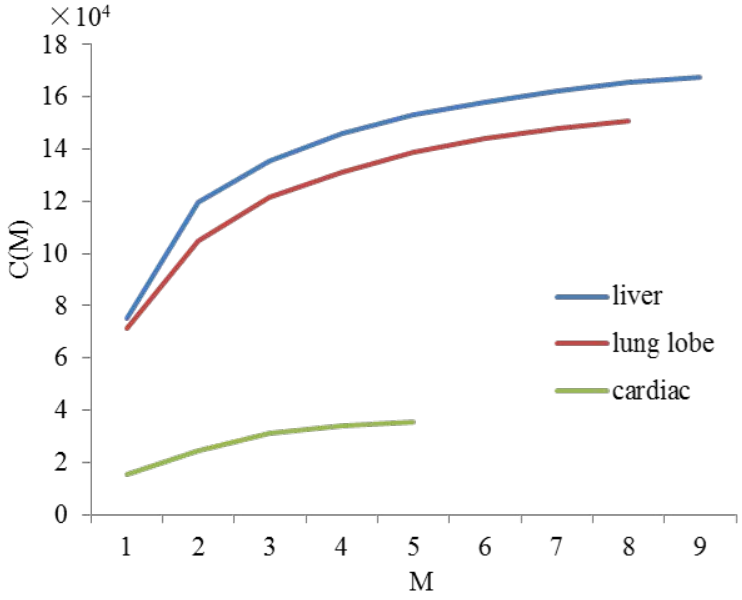

Figure 5.7 Graphs of compactness ($C(M)$).

5.4.4 DISCUSSION

From Fig. 5.5, the mean error of corresponding results with the 3 datum points' constraint was 10.83[mm], and the mean error with zero mass-center constraint was

10.09[mm]. Comparing to the size of left lung model, we think that there is nearly indistinctive when using spherical conformal mapping with 3-datum points' constraint, and with zero mass-center constraint. The most variation from the expected positions was observed at the bottom of the lung, since the intense variety caused by respiration. However, according to the standard deviations of the box plot, the correspondence results with zero mass-center constraint were more concentrative. That is the reason we use this constraint for the following experiments.

In automatic correspondence experiment, we described the practices of automatic model generation to automatically construct 3-D statistical shape models. Compared to other research reports [126], our proposed method took shorter processing time. The processing time related to the number of vertices of surface models, though the mapping complexity of algorithm is $O(mn)$, where m is the number of the vertices of model, n is the number of required iterations.

We also performed the experiment of compactness ability for automatic correspondence experiment. In Fig. 5.7, the line of left lung results and the liver result display slope forms. We think that the main variation of shapes concentrate on the limited forms. Therefore, it is possible to use a few vectors of shape to appropriate the deformation. However, as to the graph of cardiac results, we see that the trend of the line growing is gradual. So it is difficult to reduce the shape vectors to too few. In this study, we restricted to the case of linear models where the distribution on shape space is represented as a single multivariate Gaussian. But as stated in section 3.4.5, due to the motion of cardiac, the linear condition has been broken.

In this study, we applied the equal-spaced correspondence method. But some authors have pointed out a matter of fact that the relative position of equivalent points may vary considerably over the training set. That might lead poor models. The figure below demonstrates two correspondence results of left lung. The left one is utilizing the semi-

automatic method described in section 5.3.1. And right one is generated by method of section 5.3.2. Institutively, the placed landmarks in the first one seemed more reasonable.

To develop evaluation methods for model correspondence is also meaningful. In [127], the authors proposed the use of three different measures. Beside the compactness criterion, the other including: 1) *Generalization*: the ability to measure the capability to represent unseen instances of the class of object model, i.e. given an unseen instance, and approach its shape using the generated model, we measure how much degree of fitted parts. Generally this ability of each model is measured using leave-one-out reconstruction. 2) *Specificity*: the ability to represent only valid instances of the object. Relative to the generalization ability, a good model should only generate instances of the object class that are similar to those in the training set. Minimal model specificity is important in cases when newly generated objects need to be correct. Rather than rules-of-thumb measurement, according to the utility of a model in a particular application, the authors instead aim to measure properties that a good shape model should have. See Appendix B.

5.5 CONCLUSIONS

A key step in model building involves establishing correspondence of each landmark between shape boundaries over a reasonably large set of training images. In this chapter, we proposed two methods to correspond the triangular surface samples. As the next step, we will research how to embed this statistical shape model into volume image data and perform the searching algorithm.

Reviewing the model building, different choices of correspondence give models of varying quality. To obtain a “good” model, the model-building framework described requires a parameterized transformation model for manipulating correspondence. As noted earlier, many researchers have reported interesting results in this area. A promising method is proposed in [126,127]. They assume that “quality” of a model could be measured with a single suitable objective function. They used the MDL principle to generate an objective function for model parameter selection. Styner *et al*. [127] have compared models built using various methods, including MDL and SPHARM. They used a number of different biomedical datasets, and concluded that for modeling purposes, MDL outperformed other approaches. So, as the future work of our study, we would like to apply optimization strategy to refine the correspondence.

CHAPTER 6: EXPERIMENTS OF ORGANIC SEGMENTATION

The developed various segmentation methods are evaluated on three clinical applications. To show the general applicability of the method, three different modalities were chosen for the tests: chest CT images that include lung and cardiac regions, abdominal CT images and MRI abdominal images in where we want to extract liver regions. All modalities deliver full 3-D volumes of various voxel resolutions. The lung regions are treated in section 6.1. Because the segmentation of lung regions is always as the basic of lesion recognition, we aim at preventing the completeness of lung regions as much as possible. The liver regions are examined in section 6.2. The dataset includes 4 cases of CT images and 6 cases of MRI images. The last considered interest object is the cardiac. Although the contrast of image density is significant, the adjacent boundaries with liver and the divided section from aorta also make it a challenging target to segment.

6.1 SEGMENTATION OF LUNG REGION

Because the lung region is independent and strong contrast with muscular issue in chest CT images, 3-D region growing methods with fixed image density have been applied for many years. But if the lung region includes lesions, of which the pixel values are larger than the values of round issues, using simplex region growing method may leave out the lesion regions. In this chapter, we propose a complementary region growing method to solve this problem.

6.1.1 DATA SET

The Lung Image Database Consortium (LIDC) has developed as lung nodule collection and reporting protocol. The LIDC/IDRI Database contains 1018 cases, and there are four radiologists to detect suspicious lesions independently. They are demanded to draw the outline around the suspicious lesions whose diameter from 3mm to 30mm

and rate diagnostic characteristics on an ordinal scale of 1-5. Both standard-dose diagnostic CT scans and lower-dose CT scans from lung cancer screening examinations are acceptable [128]. Hence, the representation of data is universal. Some examples of pulmonary nodules are demonstrated in Fig. 6.1.

6.1.2 PROCESSING

We carry out two times of region growing. At the first time, the seed points, from where region growing begins, are set inside of lung region. As a result, the outside region is removed, as Fig. 6.2(b) demonstrates. However, since the threshold of pixel value is set low, some issues in high pixel values such as vessels, bronchus as well as the nodules are remained. To fulfill these "holes", at the second time, seed points are placed at outside region. Scan for the continuous black region, and the VOI could be remained integrally (sub-graph (c)). The feasibility of proposed method has been proofed in section 4.2.1 using theory of set.

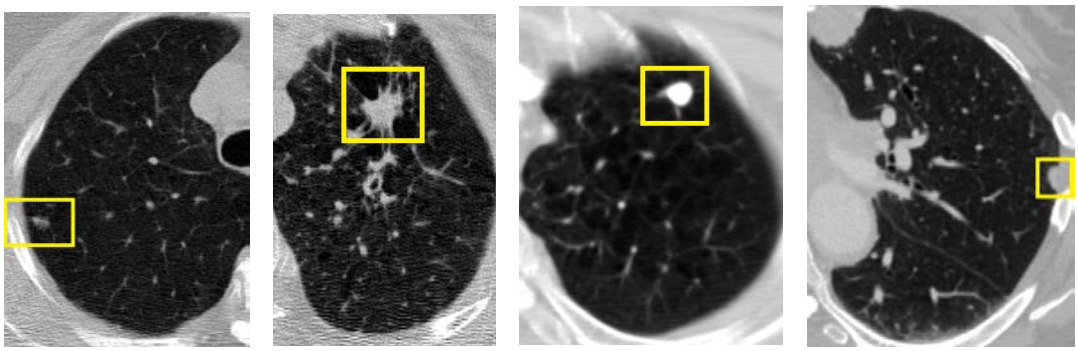

(a) (b) (c) (d)

Figure 6.1 Some nodule samples in LIDC database. Pixel value of (a) is -549.965, (b) is -143.188, (c) is 242.917, (d) is -89.57.

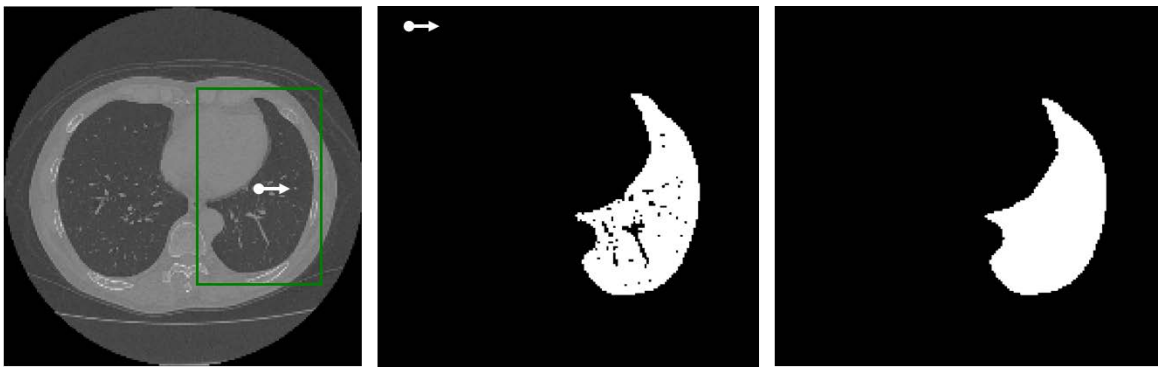

(a) (b) (c)

Figure 6.2 Generate fulfilled ROI of left lobe of lung using region growing algorithm. (a) Set the seed inside of the ROI and implement region growing to remove the background regions. (b) Then, set the seed outside the region and ran region growing again to fulfill the "holes" remained in step 1. (c) Final result.

6.1.3 RESULTS

Validation was employed with 10 sets of chest CT images to evaluate the final performance of segmentation. 3-D polygonal surface of segmented region are listed in Appendix C. Comparing to the gold standard data based on the ROC criterion stated in section 2.5.2, qualitative results of segmentation are recorded in Tab. 6.1. Average TPR is 0.985, and average FPR is 0.024. One case of comparison results using simplex 3-D region growing and our proposed method, we can see that the nodule region was prevented in the segmented image using the proposed method. On a standard PC (same performance in section 5.4.3), the processing time took about 20 seconds per case.

Table 6.1 Evaluation of left lung segmentation experiments.

Case	***TPR***	***FPR***	***Case***	***TPR***	***FPR***
1	0.997	0.240	6	0.973	0.005
2	0.998	0.534	7	0.984	0.019
3	0.957	0.040	8	0.996	0.021
4	0.995	0.023	9	0.950	0.002
5	0.997	0.026	10	0.998	0.021
Average (10 cases)		***TPR***: 0.985		***FPR***: 0.024	

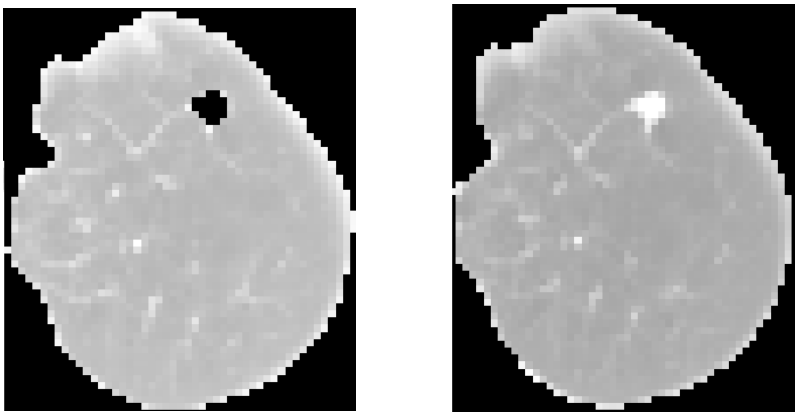

(a) (b)

Figure 6.3 One case of segmented result of lungs with nodule regions. (a) The result using simplex 3-D region growing method. (b) The result using proposed method.

6.1.4 DISCUSSION

From Tab. 6.1, the average TPR of our proposed method is 0.985. The main persistent missions include 3 locations. The first one is the main trachea, which connects to the left lungs and pixel values are similar with lung regions. It seems impossible to eliminate when image density information is used only. Consequently, we consider inducing multiple-scale technique to remove the trachea region. The second missed regions are located at the adjacent with cardiac. It is where the vena cava and portal vein connect to the lung regions. It is very difficult to define the boundary between lung regions and cardiac regions, even by a radiologist. As the improvement, we advise to extract cardiac regions previously before implement the lung regions segmentation. We can use boundary-based method with curvature information to extract the cardiac and keep the remained details which are the small vessel structures and generally are separated to the lung regions. The third over-segmented regions, although do not often happen, are the stomach regions. We have explained this limitation of 3-D region growing method in section 2.3.3. We think it is a good choose to use slice-by-slice region growing method as the substitution.

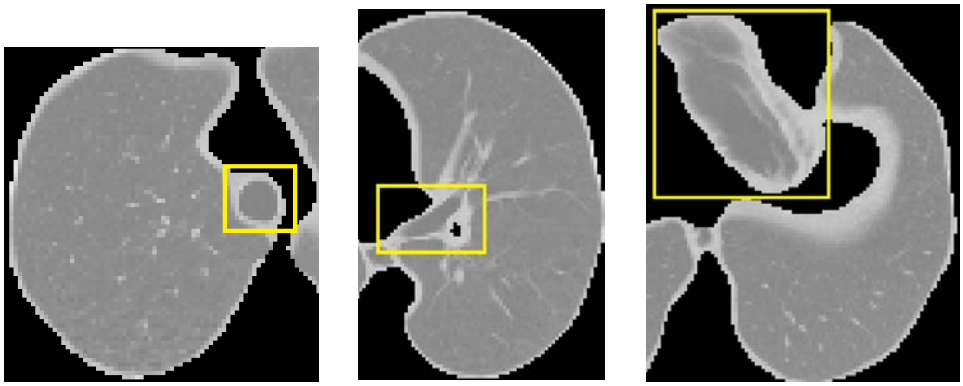

(a) (b) (c)

Figure 6.4 The over-extracted regions when segment the lung region. (a) The fenced region is trachea. (b) The parochial region inside of fence is cross section of aorta. Generally, it is divided to cardiac regions. (c) The fenced region is stomach. Sometimes it is segmented when using density-based methods.

The most interesting aspect lung regions segmentation was how to deal with a region with lesions. Although the accuracy result of the proposed method is not evident, from Fig. 6.3, the integrality of this method is confirmed. As well, the more challenging part for lung segmentation algorithms is to deal with the juxta-vascular type, which has significant connections to its neighboring vessels, as well as the juxta-pleural type nodules, which has some degree of attachment to its neighboring pleural wall, as Fig. 6.1(d) shows. An excellent research result has been reported by Shanhui Sun *et al*. [129]. They presented a segmentation approach of lung with high-density pathologies. It consists of two main processing steps. First, roughly segment the outline of the lungs using robust active shape model (RASM) matching method. And then, an optimal surface finding approach is utilized to further adapt the initial segmentation result.

6.2 EXPEREMENTS OF LIVER REGION SEGMENTATION

Main motivation to apply the developed algorithms to the liver is a project for surgery planning [130]. To calculate and visualize the optimal resection strategy for liver tumors, the liver tissue, vessel systems, and tumors have to be segmented beforehand. Performed manually, segmentation of the liver tissue takes 30 to 45 minutes and is the most time-

consuming section of the planning process. Therefore, an automated solution for this task would speed up the planning process considerably and make it available for a larger number of patients.

6.2.1 DATA SET

The used liver images were acquired on 4 cases from CT scanners and 6 cases from MRI. At the same time, the voxel spacing varies considerable: The in-plane spacing and slice thickness of CT images are 0.616[mm] and 2.0[mm] separately. As well the MRI images are 0.742[mm] and 4.0[mm] separately. All the images were contrast graphic. At the same time the MRI images are pathologic and include tumors, metastases and cysts of different sizes. The reference gold standards for evaluation were created manually by radiological experts, working slice-by-slice in transversal view. It was defined as the entire liver tissue including all internal structures such as vessel systems, tumors etc.

6.2.2 PROCESSING

Since contrast media was injected, the images of liver regions were conspicuous. However, because diffusion of the contrast media was asymmetrical, with the time passing the image density changed very quickly. In practice, segmentation using 3-D methods had produced a disastrous result. Growing region overflowed incidentally due to the image noises or neighbour issues of which the pixel values are similar. Consequently, we substituted for slice-by-slice region growing style.

The flow of the proposed method is described as: firstly, to smooth the data, anisotropic diffusion filtering was used as a preprocessing step for all image volumes. The filter was run over 3 iterations, using a time step of 0.0625 and a conductance of 1.0. Next we enhanced the VOI by selecting the arrangement of intensity window properly. The whole preprocessing is illuminated in Fig. 6.5. Regard to the settle of seed points, we place one at the beginning slice of liver regions. Then run 2-D region growing inner one slice. After that, calculate the mass center of the obtained region. Make it as the seed of growing region for the next slice, but the *z* direction should be added one.

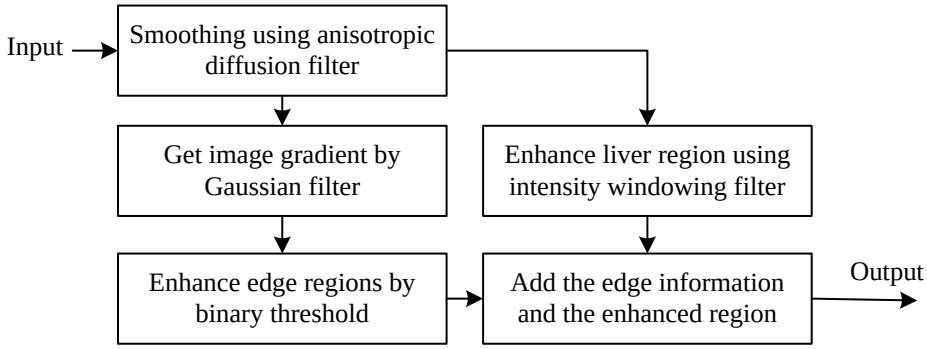

Figure 6.5 Flowchart of processing and the intermediate results.

6.2.3 RESULTS

The results are listed in Tab. 6.2. Data from case1-4 are abdominal CT images. Case5-10 are MRI images. Average TPR of segmentation results is 0.920 and average FPR is 0.003. The 3-D polygonal construction models of segmented liver regions are arranged in Appendix B.

To comparison of the proposed slice-by-slice region growing method, a standard 3-D region growing method was also performed. The experiment conditions were same. As the results, TPR 0.913 and FPR 0.04 were obtained.

Table 6.2 Evaluation of liver segmentation experiments.

Case	***TPR***	***FPR***	***Case***	***TPR***	***FPR***
1	0.964	0.001	6	0.600	0.0
2	1.0	0.002	7	0.835	0.0
3	0.993	0.0	8	0.827	0.001
4	0.993	0.001	9	0.868	0.008
5	1.0	0.013	10	0.825	0.001
Average (10 cases)		***TPR***: 0.920		***FPR***: 0.003	

6.2.4 DISCUSSION

In this experiment, although the contrast of intensity between liver regions and other issues is significant, however, influenced from the noises, the growing regions facilitate to over flow. In general, it is still very common to find medical image datasets that have been acquired with large inter-slice spacing that result the resolution of *z* axis is very low. Therefore, overflow along z axis is often and disastrous. The overflowed regions were mainly concentrated on the adjacent boundary with the cardiac, as the Fig. 6.6 demonstrates. As the outcome in Tab. 6.2 reveals, the employed algorithm is more robust, although we need to set more seed points manually. In practice, the preprocessing for MRI images needed much manual intervention. Since that in spite of the pixel value of contrasted liver regions were quite significant than the other issues, the variety of image density is distinguishable with contrast medium being absorbed. So we nearly have to adjust the parameters of intensity windowing filter case-by-case.

Comparing the results of 3-D region growing method, the improvement of accuracy by our method is obvious. Although this method needed manual intervention, segmentation time per case could be reduced to 5 minutes averagely.

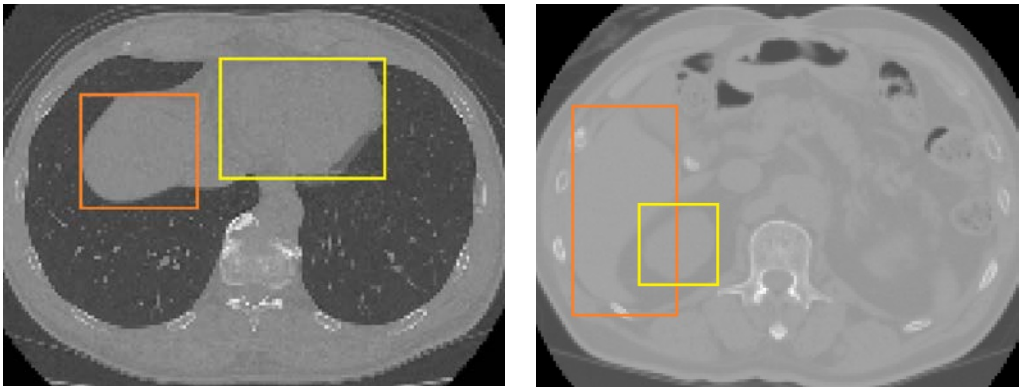

(a) (b)

Figure 6.6 Adjacent organs to liver. Region in orange box is the liver. (a) Region in yellow box is cardiac. (b) Region in yellow box is kidney.

Many studies involved model-based method for segmentation of liver regions [131]. Since the variation of the liver model makes the local search very susceptible, some researcher encourage to used multi-resolution strategy and a reasonable fit in the rougher resolutions. Reducing the candidate regions progressively is essential for a successful segmentation.

6.3 EXPERIMENTS OF CARDIAC REGION SEGMENTATION

Generally, we note that the cardiac region images are required from chest CT scan, with heart beating, most of time, the cardiac regions attach to the liver regions closely. As well the density of cardiac regions is in close proximity to the liver regions in the un-enhancement CT images. So we considered to concentrate an edge-based segmentation method. At the same time, to choose a suitable position to cut the arty and vein from cardiac is require object knowledge, as the figure below.

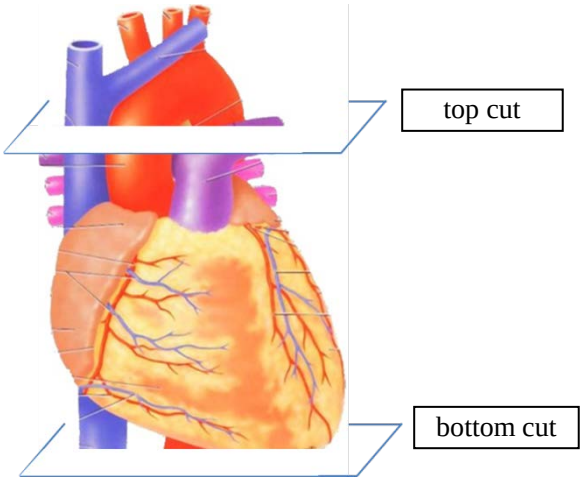

Figure 6.7 Cut off cardiac regions.

6.3.1 DATA SET

Image used in this experiment are 5 normal chest CT volumes with a resolution of that voxel spacing varies from 0.723 to 0.683[mm] in-plane and from 0.5 to 1[mm] between consecutive slices.

6.3.2 PROCESSING

We propose a hybrid segmentation method that integrates fast marching method [26] and the statistical shape model method, for automated segmentation of cardiac regions. According to adjust the time parameter of fast marching method, we could reduce the overflow parts from the cardiac regions to liver regions (refer the Fig. 6.6). At the same time, segmented region is then utilized as the initial location of shape model. Finally, we control the deformation of shape model using rigid transformation algorithm to match the cardiac regions and "cut" the top and bottom parts which are treated as the overlap using fast marching. The proposed method is outlined as follow.

Algorithm 5:

1) *Set the seed points manually and extract cardiac regions at the first time using fast marching method.*
2) *Calculate the mass center of the extracted region in step 1. Align the center of model to this point and uniform the radius of model to this region.*
3) *Collect the candidate boundary points of image which are near the landmarks.*
4) *Search the finial position for model using ICP.*
5) *Cut the top and bottom regions according to the position of shape model.*

The time term of fast marching method is provided by the function of the gradient magnitude. To cast the input of speed term to a proper range, we use a sigmoid function to control parameters that can be customized to shape a nice speed image. The mapping should be done in such a way that the propagation speed of the front will be very low close to high image gradients while it will move rather fast in low gradient areas. This arrangement will make the contour propagate until it reaches the edges of anatomical structures in the image, i.e. the contour propagate should result in large changes on the

time-crossing map values close to the structure edges.

6.3.3 RESULTS

5 cases of segmentation results are listed in Tab. 6.3. Comparing the liver segmentation experiments, here we added the Hausdorff distance and mean absolute surface distance indices were utilized, which have been stated in section 2.5.5 and section 2.5.6. The 3-D reconstructed surface models are attached to Appendix C. At the same time, segmentation experiment using fast marching only was performed too. As the results, the TPR was 0.650 and FPR was 0.002.

Table 6.3 Evaluation of cardiac segmentation experiments.

Case	***TPR***	***FPR***	***Hausdorff***	***Mean Distance***
1	0.500	0.000	19.698	0.031
2	0.684	0.001	23.264	0.245
3	0.647	0.000	11.152	0.034
4	0.577	0.000	22.236	0.015
5	0.652	0.002	27.495	0.520
Average	0.612	0.001	20.769	0.169

Hausdorff: Hausdorff distance. ***Mean Distance***: Mean absolute surface distance.

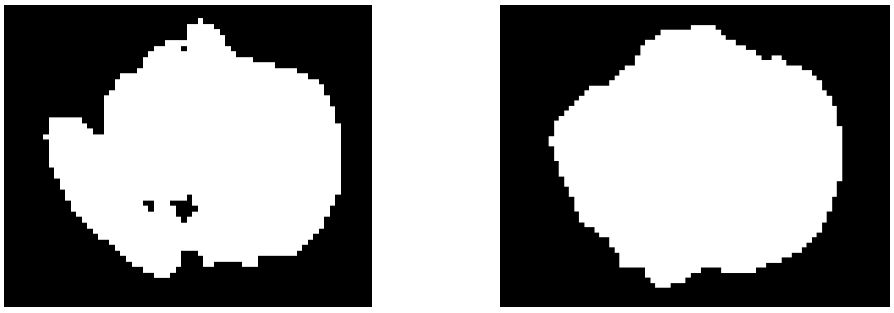

(a) (b)

Figure 6.8 Comparison of segmentation results. (a) Segmented result by fast marching method. (b) Gold standard data.

6.3.4 DISCUSSION

A beyond expectation is that the fast marching for the first segmentation did not lead to higher precision of results. Because the fact that most part of cardiac regions are surrounded by the lung regions, and contrast of pixel value between the lung regions and the cardiac regions are obvious. We thought that if the stop time is adaptive, the TPR of segmented result by fast marching should be not less than 0.90. However, even increasing the iteration time of fast marching, the results were not improved too much. The intermediate results to obtain a map image for fast marching are demonstrated in Fig. 6.9. Although from the result of gradient magnitude filter the significant boundaries were found. When enhancing the edge image by sigmoid window filter (sub-graph(c)), we can see some “black holes” inside of candidate region. These noises are caused by the complex inner structures of cardiac, such as ventricles and atriums. That would block the surface propagation of fast marching.

As the improvement of proposed method, we consider to exchange the order of implement. Firstly limit the arrangement of cardiac regions using shape model. To complete this, we can get the threshold image of chest CT images, place the mean shape model to the nearby of ROI, and then surround ROI by model using ICP algorithm. After removed the outside regions of ROI, instead of the boundary-based method, this time region-based method is utilized to refine the segmentation result gotten in previous step.

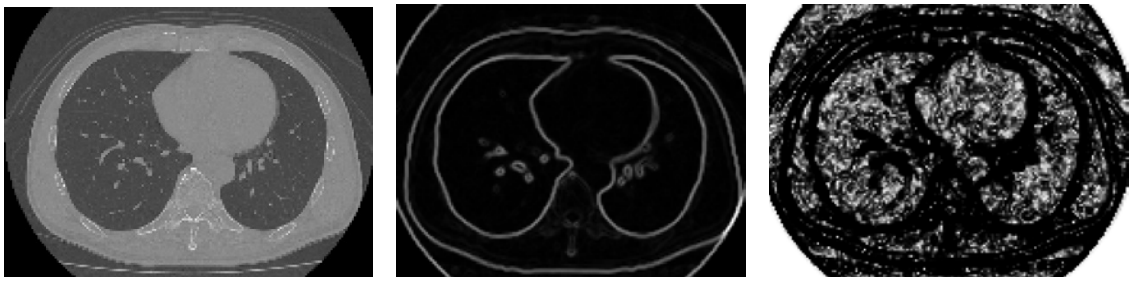

(a) (b) (c)

Figure 6.9 Preprocessing images for fast marching method. (a) Smoothing image using anisotropic diffusion filter. (b) Edge image by gradient magnitude filter. (c) Enhancing the edge map image by sigmoid filter.

6.4 CONLUSIONS

From the experiment of segmentation of liver regions, although isotropic processing for a serial of DICOM images has been a standard step before all other processes. We still think that in some case the isotropic processing breaks the resolution of the original images, since we should meet the scale of slice thick by reducing the interval spacing of intra-slice. As to the segmentation of un-enhancement images, to utilize the valuable edge information, slice-by-slice implement maybe a better choice. Of course, it is not wisdom to substitute the 2-D shape model for 3-D shape model.

Due to noise influence and partial volume effect, the edges of organs or structures in medical images are usually not clearly defined. As a result, we always need a hybrid method to complete a segmentation task. There is currently no single segmentation method that can yield acceptable results for every medical image. Combining several segmentation techniques together to form a hybrid framework can sometimes significantly improve the segmentation performance and robustness comparing to each individual component.

CHAPTER 7: VISUALIZATION TECHNOLOGY AND ITS APPLICATIONS

Image post-processing is defined as the process of integrating a series of axial images into a form that is often easier to interpret than the sections themselves [134]. The source transverse section is a fundamental image for interpretation. At the first of this section, we briefly review the 3-D visualization techniques in practice. Integrating image processing techniques and visualization techniques, computer-assisted radiology and surgery have opened up completely new possibilities for modern medicine. In the second part, we grasp up newest scientific and technological trends of 3-D medical segmentation.

7.1 VISUALIZATION TECHNOLOGY

7.1.1 VISUALIZATION FOR VOLUME DATA

7.1.1.1 Maximum Intensity Projection (MIP)

MIP is a projection technique, in which only the highest density pixel in the projection direction is displayed to reconstruct the 2-D images. MIP image allows the differentiation between enhanced high density structures and low density structures. MIP image reconstructed from the same volume data shows ROI, but their outlines merge; it is impossible to visualize the spatial relationships between the objects on the MIP image. In practice, MIP is usually performed interactively with a sliding slab, enabling the radiologist to adjust the window, select the optimal orientation to display the object in the special density level.

7.1.1.2 Multi-planar Reformation (MPR)

MPR is a high-resolution reconstruction format that allows display of planar images at any angular section through the acquisition volume, which permits visualization in not only the axial plane but also interactive planes that better follow the ROI course in the 3-D image. The slice thickness can be modified, and a thick slab may be helpful in

visualizing special structures.

7.1.1.3 Volume Rendering

Volume rendering techniques allow us to see the inhomogeneity inside objects. Roughly, it could be categorized into direct rendering techniques and geometric primitive rendering techniques. Take the CT images for example, we can realistically reproduce X-ray images by considering the intensity process at this point in the text, you can imagine extending our ray tracing example from the previous section. Thus rays not only interact with the surface of an object, they also interact with the interior [135]. To obtain richer expressive, opacity and color are assigned to each CT value interval via transfer function. For example, normal soft tissue is assigned high transparency, enhanced vascular structures slight opaqueness and bone strong opaqueness. The sum of all CT values along each search ray from the observer through the 3-D data volume, weighted by the transfer function, is displayed [136].

7.1.2 VISUALIZATION FOR SURFACE DATA

7.1.2.1 Surface rendering

Surface rendering algorithm is applied to place surface patches or tiles at each contour point, and with hidden surface removal and shading. They use a relatively small amount of contour data, resulting in fast rendering speeds. One category of the surface rendering techniques is polygon rendering methods concentrate on the visualization of data through the use of geometric primitives such as points, lines, and polygons. For medical applications such as human body visualization [137, 138] and statistical shape analysis, this is obviously the most efficient and effective representation for the data. However, although this representation could reduce data storing space, some authors pointed out that there are still many phenomena that cannot be simulated using surface rendering techniques alone. This is particularly true if we are trying to render data interior to an object, such as X-ray intensity from a CT scan [139]. Fig. 7.1 demonstrates two different representation of human skull model.

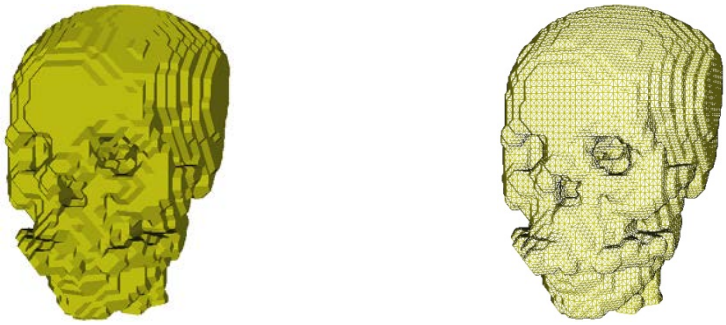

(a) (b)

Figure 7.1 Surface rendering of a skull. (a) Display in voxels. (b) Display in polygons

7.1.2.2 Texture mapping

Texture mapping is a technique to add detail to an image without requiring modeling detail. It is one of the most commonly used methods to improve the realism or to assistant shape analysis. In Fig. 5.4, a regular lattice map is mapped to the lung surface. As a result, the properties of spherical conformal mapping could be appeared intuitively. In paper [142], the authors propose a new texture mapping method, based on flattening a chain-coded 3-D surface, to handle the voxel-based data directly. The method flattens the 3-D object surface onto a 2-D plane and then uses 2-D metamorphosis to generate the correspondences between object surface and texture image. Therefore, polygon transformation is no longer necessary and texture mapping is handled with inexpensive 2-D morphing. More importantly, the internal information of medical data can be easily preserved and utilized further.

7.2 APPLICATIONS OF 3-D SEGMENTATION

7.2.1 MEDICAL DIAGNOSE

CAD system is a relatively new concept that has been developed largely during the last decades, and that is growing rapidly in diagnostic radiology and medical physics. From the mental of CAD, the computer output as an “aided opinion” to improve the diagnostic accuracy. In the development of various CAD schemes, it is necessary to employ image processing and information-processing techniques for quantitative analysis of images. In

addition, it is necessary to understand the medically relevant content of the images on the basis of technical features [1]. For example, for detecting lesions by computer, it may be useful to provide a 3-D visualization to the radiologists that the characters and type of lesions is easier to recognize. Fig. 7.2 shows a 3-D display to analyze breast lesions.

7.2.2 Shape Analysis

Medical image segmentation is of considerable importance in providing noninvasive information about human body structures that helps radiologists to visualize and analyze the anatomy of the structures. Shape analysis is always used in education in anatomy. For example, evidence suggests that shape changes of brain structures may reflect abnormalities in neurodevelopmental disorders and neurodegenerative diseases, such as attention deficit hyperactivity disorder (ADHD) [143], schizophrenia [144], and Alzheimer's disease [145]. Fig. 7.3 shows an example to analyze the mean curvature of a lung surface model.

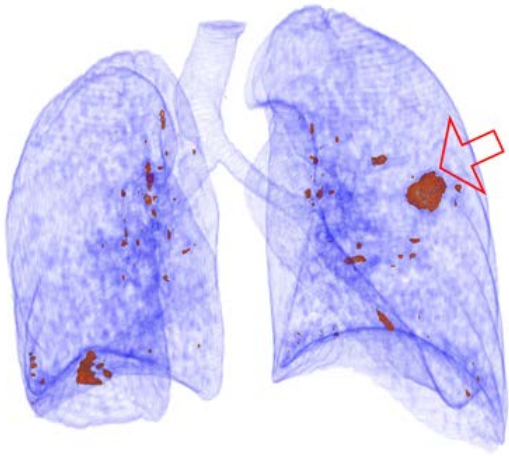

Figure 7.2 Prompt the position of lesions in 3-D space.

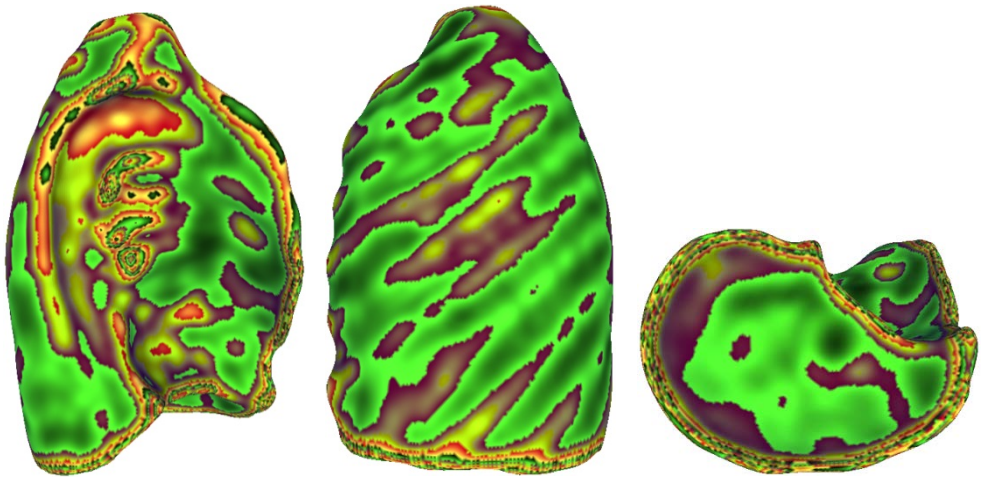

Figure 7.3 Surface model of left lung. The degree of mean curvature is distinguished with color.

7.2.3 Education in Anatomy

The derived virtual body models are a novel interactive tool for reference and education in anatomy. Detailed 3-D anatomy may be viewed from all directions, dissected with any number of cut planes, and even anatomical linked knowledge can be combined in these statistic models. One of the basic skills of a radiologist is to interpret 3-D anatomy form 2-D X-ray images. The model allows the simulation of X-rays from any direction and with any beam geometry since the absorption values for every voxel are available from the original CT data (as Fig. 7.4(a)). Based on the information contained in the model, both the contributing anatomical structures and the extent of their contribution to the total absorption may be computed and visualized in the context of 3-D anatomy [146]. The similar technology could also be used as the simulation of sonographic examinations [147].

7.2.4 Operation Assistance

In Intra-operative navigation scenarios, recovering and analyzing 3-D shape are used to assist making scenarios. For example, in the procedure for bone augmentation, pre-operative CT images are used for pre-operative planning, based on a 3-D finite element analysis of the patient's femur and planned cement injection [148]. The pre-operative

model and plan are registered to the patient and intra-operative navigation system, and a robotic device is used to inject cement containing an appropriate contrast agent (Fig.7.4 (b)). In liver surgery planning, the first step is the segmentation of the image data in order to tag the liver and diseased areas of liver tissue [130]. Non-coronary cardiovascular findings and extra-cardiac findings should be reviewed in addition to recognize primary and secondary comorbid pathology that leads to alternative non-cardiovascular diagnoses [149]. The Fig. 7.4 demonstrates commercial 3-D medical imaging software VOXEL-MAN®, which is developed by University Medical Center Hamburg-Eppendorf. It has been successfully applied in such as medicine education and operation simulation [150].

7.2.5 Applications of 3-D Segmentation in Machine Vision and Computer Graph

The next important milestone for embodied machine vision systems is to make them flexible and robust in a variety of environments and tasks. In [151], authors proposed an active 3D scene segmentation and detection method for an object grasping robot and manipulation system.

The analysis of 3-D face meshes is also important in many applications, which aim to accurately relate information from different meshes in order to compare them. In [152], P. Nair proposed an accurate and robust framework for detecting and extracting faces, localizing landmarks and achieving fine registration of face meshes based on 3-D PDM.

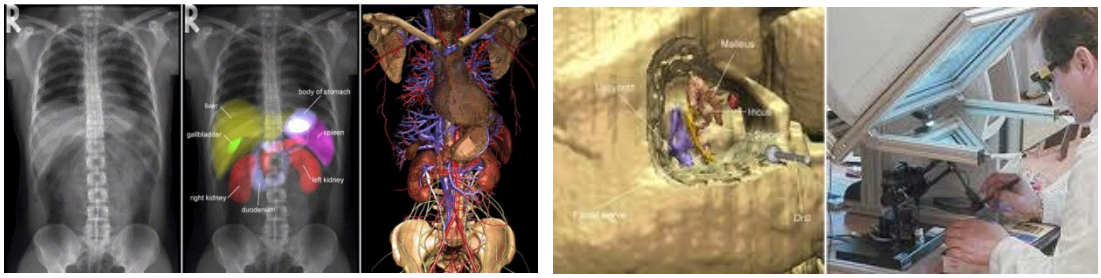

(a) (b)

Figure 7.4 Partial functions ofVOXEL-MAN® software (a) Correlation of X-ray images with 3D anatomy. (b) TempoSurg® training system for petrous bone surgery.

Recently, the application of depth cameras available at commodity prices has been increased. These cameras can usually capture both color and depth images in real-time, with limited resolution and accuracy. In [153], they study the problem of 3-D deformable face tracking with such commodity depth cameras.

Surface parameterization methods which were stated in section 5.2 have been applied widely in decades [154]. Apart from the application for brain diagnosis (section 7.2.2), in computer graphic fields, the power of these methods are also realized. Rendering realistic faces and facial expressions requires good models for the reflectance of skin and the motion of the face. The [155] described such a system. It realistically reproduces the appearance of a particular person's face and facial expressions. Some excellent works presented in these papers demonstrates in Fig. 7.5.

(a)

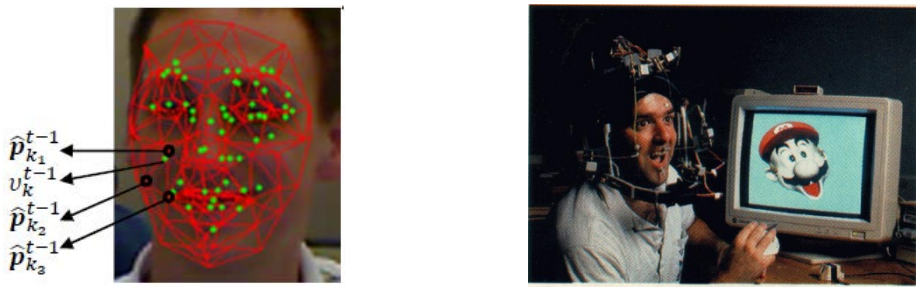

(b) (c)

Figure 7.5 Applications of 3-D segmentation. (a)Recognition of 3-D objects for manipulation system [101]. (b)Track 3-D feature points cloud of face [103]. (c)Human facial movements and phonemes are digitized to be used by animated character.

7.3 CONCLUSIONS

The last few decades have witnessed significant advances in medical imaging and computer-aided medical image analysis. The revolutionary capabilities of new multidimensional medical imaging modalities and computing power have opened a new window for medical research and clinical diagnosis. In this procedure, the medical image segmentation techniques are the primary tools for such as automatic diagnosis, the quantification of tissue volumes, localization of pathology, study of anatomical structure, treatment planning, partial volume correction of functional imaging data and so on. We think in the near future, anatomical variability, pathology and other spatial knowledge representation could also be included into the model, and more completed human model will play more important role in medical science and clinic.

CHAPTER 8: CONCLUSIONS AND FUTURE WORKS

8.1 CONCLUTIONS

Segmentation technology in medical imaging is seemed as the “Medusa’s eye” that filling with the temptation as well as the challenge. It is the major bottleneck for translating advanced computer-based procedures into clinical practice and one of the most crucial operations to develop the CAD system. Any image visualization, manipulation, and analysis tasks require directly or indirectly image segmentation. In spite of several decades of research, this still largely remains an open problem.

In this thesis, we proposed a framework to solve medical image segmentation problems. Although it is not a completely new methodology in this domain, following this framework, we could consider the construction for the Object Oriented Programming (OOP) based software project. This method is similar as the framework of registration project done in Insight Segmentation and Registration Toolkit (ITK). So, we hope the practices in medical image segmentation could be benefit of this method.

Atlas (statistical model) based methods have resulted in substantial and widespread advances in the field of medical image segmentation. The study on human themselves is the basic to solve medical imaging problems. Active shape model method is one of the pioneers in this domain. Here we attempt to optimize parameters by an intelligent approach. In spite of time-consuming when utilizing genetic algorithm to obtain the parameters directly, introduction of intelligent optimization method seems to be potential on accuracy improvement. In addition, we think that many excellent control theories are able to use in model based imaging methods.

Regard to the 3-D SSM building, we have to admit that the approaches presented in this thesis are just a start. However, from the correspondence results in Appendix B.1, the

automatically mapped landmarks are located near the corresponding positions robustly, although they have not been as exactly as possible. We think the proposed methods are suitable for the initialization of landmarks. Many novel researching reports have been known in decades, and even some researches predict that the statistics based methods would be one step towards the final goal of automatic segmentation task in the clinic.

In this study, we proposed a novel alignment method using surface features and stereographic projection. This strategy provided a new viewpoint to solve the orientation for a 3-D object. From Appendix A, the surface features of one class of objects appear quite regular. We believe that these algorithms could be easily embedded in many applications and provide a thorough basis for computing may image statistics.

Each method has its special talents. In this thesis, we practiced the main three categories of novel segmentation methods in medical imaging: region growing, level set methods and Deformable model methods. We are conscious that it is impossible to improve the segmentation accuracy without combining more information to any method above. Meanwhile we think that just taking account of single object but overlooking the relationship of anatomical structure is fruitless.

8.2 FUTURE WORKS

Below is a list of future work, arising from the observations in this thesis:

Implement the multiple-organic shape statistic, i.e. body atlas. As mentioned earlier, using single statistical model is not able to master the processing of segmentation. Even to a radiologist, it is inconceivable that drawing the boundary perfectly without referring the issue regions around the ROI. To obtain a statistical model, combining the complex image information to one model is necessary. The knowledge includes such as locations of organs, local appearance information, curvature etc.

Alignment or registration of 3-D objects is able to be regarded as an independent research field. Orientations driven methods break out the general viewpoint about accessing the uniformity of special objects, which makes the minimizing Euclidean distance of two surfaces as the standard. We anticipate this method and its derivate could play a role to solve the problems of alignment of one class of objects, which have the same structures but various shapes.

Refine the landmark points based statistic shape model methods. To obtain a more reasonable shape model, we should assume an objective function to measure the “quality” of a model. This approach that has been taken is based on the idea that a good model should allow a concise description of the members of the training set. Some pioneering methods have been proposed, such as Minimum Description Length (MDL) principle. Another strategy is described as searching the key-points in parameter domain. Since the harmonic mapping methods are able to prevent the information of surface curvatures. Lots of feature description methods in image processing area, such as Scale-Invariant Keypoints [156], are considered to be utilized for searching the corresponding positions of landmarks between surface data.

Two main techniques utilized in this thesis---shape statistical method and surface parameterization are considered to be applied in wider areas, which are not confined of medical imaging but also machine vision. Especially, with the development of 3-D printing technology, reconstructions of 3-D shapes and computational geometry will be gained insight. As well the marriage of these two approaches is a relatively new approach in the world of vision research that we can hope the truly understand the deeper aspects of the human visual system, and the human mind.

BIBLIOGRAPHY

[1] K. Doi, “Diagnostic imaging over the last 50 years: research and development in medical imaging science and technology,” *Physics in Medicine and Biology*, vol. 51, no. 13, pp. R5-R27, 2006.

[2] Z. Ma, J. Manuel, “A review of algorithms for medical image segmentation and their applications to the female pelvic cavity,” *Computer Methods in Biomechanics and Biomedical Engineering*, vol. 13, no. 2, pp. 235-246, 2010.

[3] D. L. Pham, C. Xu, J. L. Prince, “A survey of current methods in medical image segmentation,” *Annual Review of Biomedical Engineering*, vol. 2, no.1, pp. 315-338, 2000.

[4] S. Pieper, M. Halle, R. Kikinis, *3D Slicer* [Online], Available: http://www.na-mic.org.

[5] D.T. Lin, C.C. Lei, S.W. Hung, “Computer-aided kidney segmentation on abdominal CT images,” *IEEE Trans. Inf. Technol. Biom.*, vol. 10, no. 1, pp. 59-65, 2006.

[6] The Visible Human Project: Informatic Bodies and Posthuman Medicine, Taylor & Francis press, 2005.

[7] H.F. Ng, “Automatic thresholding for defect detection,” *Pattern Recognition Letters*, vol. 27, no. 14, pp. 1644-1649, 2006.

[8] N. Otsu, “A threshold selection method from gray-level histograms,” *Automatica*, vol. 11, no. 285-296, pp. 23-27, 1975.

[9] R.V. Andreao, J. Boudy, “Combining Wavelet Transform and Hidden Markov Models for ECG Segmentation,” *EURASIP Journal on Applied Signal Processing*, vol. 1, p.95, 2007.

[10] K.S. Chuang, H.L. Tzeng et al., “Fuzzy c-means clustering with spatial information for image segmentation,” *Computerized medical imaging and graphics*, vol. 30, no. 1, pp. 9-15, 2006.

[11] R. Adams, “Seeded region growing,” *IEEE Trans. Pattern Anal. Mach. Intell.*, vol. 16, no. 6, pp. 641-647, 1994.

[12] K. Haris, S.N. Efstratiadis et al., “Hybrid Image Segmentation Using Watershed and Fast Region Merging,” *IEEE Trans. Image Proc.*, vol. 7, no. 12, pp. 1684-1699, 1998.

[13] O. Gomez, J.A. Gonzalez, E.F. Morales, “Image segmentation using automatic seeded region growing and instance based learning,” in *Progress in Pattern Recognition, Image Analysis and Applications*, Springer Berlin Heidelberg, 2007. pp. 192-201.

[14] J. Dehmeshki, X. Ye, J. Costello, “Shape Based Region Growing Using Derivatives of 3D Medical Images: Application to Semiautomated Detection of Pulmonary Nodules,” in *Image Processing, 2003. ICIP 2003 Processings. 2003 Int. Conf. on*. p.l-1085-8.

[15] R. Pohle, K.D. Toennies, “Segmentation of Medical Images Using Adaptive Region Growing,” in *Proc. SPIE Medical Imaging*, pp. 1337-1346, 2001.

[16] C.G. Rafael, E.W. Richard, *Digital Image Processing*, Pearson Prentice Hall press, 2008.

[17] V. Grau, A.U.J. Mewes, “Improved Watershed Transform for Medical Image Segmentation Using Prior Information,” *IEEE Trans. Med. Imag.*, vol. 23, no. 4, pp. 447-458, 2004.

[18] G. Hamarneh, X.X. Li, “Watershed Segmentation Using Prior Shape and Appearance Knowledge,” *Image and Vision Computing*, vol. 27, no. 1, pp. 59-68, 2009.

[19] S. Osher, J. A. Sethian, “Fronts propagating with curvature-dependent speed: algorithms based on Hamilton-Jacobi formulations,” *J. computational physics*, vol. 79, no. 1, pp. 12-49, 1988.

[20] R. Malladi, J.A.Sethian, “Level Set and Fast Marching Methods in Image Processing and Computer Vision,” in *Image Proc., 1996. Proc., Int. Conf. on IEEE*, pp. 489-492.

[21] S. Kichenassamy, A. Kumar et al., “Conformal Curvatures Flows: From Phase Transitions to Active Vision,” *Archive for Rational Mechanics and Analysis*, vol. 134, no. 3, pp. 275-301, 1996.

[22] V. Caselles, R. Kimmel, G. Sapiro, “Geodesic active contours,” *Int. J. computer vision*, vo. 22, no. 1, pp. 61-79, 1997.

[23] J.S. Suri, K.C. Liu et al., “Shape Recovery Algorithms Using Level Sets in 2-D/3-D Medical Imagery: A State-of-

the-Art Review," *IEEE Trans. Inf. Tech. in Biomed.*, vol. 6, no. 1, pp. 8-28, 2002.

[24] T. Chan, L.A. Vese, "Active Contour and Segmentation Models Using Geometric PDE's for Medical Imaging," in *Geometric Methods in Bio-Medical Image Proc.*. Springer Berlin Heidelberg, 2002. pp. 63-75.

[25] D. Cremers, M. Rousson, R. Deriche, "A Review of Statistical Approaches to Level Set Segmentation: Integrating Color, Texture, Motion and Shape," *Int. J. computer vision*, vol. 72, no. 2, pp. 195-215, 2007.

[26] J.A. Sethian, *Level Set Methods and Fast Marching Methods: evolving interfaces in computational geometry, fluid mechanics, computer vision, and materials science*, Cambridge university press, 1999.

[27] R. Malladi, J.A. Sethian, B.C. Vemuri, "Shape modeling with front propagation: A level set approach," *IEEE Trans. Pattern Anal. Machine Intell.*, vol. 17, no. 2, pp. 158-175, 1995.

[28] Z. Wu, R. Leahy, "An Optimal Graph Theoretic Approach to Data Clustering: Theory and Its Application to Image segmentation," *IEEE Trans. Pat. Anal. Mach. Intell.*, vol. 15, no. 11, pp. 1101-1113, 1993.

[29] J. Shi, J. Malik, "Normalized cuts and image segmentation," *IEEE Trans. Anal. Machine Intell.*, vol. 22, no.8, pp. 731-737, 1997.

[30] Y. Boykov, M. Jolly, "Interactive graph cuts for optimal boundary and region segmentation of objects in n-d images," in *Proc. Eighth IEEE Int. Conf. Computer Vision (ICCV)*, pp. 105-112, 2001.

[31] S. Wang, J. Siskind, "Image segmentation with ratio cut," *IEEE Trans. Pat. Anal. Machine Intell.*, vol. 25, no. 6, pp. 675-690, 2003.

[32] D. Grosgeorge, C. Petitjean , J.-N. Dacher, S. Ruan, "Graph cut segmentation with a statistical shape model in cardiac MRI," *Computer Vision and Image Understanding*, in press.

[33] L. Grady, "Random walks for image segmentation," *IEEE Trans. Pattern Anal. Mach. Intell.*, vol. 28, no. 11, pp. 1768-1783, 2006.

[34] M. Kass, A. Witkin, D. Terzopoulos, "Snakes: Active Contour Models," *Int. J. Computer Vision*, vol. 1, no. 4, pp. 321-331, 1988.

[35] L.D. Cohen, I. Cohen, "Finite Element Methods for Active Contour Models and Balloons for 2D and 3D Images," *IEEE Trans. Pattern Anal. Mach. Intell.*, vol. 15, no. 11, pp. 1131-1147, 1991.

[36] C. Xu, J. L. Prince, "Snakes, Shapes, and Gradient Vector Flow," *IEEE Trans. Image Proc.*, vol. 7, no. 3, pp. 359-369, 1998.

[37] T. McInerney, D. Terzopoulos, "T-snakes: Topology adaptive snakes," *Medical Image analysis*, vol. 4, no. 2, pp. 73-91, 2000.

[38] L. He, Z.G. Peng et al., "A comparative Study of Deformable Contour Methods on Medical Image Segmentation," *Image and Vision Computing*, vol. 26, no. 2, pp. 141-163, 2008.

[39] T.F. Cootes, C.J. Taylor, D.H. Cooper, J. Graham, "Active shape models-their training and application," *Computer vision and image understanding*, vol. 61, no. 1, pp. 38-59, 1995.

[40] T.F. Cootes, G.J. Edwards, C.J. Taylor, "Active appearance models," *IEEE Trans. Pattern Anal. Mach. Intell.*, vol. 23, no. 6, pp. 681-685, 2001.

[41] R. Beichel, H. Bischof et al., "Robust Active Appearance Models and Their Application to Medical Image Analysis," *IEEE Trans. Med. Imag.*, vol. 24, no. 9, pp. 1151-1169, 2005.

[42] T. McInerney, D. Terzopoulos, "Deformable Models in Medical Image Analysis: A Survey," *To appear in Medical Image Analysis*, vol. 1, no. 2, pp. 91-108, 1996.

[43] S. Sun, C. Bauer, R. Beichel, "Automated 3-D Segmentation of lungs With Lung Cancer in CT Data Using a Novel Robust Active Shape Model Approach," *IEEE Trans. Med. Imag.*, vol. 31, no. 2, pp. 449-460, 2012.

[44] *Co-Planar Stereotaxic Atlas of the Human Brain*: *3-Dimensional Proportional System: An Approach to Cerebral Imaging*, Thieme Medical Publisher press, 1988.

[45] D.L. Collins, C.J. Holmes, T.M. Peters, A.C. Evans, "Automatic 3D model-based neuroanatomical segmentation," *Human Brain Mapping*, vol. 3, no. 3, pp. 190-208, 1995.

[46] A.O. Akinyemi, "Atlas-based segmentation of medical images," Ph.D dissertation, University of Glasgow, 2011.

[47] L.P. Dzung, X. Chenyang, L.P. Jerry, "A survey of current methods in medical image segmentation," Tech. Rep., Department of ECE, Johns Hopkins Univ., 1999.

[48] R.D. Deriche, "Recursively implementing the Gaussian and its derivatives," Tech. Rep., INRIA Sophia Antipolis, 1993.

[49] S. Acton, “Multigrid anisotropic diffusion,” *IEEE Trans. Imag. Proc.*, vol. 7, no. 3, pp. 280-291, 1998.

[50] L. Alvarez, J.M. Morel, “Morphological approach to multiscale analysis: From principles to equations,” in *Geometry-Driven Diffusion in Computer Vision. Springer Netherlands*, pp. 229-254, 1994.

[51] J. Weickert, *Anisotropic Diffusion in Image Processing*, Stuttgart Teubner, 1998.

[52] Q. Li, S. Sone, K. Doi, “Selective enhancement filters for nodules, vessels, and airway walls in two- and three-dimensional CT scans,” *Medical physics*, vol. 30, pp. 2040-2051, 2003.

[53] G. Hamarneh, C. Mcintosh, “Physics-based deformable organisms for medical image analysis,” in *Medical Imaging, Int. Society for Optics and photonics*, 2005, pp. 326-335.

[54] T.F. Cootes, C.J. Taylor, “Combining point distribution models with shape models based on finite element analysis,” *Image and Vision Computing*, vol. 13, no. 5, pp. 403-409, 1995.

[55] M. Bressan, J. Vitrià, “Independent Modes of Variation in Point Distribution Models,” *Visual Form 2001*. Springer Berlin Heidelberg, 2001. pp. 123-134.

[56] R. Larsen, K. Baggesen et al., “Some Issues of Biological Shape Modelling with Applications,” *Image Analysis*, Springer Berlin Heidelberg, 2003. pp. 509-519.

[57] P. Yushkevich, S.M. pizer, “Intuitive, Localized Analysis of Shape Variability,” in *Inf. Proc. in Medical Imaging*, Springer Berlin Heidelberg, 2001. pp. 402-408.

[58] M. Styner, “Automatic and Robust Computation of 3D Medial Models Incorporating Object Variability,” *Int. J. Computer Vision*, vol. 55, no. 2-3, pp. 107-122, 2003.

[59] K. Leventon, W.E.L. Grimson, O. Faugeras, “Statistical Shape Influence in Geodesic active contours nfluence in Geodesic active contours,” in *Proc. IEEE Conf. Computer Vision and Pattern Recognition*, pp.316-323, 2000.

[60] H. Blum, *A transformation for extracting new descriptors of shape, Models for the Perception of Speech and Visual Form*, MIT Press, 1967.

[61] S.M. Pizer, P.T. Fletcher, “Deformable M-Reps for 3D Medical Image Segmentation,” *Int. J. Computer Vision*, vol. 55, pp. 2-3, pp. 85-106, 2003.

[62] M. Styner, J.A. Lieberman, “Boundary and medial shape analysis of the hippocampus in schizophrenia,” *Medical Image Analysis*, vol. 8, no. 3, pp. 197-203, 2003.

[63] G. Szekely, A. Kelemen, C. Brechbuhler, G. Gerig, “Segmentation of 2D and 3D objects from MRI volume data using constrained elastic deformations of flexible Fourier contour and surface models,” *Medical Image Analysis*, vol. 1, no. 1, pp. 19-34, 1996.

[64] A. Matheny, D.B. Goldgof, “The use of three- and four- dimensional surface harmonics for rigid and nonrigid shape recovery and representation,” *IEEE Trans. Pat. Anal. Mach. Intell.*, vol. 17, no. 10 pp. 967-981, 1995.

[65] Nikou, G. Bueno, F. Heitz, J.P. Armspach, “A joint physics-based statistical deformable model for multimodal brain image analysis,” *IEEE Trans. Med. Imag.*, vol. 20, no. 10, pp. 1026-1037, 2001.

[66] Davatzikos, D. Liu, D. Shen, E.H. Herskovits, “Spatial normalization of spine MR images for statistical correlation of lesions with clinical symptoms,” *Radiology*, vol. 224, no. 3, pp. 919-926, 2002.

[67] Nain, S. Haker, A. Bobick, A. Tannenbaum, “Multiscale 3D shape representation and segmentation using spherical wavelets,” *IEEE Trans. Med. Imag.*, vol. 26, no. 4, pp. 598-618, 2007.

[68] M.A. Styner, “Combined Boundary-Medial Shape Description of Variable Biological Objects,” PhD dissertation, University of North Carolina at Chapel Hill, Chapel Hill, NC, 2001.

[69] D.L. Pham, C. Xu, J.L. Prince, “A Survey of Current Methods in Medical Image Segmentation,” *Annu. review of biomedical Engineering*, vol. 2, no. 2, pp. 315-338, 2000.

[70] H. Li, “Fractal Modeling and Segmentation for the Enhancement of Microcalcifications in Digital Mammograms,” *IEEE Trans. Med. Imaging*, vol. 16, no. 6, pp. 785-798, 1997.

[71] J. M. Keller, S. Chen, “Texture description and segmentation through fractal geometry,” *Computer Vision, Graphics, and Image Proc.*, vol. 45, no. 2, pp. 150-166, 1989.

[72] J. Rogowska, “Overview and Fundamentals of Medical Image Segmentation,” in *Handbook of Medical Image Processing and Analysis*, Academic Press in an imprint of Elsevier, 2008, pp. 73-84.

[73] I. Pitas, *Digital Image Processing Algorithms and applications*, John Wiley & Sons, 2000.

[74] V. Grau, A.U.J. Mewes, “Improved Watershed Transform for Medical Image Segmentation Using Prior Information,” *IEEE Trans. Med. Imag.*, vol. 23, no.4, pp. 447-458, 2004.

[75] P.J. Besl, “A Method for Registration of 3-D Shapes,” *IEEE Trans. Pattern Anal. Mach. Intell.*, vol. 14, no. 2, 1992.

[76] A.W. Fitzgibbon, “Robust registration of 2D and 3D point sets,” *Image and Vision Computing*, vol. 21, no. 13, pp. 1145-1153, 2003.

[77] D. Cohen, “On active contour models and balloons,” in *CVGIP: Image understanding*, vol. 53, no. 2, pp. 211-218, 1991.

[78] P.K. Pandey, Y. Singh, S. Tripathi, “Image Processing using Principla Component Analysis,” *Int. J. Computer Applications*, vol. 15, no. 4, pp. 1975-8887, 2011.

[79] C.K. Wikle, “A kernel-based spectral model for non-Gaussian spatio-temporal processes,” *Statistical Modelling*, vol. 2, no. 4, pp. 299-314, 2002.

[80] A. Hyvarinen, J. Karhunen, E. Oja, *Independent Component Analysis*, John Wiley & Sons Press, 2001.

[81] K.M. Pohl, J. Fisher et al., “A Bayesian model for joint segmentation and registration,” *NeuroImage*, vol. 31, no.1, pp. 228-239, 2006.

[82] U. Maulik, “Medical Image Segmentation Using Genetic Algorithms,” *IEEE Tran. Inf. Technol. Biomed.*, vol. 13, no. 2, pp. 166-173, 2009.

[83] F. Masulli, A. Schenone, “A fuzzy clustering based segmentation system as support to diagnosis in medical imaging,” *Artificial Intelligence in Medicine*, vol. 16, no. 2, pp. 129-147, 1999.

[84] W.E. Reddick, “Automated Segmentation and Classification of Multispectral Magnetic Resonance Images of Brain Using Artificial Neural Networks,” *IEEE Trans. Med. Imag.*, vol. 16, no. 6, pp. 911-918, 1997.

[85] J.K. Udupa, V.R. leBlanc et al., “A framework for evaluating image segmentation algorithms,” *Computerized Medical Imaging and Graphics*, vol. 30, no. 2, pp. 75-87, 2006.

[86] S.K. Warfield, K.H. Zou, W.M. Wells, “Simultaneous truth and performance level estimation (STAPLE): an algorithm for the validation of image segmentation,” *IEEE Trans. Med. Imag.*, vol. 23, no. 7, pp. 903-921, 2004.

[87] G. Gerig, M. Jomier, M. Chakos, “Valmet: A new validation tool for assessing and improving 3D object segmentation,” *Medical Image Computing and Computer-Asisted Intervention---MICCAI 2001*. Springer Berlin Heidelberg, 2001. pp. 516-523.

[88] L. Lee, “Measures of Distributional Similarity,” in *Proc. of the 37th annual meeting of the Assiciation for Computational Linguistics on Computational Linguisticsm*. Association for Computational Linguistics, 1999. pp. 25-32.

[89] P. Jaccard, “The distribution of the flora in the alpine zone,” *New Phytologist*, vol. 11, no. 2, pp. 37-50, 1912.

[90] D.P. Huttenlocher, G.A. Klanderman, W.J. Rucklidge, “Comparing Images Using the Hausdorff Distance,” *IEEE Trans. Pattern Anal. Mach. Intell.*, vol. 15, no. 9, pp. 850-863, 1993.

[91] A. Robertson, “The Sampling Variance of The Genetic correlation Coefficient,” *Biometrics*, vol. 15, no. 3, pp. 469-485, 1959.

[92] A. Lanitis, T.F. Cootes, C.J. Taylor, “Automatic Interpretation and Coding of Face Images Using Flexible Models,” IEEE Trans. Pattern Anal. Mach. Intell., vol. 19, no. 7, pp. 743-756, 1997.

[93] A. Hill, T.F. Cootes, C.J. Taylor, “Active shape models and the shape approximation problem,” *Image and Vision Computing*, vol. 14, no. 8, pp. 601-607, 1996.

[94] N. Duta, M. Sonka, “Segmentation and interpretation of MR brain images: an improved active shape model,” *IEEE Trans. Med. Imag.*, vol. 17, no. 6, pp. 1049-1062, 1998.

[95] Lekadir, R. Merrifield, G.Z. Yang, “Outlier detection and handling for robust 3-D active shape models search,” *IEEE Tran. Med. Imag.*, vol. 26, no. 2, pp. 212-222, 2007.

[96] Y. Shang, O. Dossel, “Statistical 3D shape-model guided segmentation of cardiac images,” in *Computers in Cardiology*, pp. 553-556, 2004.

[97] B. Tsagaan, A. Shimizu, H. Kobatake, K. Miyakawa, “An automated segmentation method of kidney using statistical information,” in *Medical Image Computing and Computer-Assisted Intrvention---MICCAI 2002*. Springer berlin Heidelberg, 2002, pp. 556-563.

[98] M.B. Stegmann, “Active Appearance Models: Theory extensions and cases,” *Informatics and Mathematical Modelling*, p. 262, 2000.

[99] J. Park, D. Metaxas, A.A. Young, L. Axel, “Deformable Models with Parameter Functions for Cardiac Motion

Analysis from Tagged MRI Data," *IEEE Trans. Med. Imag.*, vol. 15, no. 3, pp. 1-13, 1996.

[100] J.C. Gower, "Generalized procrustes analysis," *Psychometrika*, vol. 40, no. 1, pp. 33-51, 1975.

[101] C. Goodall, "Procrustes methods in the statistical analysis of shape," *J. the Royal Statistical Society* B, vol. 53, no. 2, pp. 285-339, 1991.

[102] L. Thomas, W. Stefan, R. Karl, M.S. Peter. "Landmark-based 3D elastic registration of pre- and postoperative liver CT data," in *Bildverarbeitung für die Medizin 2009*, pp. 107-111.

[103] M. Andriy, X. Song, "Point Set Registration: Coherent Point Drift," *IEEE Trans. Pattern. Anal. Mach. Intell.*, vol. 32, no. 12, pp. 2262-2275, 2011.

[104] J. Bing, B.C. Vemuri, "Roust Point Set Registration Using Gaussian Mixture Models," *IEEE Trans. Pattern Anal. Mach. Intell.*, vol. 33, no. 8, pp. 1633-1645, 2011.

[105] J. Qu, L Gong, L Yang, "A 3D point matching algorithm for affine registration," *Int. J. computer assisted radiology and surgery*, vol. 6, no. 2, pp. 229-236, 2011.

[106] D. Han, J. Bayouth et al., "Motion artifact Reduction in 4D Helical CT: Graph-based Structure Alignment," *Medical Computer Vision. Recognition Techniques and Applications in Medical Imaging.* Springer Berlin Heidelberg, 2011. pp. 63-73.

[107] Available: http://rsbweb.nih.gov/ij/

[108] W.E Lorensen, "Marching cubes: A high resolution 3D surface construction algorithm," in *ACM Siggraph Computer Graphics*, pp. 163-169, 1987.

[109] T.S. Newman, H. Li, "A survey of the marching cubes algorithm," *Computer & Graphics*, vol. 30, no. 5, pp. 854-879, 2006.

[110] R. Dyer, H. Zhang, T. Moller, "Delaunay Mesh Construction," in *Eurographics Symposium on Geometry Processing*, pp. 273-282, 2007.

[111] D.S. Meek, D.J. Walton, "On surface normal and Gaussian curvature approximations given data sampled from smooth surface," *Computer Aided Geometric Design*, vol. 17, no. 6, pp. 521-543, 2000.

[112] M. Meyer, M. Desbrun, P. Schröder and A.H. Barr, "Discrete Differential- Geometry Operators for Triangulated 2-Manifolds," unpublished.

[113] T. Kanungo, N.S. Netanyahu, A.Y. Wu, "An Efficient k-Means Clustering Algorithm: Analysis and Implementation," *IEEE Trans. Pattern Anal. Mach. Intell.*, vol. 24, no.7, pp. 881-892, 2002.

[114] B.K.P. Horn, "Closed-form Solution of Absolute Orientation Using Unit Quaternions," *JOSA A*, vol. 4, no. 4, pp. 629-642, 1987.

[115] J. Arvo, "Fast Random Rotation Matrices," in *Graphics Gems III*, Academic Press professional, 1992, pp. 117-120.

[116] T. Heimann, H. Meinzer, "Statistical Shape Models for 3D Medical Image Segmentation: A review," *Medical Image Analysis*, 13(4): 543-563, 2009.

[117] A. Keleman, G. Szekely, G. Gerig, "Elastic model-based segmentation of 3-D neuroradiological data sets," *IEEE Trans. Med. Imag*, vol. 18, no. 10, pp. 828-839, 1999.

[118] R.H. Davies, C.J. Twining, T.F. Cootes, C.J. Taylor, "Building 3-D statistical Shape Models by Direct Optimization," *IEEE Trans. Med. Imag.*, vol. 29, no. 4, pp. 961-981, 2010.

[119] T. Heimann, I Volf, H.P. Meinzer, "Optimal landmark distributions for statistical shape model construction," in *Medical Imaging Int. Society for Optics and Photonics*, p. 61441J, 2006.

[120] T. Okada, K. Yokota, et al., "Construction of Hierarchical Multi-Organ Statistical Atlases and Their Application to Multi-Organ Segmentation from CT Image," in *Medical Image Computing and Computer-Assisted Intrvention---MICCAI 2008.* Springer berlin Heidelberg, 2008. pp. 502-509.

[121] H. Zhang, A. Sheffer et al., "Deformation-driven shape correspondence," *Computer Graphics Forum*, vol. 27, no. 5, pp. 1431-1439, 2008.

[122] M.S. Floater, K. Hormann, "Surface Parameterization: a Tutorial and Survey," in *Advances in Multiresolution for Geometric Modelling mathematics and Visualization*, pp. 157-186, 2005.

[123] X.D. Gu, Y. Wang et al., "Genus Zero Surface Conformal Mapping and Its Application to Brain Surface Mapping", *IEEE Trans. Med. Imag.*, vol. 23, no. 8, pp. 949- 958, 2004.

[124] X.D. Gu, S.T. Yau, *Computational Conformal Geometry*. Higher Education Press, 2008.

[125] X. Gu, S.T. Yau, "Computing Conformal Structures of Surfaces," *Communications in Information and Systems*, vol. 2, no. 2, pp. 121-146, 2002.

[126] R.H. Davies, C.J. Twining, C.J. Taylor, *Statistical Models of Shape: Optimisation and Evaluation*. Springer, 2008.

[127] M.A. Styner, K.T. Rajamani et al., "Evaluation of 3D Correspondence Methods for Model Building," in *Information proc. in medical imaging*. Springer Berlin Heidelberg, 2003. pp. 63-75.

[128] S.G. Armato III et al., "The Lung Image Database Consortium (LIDC) and Image Database Resource Initiative (IDRI): A Completed Reference Database of Lung Nodules on CT Scans," *Medical physics*, vol. 38, pp. 915-931, 2011.

[129] S. Sun C. Bauer, R. Beichel, "Automated 3-D Segmentation of Lungs with Lung Cancer in CT Data Using a Novel Robust Active Shape Model Approach," *IEEE Trans. Med. Imag.*, vol. 31, no. 2, pp. 449-460, 2012.

[130] H.G. Debarba, D.J. Zanchet et al., "Efficient Liver Surgery Planning in 3D based on Functional Segment Classification and Volumetric Information," in *Engineering in Medicine and Biology(EMBC), 2010 Annu. Int. Conf. of the IEEE*. pp. 4797-4800, 2010.

[131] P. Campadelli, E. Casiraghi, "Liver Segmentation from CT Scans: A Survey," *Applications of Fuzzy Sets Theory*. Spring Berlin Heidelberg, 2007. pp. 520-528.

[132] H. Lamecker, T. Lange, M. Seebass, *Segmentation of the Liver using a 3D Statistical Shape Model*, Konrad-Zuse-Zentrum für Informationstechnik, 2004.

[133] J. Schulz-Menger, D.A Bluemke, "Standardized image interpretation and post processing in cardiovascular magnetic resonance: Society for Cardiovascular Magnetic Resonance (SCMR) Board of Trustees Task Force on Standardized Post Processing," *J. Cardiovasc. Magn. Reson.*, vol. 15, no. 1, p.35, 2013.

[134] M. Jinzaki, M. Yamada, "Image post-Processing and Interpretation," *Advances in the Diagnosis of Coronary Atherosclerosis*, pp. 305-330, 2011.

[135] W. Schroeder, K. Martin, B. Lorensen, *The Visualization Toolkit---An Object-Oriented Approach to 3D Graphics*, Kitware Press, 2006.

[136] P.S. Calhoun, B.S. Kuszyk et al., "Three-dimensional Volume Rendering of Spiral CT Data: Theory and Method," *Radio Graphics*, vol. 19, no.3, pp. 745-764, 1999.

[137] J. Toriwaki, K. Mori, "Visualization of the human body toward the navigation diagnosis with the virtualized human body," *J. Visualization*, vol. 1, no. 1, pp. 111-124, 1998.

[138] Aslanidi, M.A. Colman et al., "3D virtual human atria: a computational platform for studying clinical atrial fibrillation," in *biophysics and molecular biology*, vol. 107, no. 1, pp. 156-168, 2011.

[139] K.H. Hühne, B. Pflesser et al., *VOXEL-MAN 3D Navigator: Inner Organs. Regional, Systemic and Radiological Anatomy*, Springer-Verlag Electronic Media, 2003.

[140] B. Reitinger, "Virtual Liver Surgery planning: Simulation of Resections using Virtual Reality Techniques," Ph.D. dissertation, Graz University of Technology, 2005.

[141] E. Burmester, T. Leineweber et al, "EUS meets VOXEL-MAN: Three- dimensional anatomic animation of linear-array endoscopic ultrasound images," *Endoscopy*, vol. 36, no. 8, pp. 726-730, 2004.

[142] T.L. Weng, S.J. Lin et al., "Voxel-based texture mapping for medical data," *Computerized Medical Imaging and Graphics*, vol. 26, no. 6, pp. 445-452, 2002.

[143] A. Qiu, D. Crocetti et al., "Basal ganglia volume and shape in children with attention deficit hyperactivity disorder," The *American J. psychiatry*, vol. 166, no. 1, pp. 74-82, 2009.

[144] K.L. Narr, P.M. Thompson et al., "Three-dimensional mapping of gyral shape and cortical surface asymmetries in schizophrenia: Gender effects," The *American J. psychiatry*, vol. 158, no. 2, pp. 244-255, 2001.

[145] L. Apostolova, J. Morra et al., "Automated 3d mapping of baseline and 12-month associations between three verbal memory measures and hippocampal atrophy in 490 ADNI subjects," *Neuroimage*, vol. 51, no. 1, pp. 488-499, 2010.

[146] A. Criminisi, J. Shotton et al., "Validating automatic semantic annotation of anatomy in DICOM CT images," in *SPIE Mededical Imaging*. Int. Society for optics and Photonics, 2011. p. 796704.

[147] A. Fenster, D.B. Downey, H.N. Cardinal, "Three-dimensional ultrasound imaging," *Physics in medicine and biology*, vol. 46, no. 5, pp. 67-99, 2001.

[148] B. pflesser, A. Petersik et al., "Volume cutting for virtual petrous bone surgery," *Computer Aided Surgery*, 7: 74-83, 2002.

[149] N. Oyama-Manabe, T. Sugaya et al., “Non-Coronary Cardiac Findings and Pitfalls in Coronary Computed Tomography Angiography,” *J. Clinical Imaging Science*, vol. 1, no. 51, pp. 1-7, 2011.

[150] H.H. Karl, P. Bemhard et al., *VOXEL-MAN 3D-Navigator: Inner Organs-Regional, Systemic and Radiological Anatomy*, Springer Electronic media, 2003.

[151] M. Bjorkman, K. Danica, “Active 3d scene segmentation and detection of unknown objects”, in *IEEE Int. Conf. Robotics and automation* (*ICRA)*, pp. 3114-3120, 2010.

[152] P. Nair, A. Cavalloro, “3-D Face Detection, Landmark Localization, and Registration Using a Point Distribution Model,” *IEEE Trans. Multimedia*, vol. 11, no. 4, pp. 611-623, 2009.

[153] Q. Cai, D. Gallup et al., “3D Deformable Face Tracking with a Commodity Depth Camera,” in *Computer Vision---ECCV 2010*. Springer Berlin Heidelberg, pp. 229-242, 2010.

[154] S. Alla, E. Praun, K. Rose, “Mesh parameterization methods and their applications,” in *Foundations and Trends® in Computer Graphics and Vision*, vol. 2, no. 2, pp. 105-171, 2006.

[155] P. Ratner, *3-D Human Modeling and Animation*. John Wiley & Sons press, 2009.

[156] Lowe, G. David, “Object recognition from local scale-invariant features,” in *Computer vision, 1999. The proc. of the seventh IEEE int. conf. on.* pp. 1150-1157.

APPENDIX A: UNFOLDED GAUSS MAPS OF LEFT LUNG MODELS

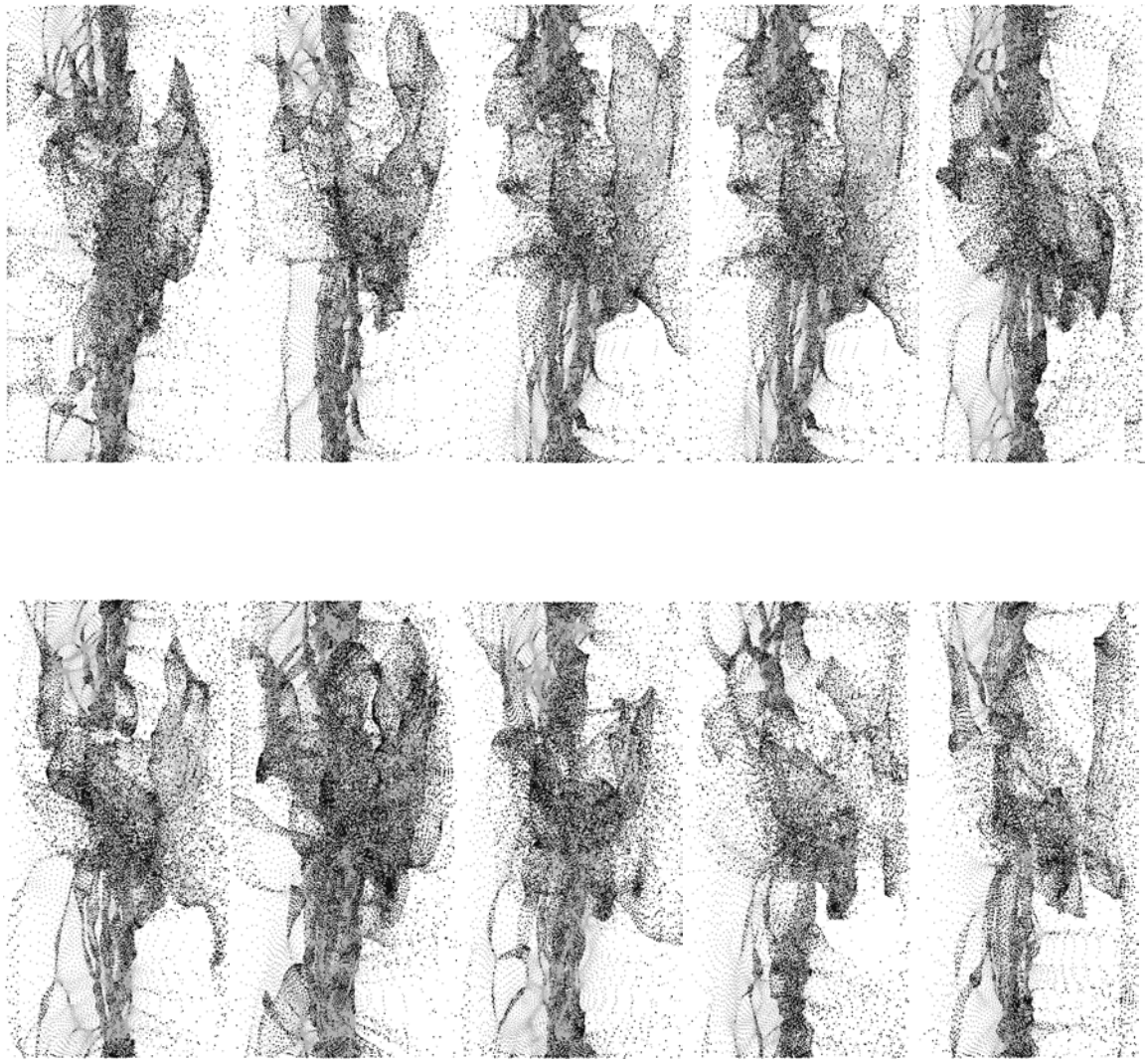

APPENDIX B: CORRESPONDENCE RESULTS

1. Results by the proposed method of section 5.3.1.

There are two cases on opposite viewpoints in each row.

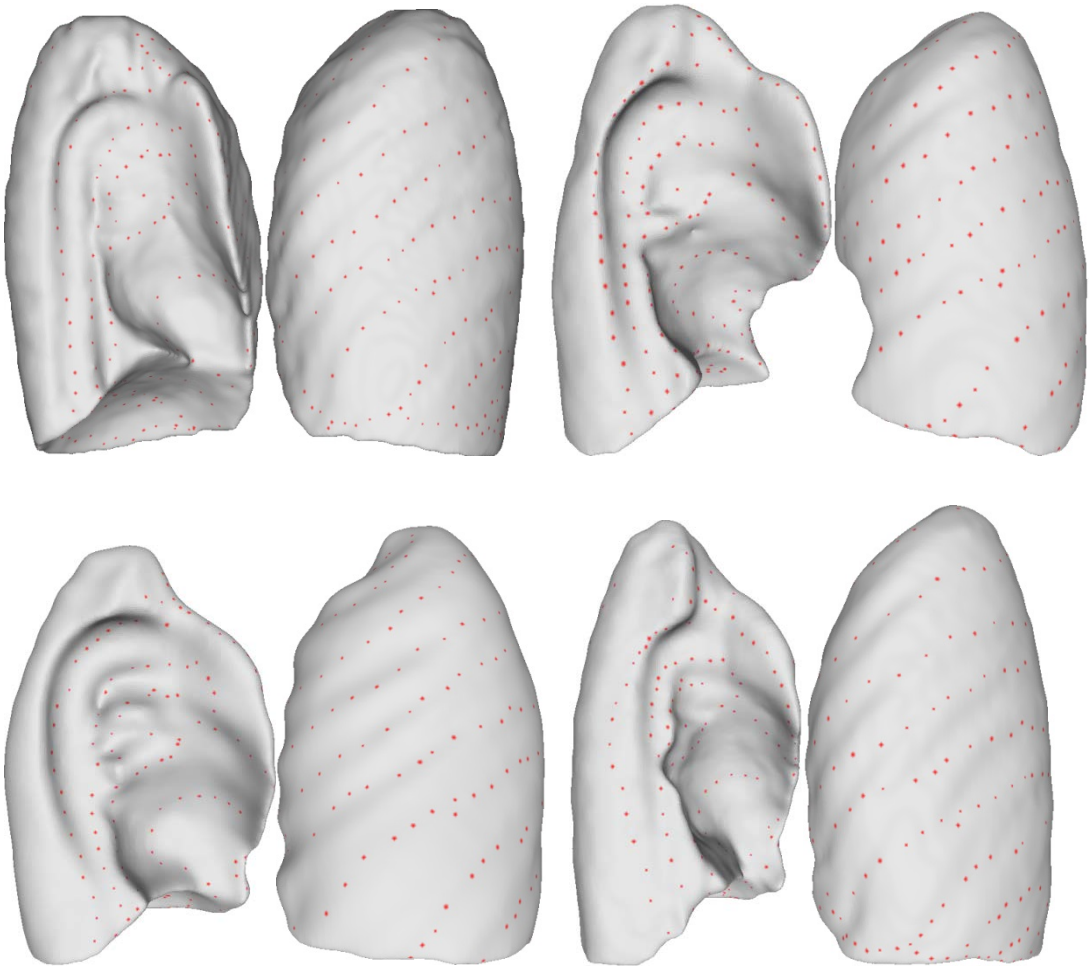

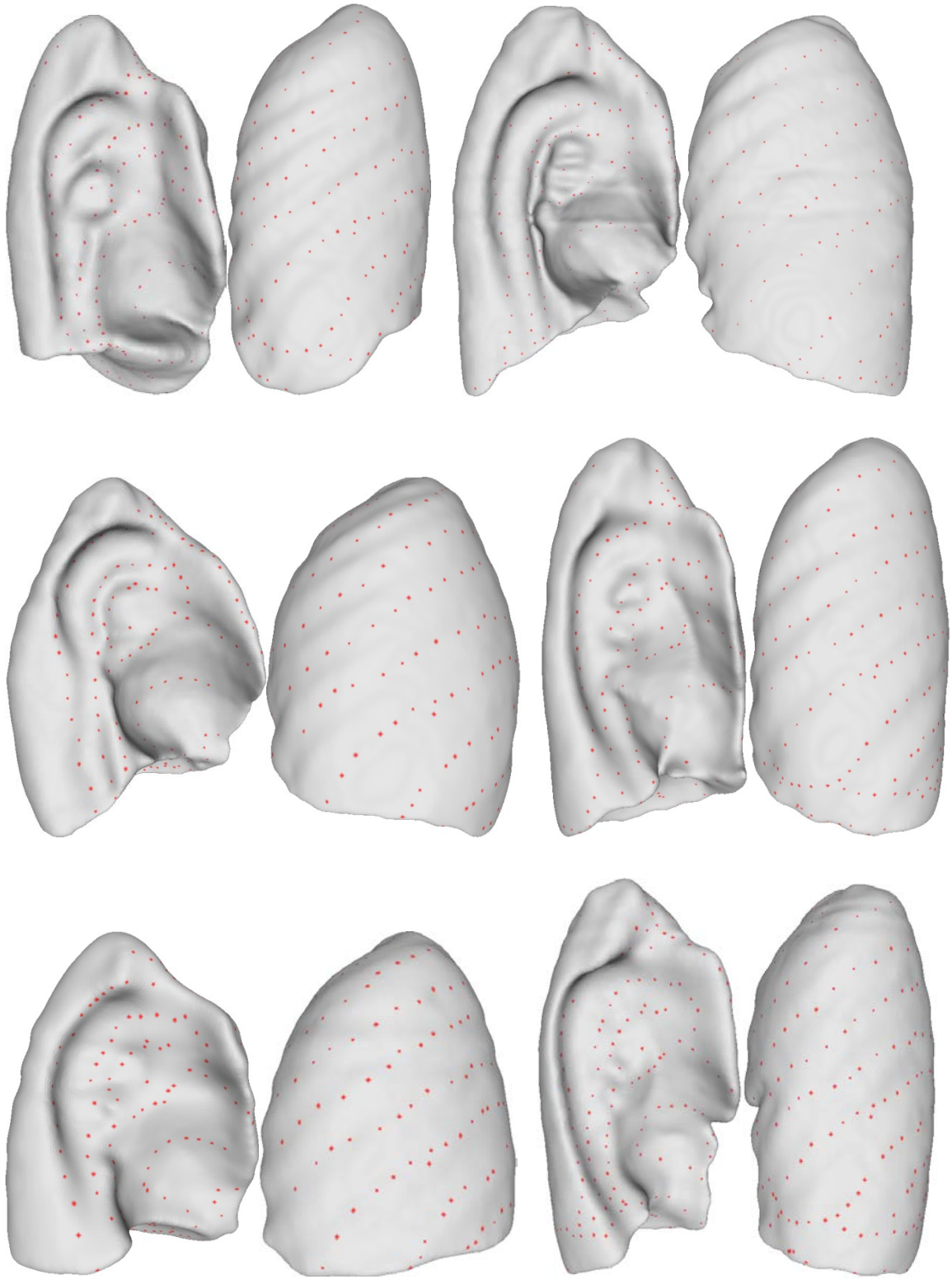

2. Results by the proposed method of section 5.3.2.

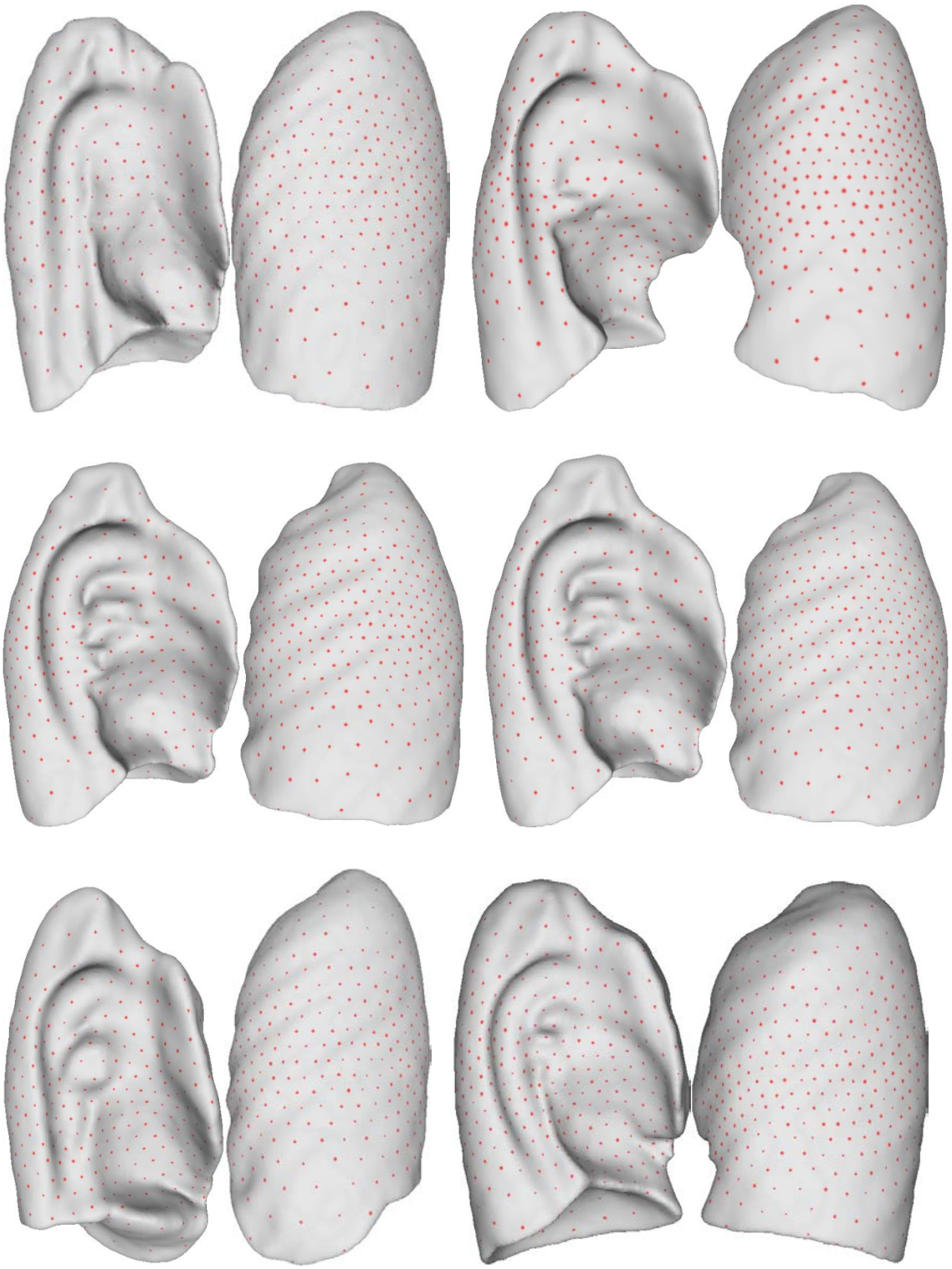

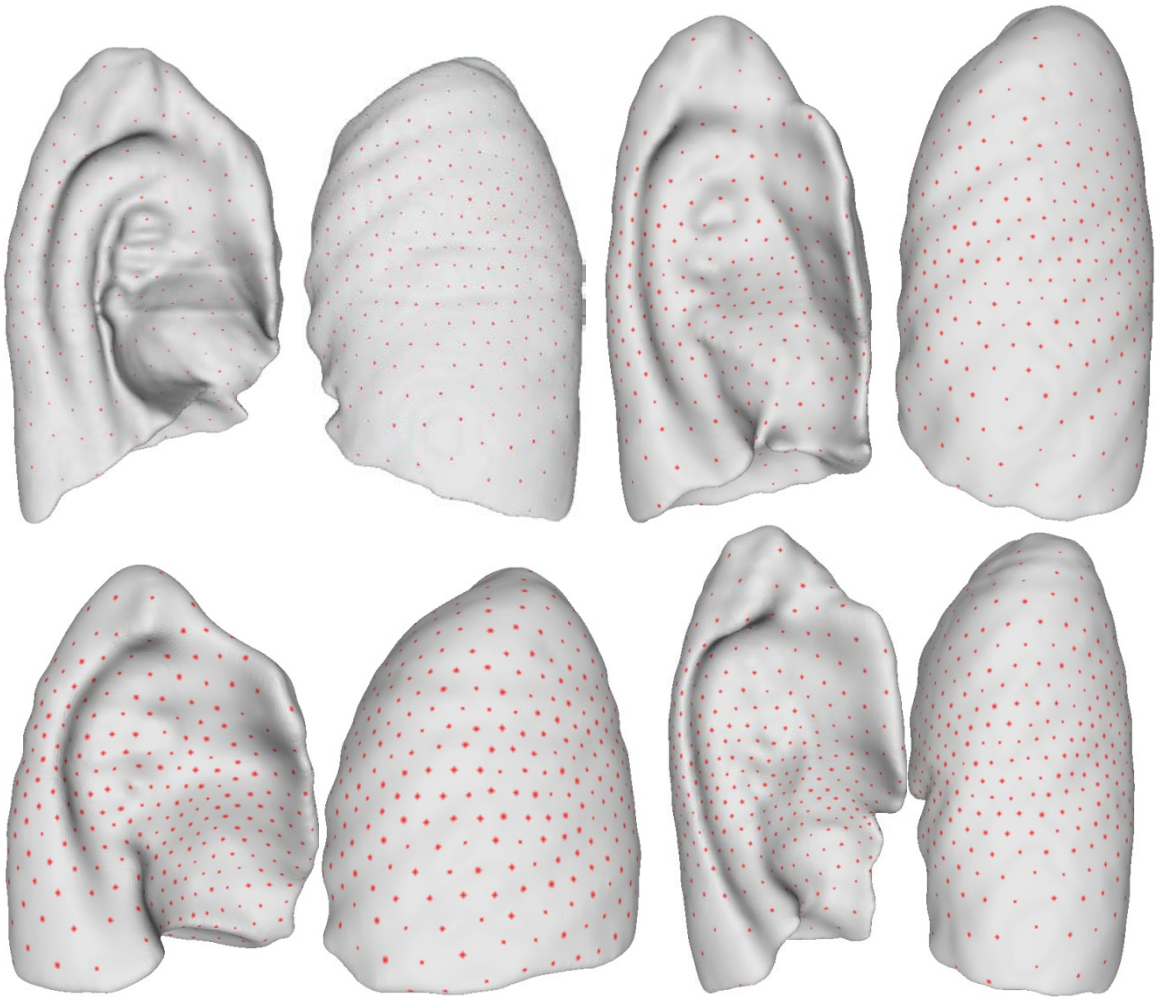

APPENDIX C: SEGMENTATION RESULTS

1. Segmentation results of lung regions (10 cases).

Each case is arranged in a row on 3 viewpoints.

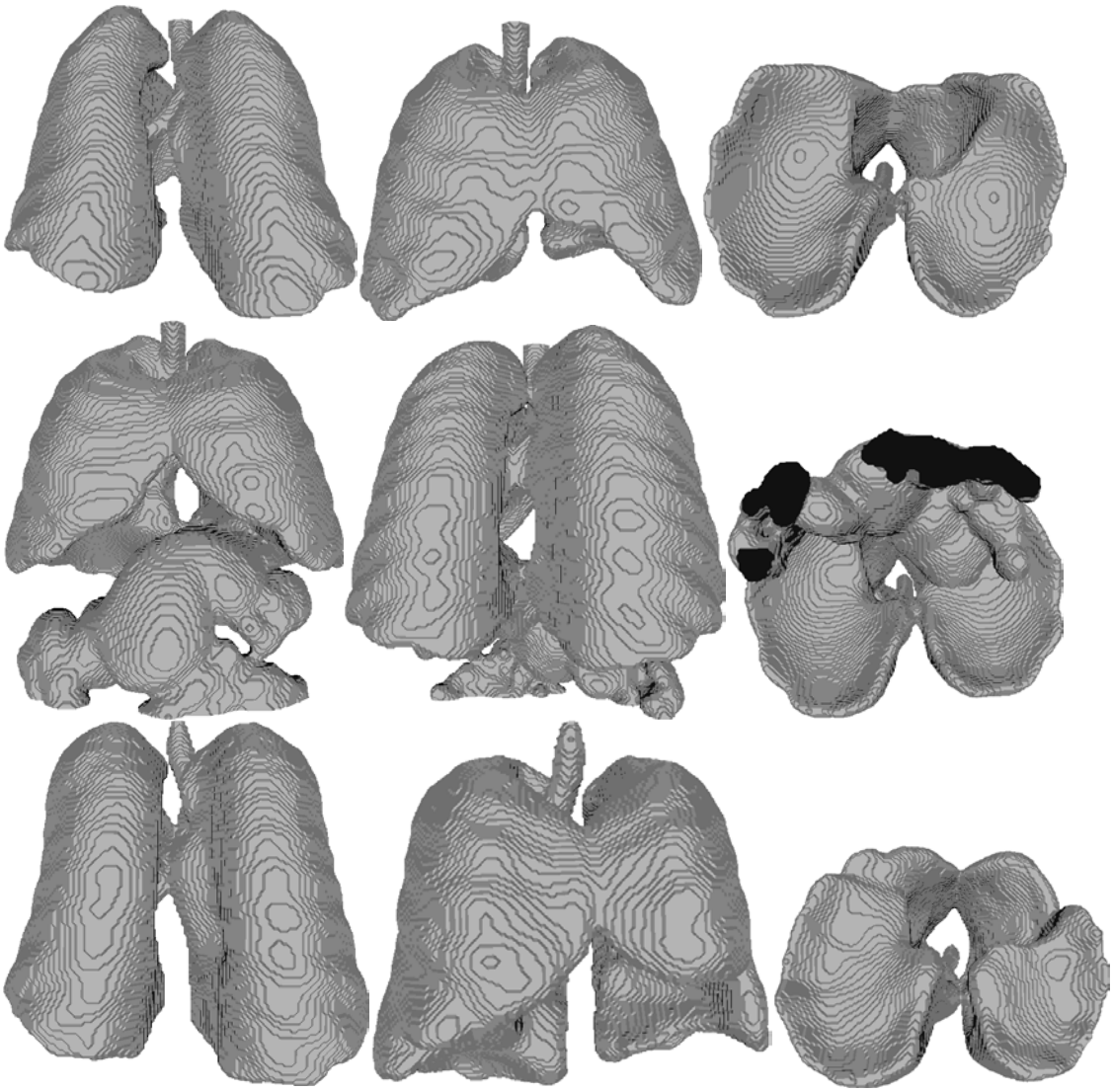

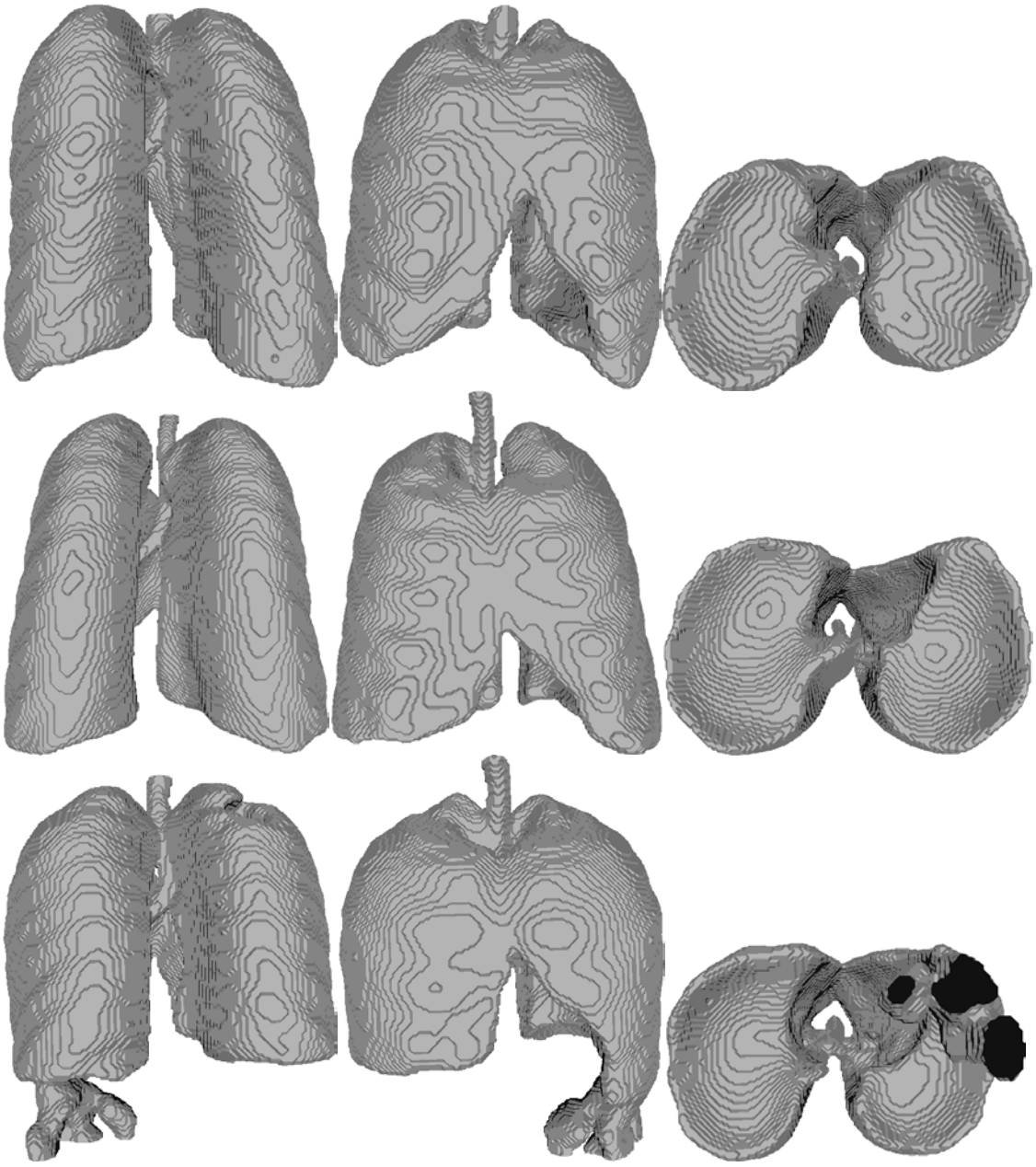

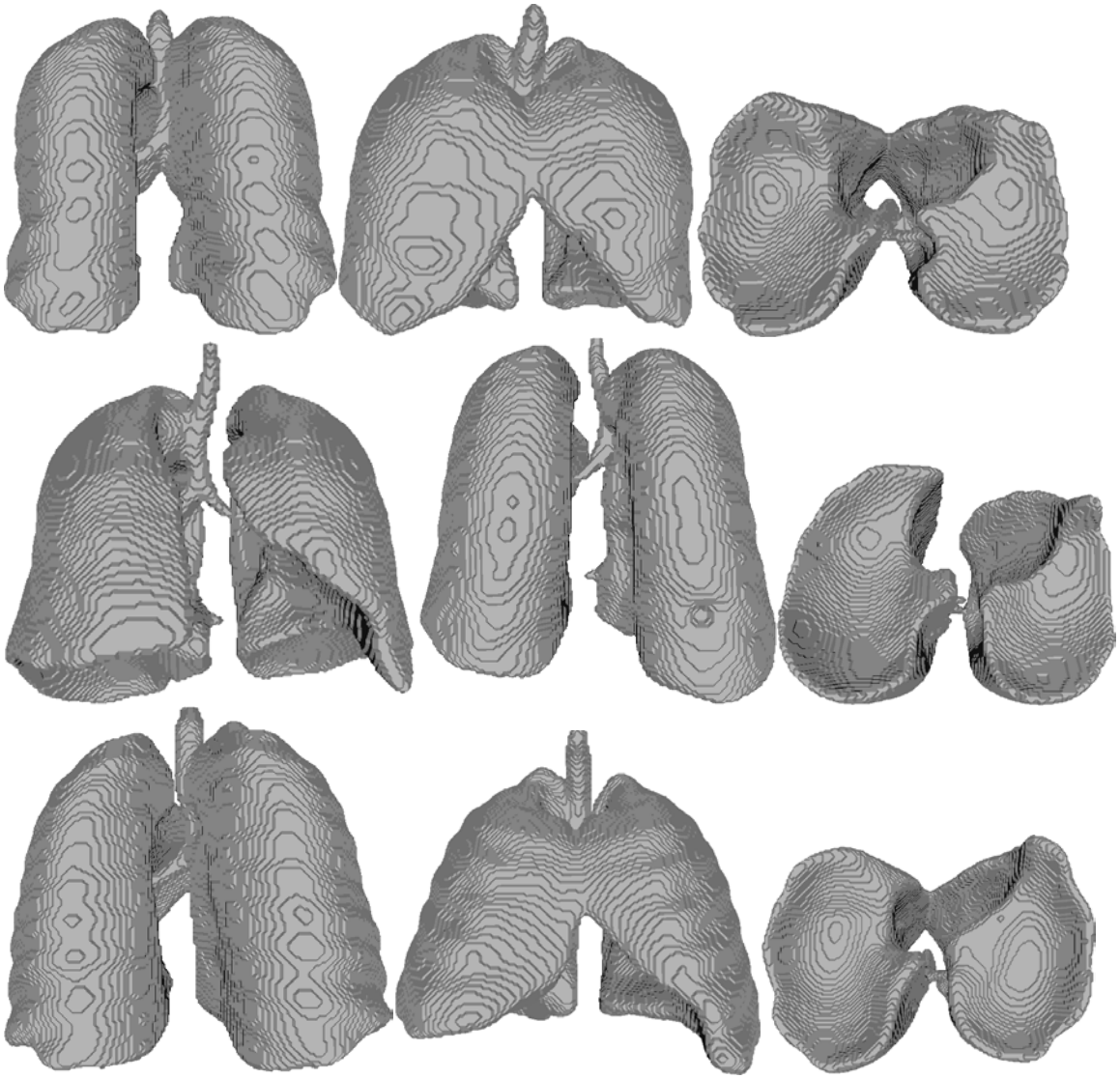

1. Segmentation results of liver regions (10 cases).

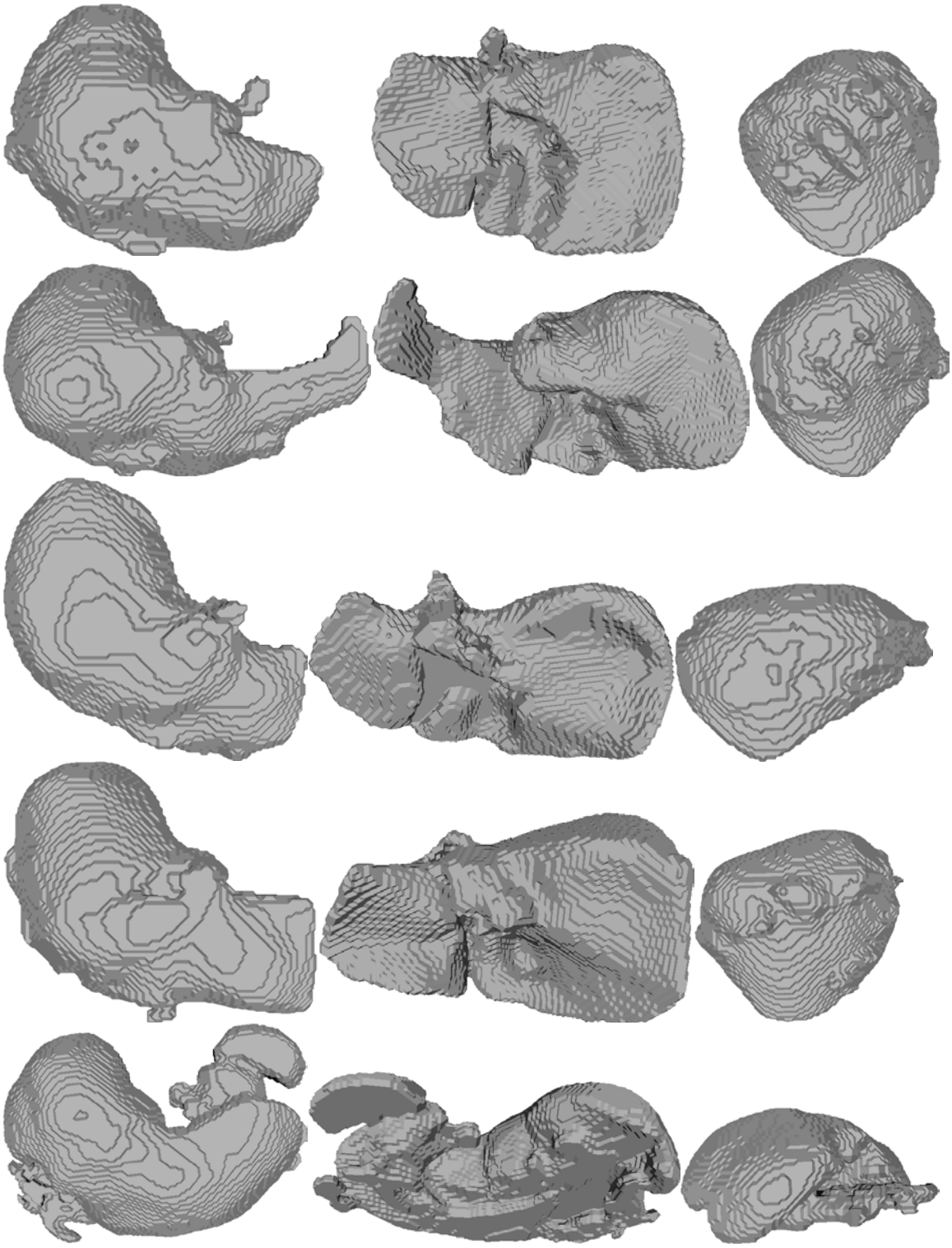

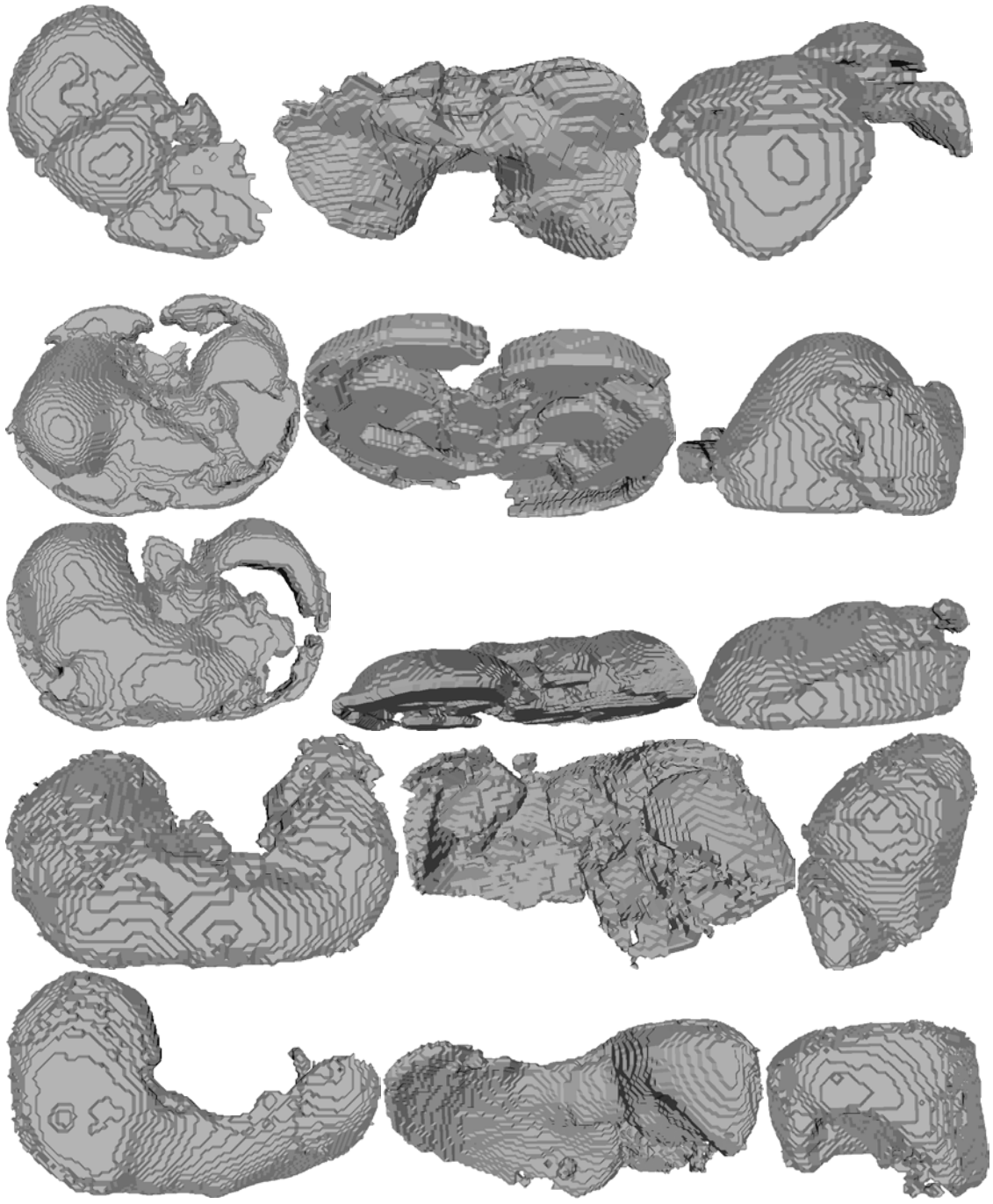

1. Segmentation results of cardiac regions (5 cases).